

Tecnologica  
2020

LAPO MICCINESI

# Advanced Ground- Based Real and Synthetic Aperture Radar

PREMIO TESI DOTTORATO  
FIRENZE UNIVERSITY PRESS — UNIVERSITÀ DEGLI STUDI DI FIRENZE



Tecnologica  
2020

LAPO MICCINESI

# Advanced Ground- Based Real and Synthetic Aperture Radar

PREMIO TESI DOTTORATO  
FIRENZE UNIVERSITY PRESS — UNIVERSITÀ DEGLI STUDI DI FIRENZE



PREMIO TESI DI DOTTORATO

ISSN 2612-8039 (PRINT) | ISSN 2612-8020 (ONLINE)

PREMIO TESI DI DOTTORATO  
Commissione giudicatrice, anno 2020

Vincenzo Varano, *Presidente della commissione*

Aldo Bompani, *Area Scienze Sociali*

Mario Caciagli, *Area Scienze Sociali*

Franco Cambi, *Area Umanistica*

Giancarlo Garfagnini, *Area Umanistica*

Roberto Genesio, *Area Tecnologica*

Flavio Moroni, *Area Biomedica*

Adolfo Pazzagli, *Area Biomedica*

Giuliano Pinto, *Area Umanistica*

Vincenzo Schettino, *Area Scientifica*

Maria Chiara Torricelli, *Area Tecnologica*

Luca Uzielli, *Area Tecnologica*

Graziella Vescovini, *Area Umanistica*



Lapo Miccinesi

# Advanced Ground-Based Real and Synthetic Aperture Radar

FIRENZE UNIVERSITY PRESS

2021

Advanced Ground-Based Real and Synthetic Aperture Radar / Lapo Miccinesi. – Firenze : Firenze University Press, 2021.

(Premio Tesi di Dottorato; 93)

<https://www.fupress.com/isbn/9788855183772>

ISSN 2612-8039 (print)

ISSN 2612-8020 (online)

ISBN 978-88-5518-376-5 (Print)

ISBN 978-88-5518-377-2 (PDF)

ISBN 978-88-5518-378-9 (XML)

DOI 10.36253/978-88-5518-377-2


Front cover: imagine radar di ambiente urbano, ESECH Lab, 2021.

*FUP Best Practice in Scholarly Publishing* (DOI [https://doi.org/10.36253/fup\\_best\\_practice](https://doi.org/10.36253/fup_best_practice))

All publications are submitted to an external refereeing process under the responsibility of the FUP Editorial Board and the Scientific Boards of the series. The works published are evaluated and approved by the Editorial Board of the publishing house, and must be compliant with the Peer review policy, the Open Access, Copyright and Licensing policy and the Publication Ethics and Complaint policy.

*Firenze University Press Editorial Board*

M. Garzaniti (Editor-in-Chief), M.E. Alberti, F. Vittorio Arrigoni, E. Castellani, F. Ciampi, D. D'Andrea, A. Dolfi, R. Ferrise, A. Lambertini, R. Lanfredini, D. Lippi, G. Mari, A. Mariani, P.M. Mariano, S. Marinai, R. Minuti, P. Nanni, A. Orlandi, I. Palchetti, A. Perulli, G. Pratesi, S. Scaramuzzi, I. Stolzi.

 The online digital edition is published in Open Access on [www.fupress.com](http://www.fupress.com).

Content license: except where otherwise noted, the present work is released under Creative Commons Attribution 4.0 International license (CC BY 4.0: <http://creativecommons.org/licenses/by/4.0/legalcode>). This license allows you to share any part of the work by any means and format, modify it for any purpose, including commercial, as long as appropriate credit is given to the author, any changes made to the work are indicated and a URL link is provided to the license.

Metadata license: all the metadata are released under the Public Domain Dedication license (CC0 1.0 Universal: <https://creativecommons.org/publicdomain/zero/1.0/legalcode>).

© 2021 Author(s)

Published by Firenze University Press

Firenze University Press

Università degli Studi di Firenze

via Cittadella, 7, 50144 Firenze, Italy

[www.fupress.com](http://www.fupress.com)

*This book is printed on acid-free paper*

*Printed in Italy*

# Table of contents

Preface	7
State of the art of Ground-based radar interferometry	9
1.1 GBRI in the Scientific Literature	10
1.2 Multiple Input Multiple Output (MIMO)	18
1.3 Detection of the Displacement Vector	19
1.4 Three-dimensional Imaging	20
1.5 Objective	20
Basic principles of Ground-Based Radar Interferometer	23
2.1 Target detection	23
2.2 Focusing algorithm	29
2.3 Interferometry	31
Radar systems for retrieving the displacement vector	35
3.1 Working principle of bistatic	36
3.2 Range and angular resolution of bistatic GB-SAR	39
3.3 Proof of principle	41
3.4 The transponder	50
3.5 Other applications	66
3.6 Conclusions	74

Compressive Sensing MIMO Radar	75
4.1 Compressive sensing	76
4.2 Compressive sensing for GBSAR	78
4.3 Compressive Sensing MIMO Interferometric Radar	93
4.4 Conclusions	104
Advanced in 3 dimensional GBSAR	107
5.1 GBSAR with 3D bistatic imaging capability	108
5.2 GBSAR with 3D imaging capability using compressive sensing MIMO in elevation	116
5.3 Conclusions	120
Conclusions	123
References	127

# Preface

Ground-based/terrestrial radar interferometry (GBRI) is a scientific topic of increasing interest in recent years. The GBRI is used in several fields as a remote sensing technique for monitoring natural environment (landslides, glaciers and mines) or infrastructures (bridges, towers).

These sensors provide the displacement of targets by measuring the phase difference between sending and receiving radar signal. If the acquisition rate is enough the GBRI can provide the natural frequency, e.g. by calculating the Fourier transform of displacement.

The research activity, presented in this work, concerns design and development of some advanced GBRI systems. These systems are related to the following issues: detection of displacement vector, Multiple Input Multiple Output (MIMO) and radars with 3D capability.

The conventional GBRI measures only the component of displacement along range direction. A GBRI operating in monostatic and bistatic modality is presented in this work. The sensor detects the first component of displacement as the conventional GBRI (monostatic) and an additional component through a transponder (bistatic).

The radar has been successfully tested in controlled environment using a basic transponder (two antennas and an amplifier). The transponder has



been improved in order to increase the gain of the amplifier and to solve some issues of the basic version. Finally, the system is used in real application for measuring the natural axis of a telecommunication tower.

The most advanced GRBI system can measure the direction of arrival of scattered signal by exploiting the movement of the antenna on an axis (Ground Based Synthetic Aperture Radar - GBSAR). The step between two position on the axis has to be smaller than a quarter of wavelength.

The emerging Multiple Input Multiple Output (MIMO) technique can be used to reduce the mechanical movement parts and the problems related to these. Also for MIMO radar the spacing between two closer phase center has to be smaller than a quarter of wavelength for the Shannon theorem.

In this work a Compressive Sensing (CS) MIMO radar is described. Indeed the CS is a technique able to reconstruct signal without the constrain of Shannon theorem. The signal has to be sparse and randomly sampled in order to use the CS.

The CS technique can be applied for increase the scan-length of a MIMO system of 40% ÷ 50%. Therefore, by using the same number of antennas, the CS allows to increase the angular resolution of a MIMO radar.

A prototype of interferometric CS MIMO radar has been developed and tested on some bridges. The results were compared with a conventional GBRI with a good agreement. The CS MIMO radar was able to discriminate the left-right movement of bridges. Unfortunately the repetition rate of this prototype was not enough to retrieve the spectra of natural frequency.

Since the movement is along a single axis the obtained radar image does not have angular resolution in the plane orthogonal to the scan axis. In other words, if the radar head scans along the x-axis the radar image cannot have resolution in elevation angle. This is not a serious problem when the scenario is a slope, where the elevation (z-axis) can be reasonably considered an unambiguous function of the (x,y) position. Unfortunately there are cases where the geometry of the structure under test is much more complex, i.e in urban environment.

In this thesis two radar systems with three dimensional resolution are reported. This two systems synthesize the two technique previously described. Indeed the first sensor uses the bistatic principle by exploiting the movement of an additional antenna in vertical axis for obtaining the resolution in elevation. The second system exploits the movement on an horizontal axis of the CS MIMO with phase center positioned on a vertical axis.

In order to test the capability, the two radars were located in a urban scenario in front of a 7-storey building. Both systems were able to provide a 3D image of the building.

# State of the art of Ground-based radar interferometry

Ground-based/terrestrial radar interferometry (GBRI) is a scientific topic of increasing interest in recent years. The GBRI is a popular remote sensing technique for monitoring landslides, mines, bridges, towers, dams, and other civil infrastructures.

The radar interferometry started as space technology. In the nineties, the satellites ERS-1, JERS-1, RADARSAT-1, and ERS-2 [1], [2], made use of the phase information of radar images for detecting ground changes. Spaceborne Synthetic Aperture Radar (SAR) systems, operating from an orbit at 800 km altitude, provide impressive interferograms due to the ground displacement after an earthquake [3], [4]. These extraordinary spaceborne developments had an early follow-up in analogue ground-based radar systems. Pioneering works anticipated some ideas. In 1997 [5], Tarchi et al. detected by radar the structural change of a beam in a large anechoic chamber. In 1999 [6], the same bulk laboratory equipment was used to detect the changes of a dam. In 2000, Pieraccini et al. [7] measured the deformations of a pedestrian bridge during its static test with a portable radar. In 2003 [8], a landslide was monitored by an interferometric Ground-based Synthetic Aperture Radar (GBSAR) for the first time.

In February 2000, a specifically modified radar system with one trans-

mitter and two receivers (the second at the end of a 60-meter mast that extended from the payload) flew on board the Space Shuttle Endeavour during the 11 day STS-99 mission [9]. This equipment was able to generate a high-resolution digital topographic database. Inspired by this idea, a GB-SAR has been modified for acquiring data with different baselines to obtain the Digital Elevation Model (DEM) of its field of view [10].

The strength of GBRI is its complementarity with spaceborne SAR [11], [12], [13], while the latter is a powerful and effective remote sensing technique for surveying large areas (many km<sup>2</sup>) at long term (return time in the order of several weeks or months), GBRI is suitable for monitoring small areas (from a single building to a slope) at short term (sampling time up to a few of minutes) as sketched in Figure 1.1.

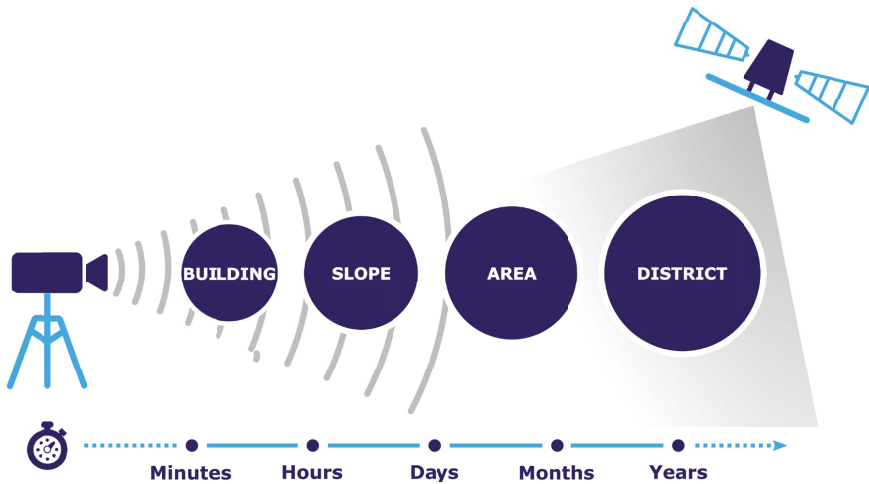


Figure 1.1: Complementarity of GBRI with spaceborne SAR.

## 1.1 GBRI in the Scientific Literature

Since the pioneering works in the nineties, the scientific literature of GBRI has greatly grown involving several academic groups, private companies, and government agencies. Figure 1.2 shows the number of publications from 1997 [5] to December 2018. The average bibliographic production of the last four year is 42 publications per year.

In the following section the publications are classified in terms of operative modality (design and operative bands) and in terms of its applications (landslide, bridge, building, mine,...). Finally some of the recent developments are briefly discussed: detection of displacement vector, Multiple Input Multiple Output and three-dimensional image.

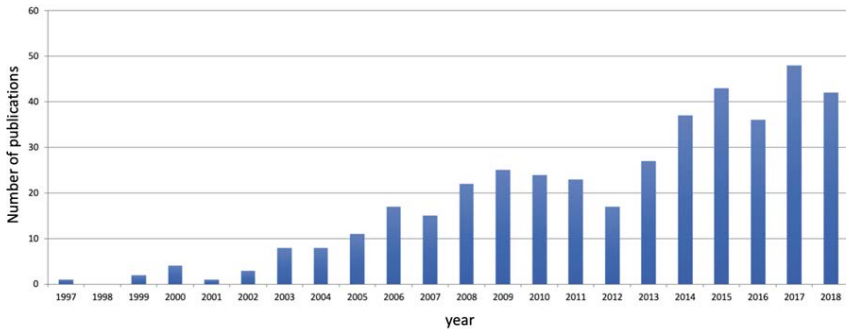


Figure 1.2: Papers published until December 2018 on GBRI [14].

Radars can detect a range by measuring the time-of-flight between the transmitted and received electromagnetic wave. The direction of arrival (DOA) cannot be detected (briefly “no-DOA”), [15], [16], [17], [18] or can be detected by the rotation of the radar head (“Rotary”) without any synthetic aperture [19], [20]. The most advanced radar systems are able to detect the direction of arrival through synthetic aperture (SAR: Synthetic Aperture Radar). The main advantage of SAR compared with equal aperture (physical or scanned) is that the angular resolution is twice good [21]. The simplest Ground-based Synthetic Aperture is based on the movement of a radar head along a linear mechanical guide (“linear SAR”) [7], [8]. Alternatively, it can be based on a circular movement (e.g., along an arc) [22], [23], [24]. This kind of radar is called “C-SAR”. Finally, the synthetic aperture can be made with multiple transmitting antennas and multiple receiving antennas (MIMO: Multiple Input Multiple Output) [25], [26]. A less common way to realize a synthetic aperture is to use the movement of a helicoidally slot [27]. Figure 1.3 shows pictures of some prototypes that exemplify these six operative modalities.

As shown in the histogram in Figure 1.4, the majority of the papers refer to linear SAR (58%) [7]. About 25% of the papers discuss developments or applications of radar interferometers without angular resolution (“real aperture”). About 8% of the publications refer to radar systems that achieve angular resolution just by rotating the antenna. These three operative modalities cover 91% of the publications.

The operative band is a key parameter of a radar. Generally speaking, by increasing the operative frequency, the angular resolution improves and the displacement resolution increases. At the same time, the temporal coherence of the targets decreases. Therefore, a balance is necessary. Figure 1.5 shows

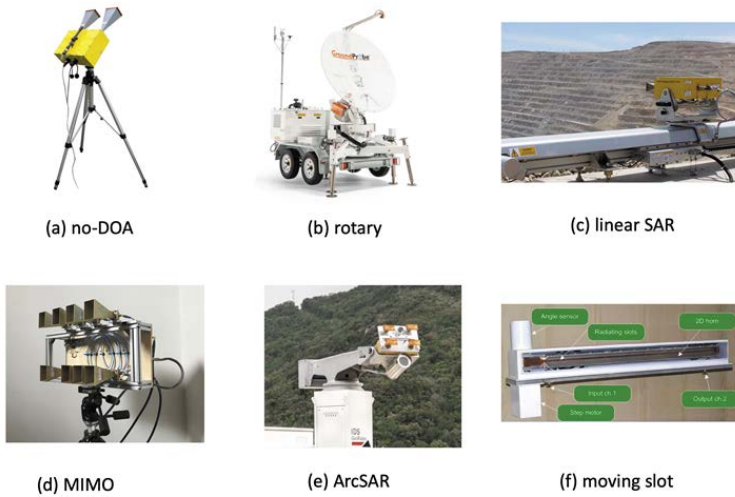


Figure 1.3: Examples of ground-based radar interferometers: (a) no-DOA (after [28]); (b) Rotary (after [29]); (c) linear SAR (after [28]); (d) MIMO (after [30]); (e) ArcSAR (after [48]); (f) moving slot (after [27]).

the histogram of the publications divided on the basis of the chosen operative frequency of the radar. About 58% of publications are relative to equipment in Ku-band (12 - 18 GHz). Some radar systems operate in C-band (4 - 8 GHz), and X-band (8 - 12 GHz). The Ku-band is a good trade-off between size of the equipment and temporal coherence of the targets, even if the C-band is probably preferable for monitoring snow covers [31], [32], [33]. The components cost can be another issue that can make the difference in the selection of the band. Until today, components in Ka and W were more expensive, but with the large diffusion of automotive radar in W-band, their cost is rapidly decreasing [34].

GBRI is an applicative topic. Figure 1.6 shows the whole the publications grouped based on the specific application. Obviously, a single publication can cover more than one application, and there are publications that do not refer to any specific application.

Landslide monitoring is doubtless the most popular application of GBRI (see Figure 1.7). Sinkhole monitoring [35] has been included in this category. Over 40% of the publications are developments or case-studies about monitoring systems of landslides. The first in-field test dates back to 2003 [8]. Landslide monitoring is an application of great social and scientific impact and currently many slopes are routinely monitored by radar interferome-



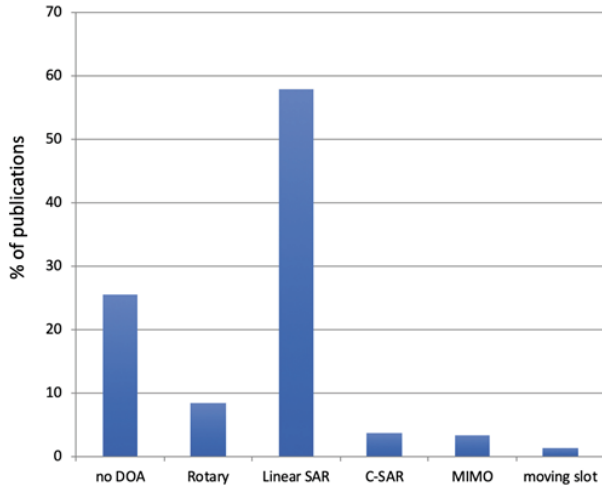


Figure 1.4: Papers published until December 2018 classified on the basis of the operative modality [14].

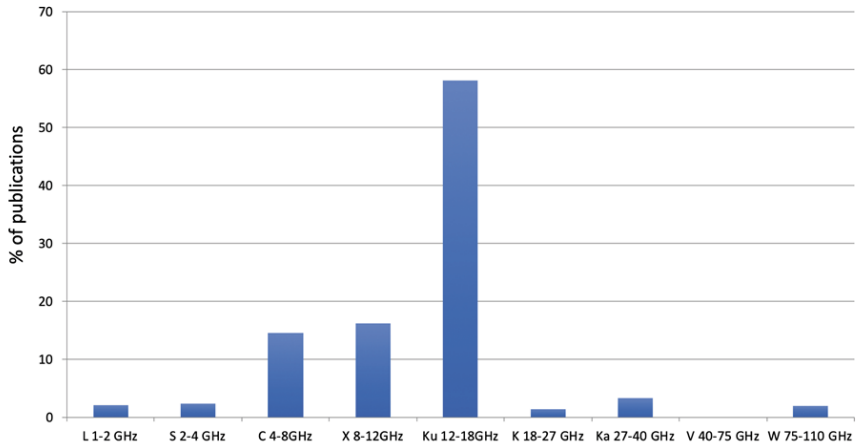


Figure 1.5: Papers published until December 2018 classified on the basis of the operative band [14].

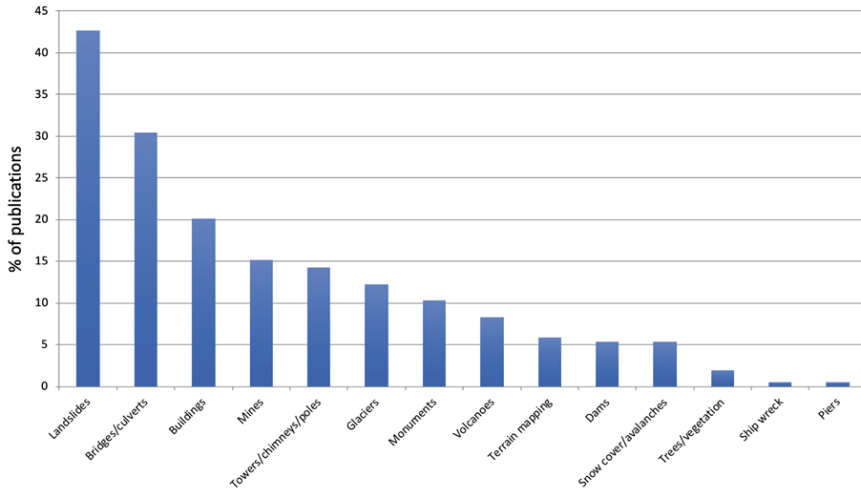


Figure 1.6: Papers published until December 2018 classified on the basis of their applications [14].

ters [36], [37].

Testing or monitoring of bridges is another key application (see Figure 1.7). The radar is a fast, reliable and accurate equipment for remotely sensing the static or dynamic behaviour of a bridge. Pieraccini et al. were the first (2000) that demonstrated [7] this possibility. Overall about 30% of publications refer to bridge monitoring.

Building is the third class of applications in order of popularity (see Figure 1.7). This class is less homogeneous if we considered radar systems that monitor construction works [41], villages built over landslide [42] or on terrain subject to subsidence [43]. Probably, this class of application is overestimated because many papers deal with the tests of equipment rather than their effective applications.

On the contrary, the class of the open pit mining is probably underestimated. Indeed, hundreds of radars are currently in operation as safety equipment in mining areas (see Figure 1.7), but the number of publications on monitoring activity for worker safety in mining areas is rather modest (about 15%). This is probably because mine safety is a rather confidential issue, and the owners hardly agree to publish their radar data. The first publication about it dates back to 2000 [19].

Monitoring of towers/chimneys/electric poles is another emerging application field of GBRI (see Figure 1.8). Generally speaking, all nearly one-dimensional structures, like bridges and towers, are particularly suitable for

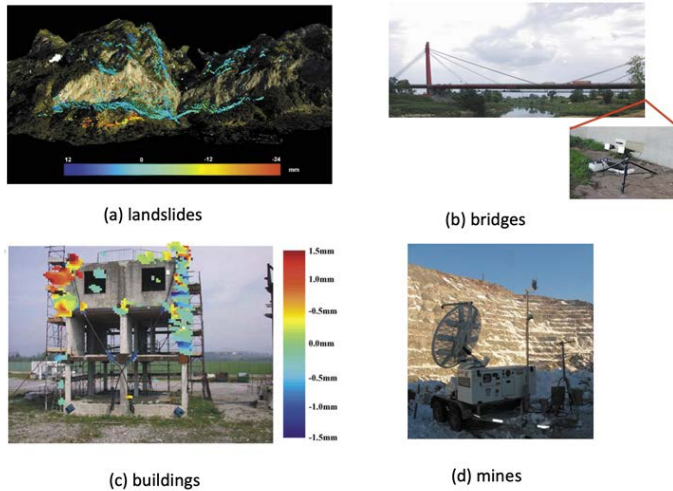


Figure 1.7: Examples of applications of GBRI: (a) landslide monitoring (after [38]), displacement map and picture projected on the digital elevation model of the slope; (b) monitoring of a viaduct in Florence, Italy; (c) displacement map projected on the picture of the monitored building (after [39]); (d) mines monitoring, radar deployed in Thompson Creek Mine, Idaho, USA (after [40]).

being monitored/tested by radar, as it does not require cross-range resolution. Therefore, if radar operates in no-DOA modality the structure can be sampled at over 50 - 100 Hz [15], [16], and its dynamic characteristics (natural frequencies, modal shape, transient response) can be detected.

Glaciers are fundamental “proxies” for standing the effects global warming on a local scale [48]. So, scientists have great interest in using GBRI for monitoring the change of glaciers (see Figure 1.8). The first case study dates back to 2007 [49], but aftermath many other studies on different glaciers have been performed (see for example [13], [50], [51]). In our bibliographic survey about 13% of the papers refer to glacier monitoring.

Another field of application of great scientific and social interest is the monitoring of cultural heritage (see Figure 1.8). Radar has been used for monitoring the leaning Tower of Pisa, Italy [16]; the towers of San Gimignano, Italy [52], the Bell-tower of Giotto in Florence [53], the Michelangelo’s David at Accademia Museum in Florence [46], the Baptistery of Florence, Italy [54], the ruins of Roman Forum of Rome, Italy [55], the retaining walls of the historical town of Volterra, Tuscany [56], and other sites [57], [58]. Overall the publications the refer to Cultural Heritage represent about 10% of the total.

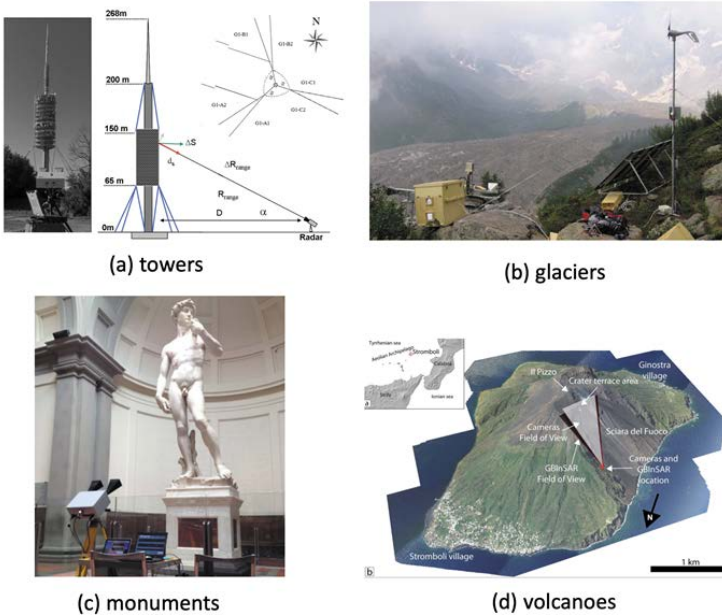


Figure 1.8: Examples of GBRI applications: (a) towers (after [44]); (b) glaciers (after [45]); (c) monuments (after [46]); (d) volcanoes, permanent installation at the Stromboli volcano, Italy (after [47]).

Volcanoes are both a fascinating phenomenon and an impending risk for people living around their flanks. Therefore, although the number of active volcanoes is rather limited, over 8% of the scientific papers refer to volcanoes. In particular, Stromboli volcano, Italy, (see Figure 1.8) is one of the most studied volcanoes in the world [59], [60], [61], [62], [63] and it has been continuously monitored by terrestrial radar since 2008 [64]. Also, Soufrière Hills in the Montserrat island [65] and Hakone volcano in Japan [66] have been monitored by terrestrial radar.

Digital Elevation Model (DEM) production is another interesting GBRI application (see Figure 1.9). Twelve papers (6% of total) have been published on this subject. The main finding is that this technique is effective even by a terrestrial radar, but its accuracy is sensibly worse than traditional equipment (photogrammetry or Terrestrial Laser Scanner) [10].

Dam-monitoring has been the first in-field application of GBRI: it dates back to 1999 [6] (see Figure 1.9). The concrete surface of a dam is almost an ideal target for radar interferometry; it is coherent, homogeneous enough but not specular. Nevertheless, the papers related to this application are

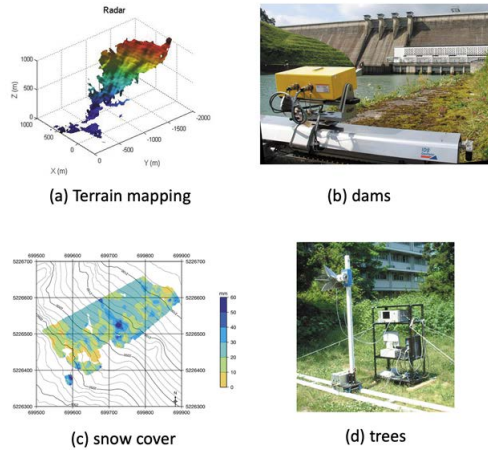


Figure 1.9: Examples of GBRI applications: (a) terrain mapping, digital elevation model of a slope obtained through GBSAR (after [67]) (b) dams monitoring (courtesy of IDS georadar [28]); (c) snow cover monitoring, map of snow water equivalent change obtained by GBSAR (after [68]); (d) trees monitoring by GBSAR (after [69]).

only 5% of total, but dams have already sophisticated monitoring systems with different sensors [70], so there is no demand for novel sensors; and dam safety, as well as mines, is a rather confidential issue, and the owners hardly agree to publish their radar data.

Martinez-Vazquez in 2005 [31] proposed the GBRI for assessing snow cover change (see Figure 1.9), as it has already been done by satellite [71]. The technique's results are effective with dry snow, while wet snow can be a problem [32]. Very interesting results have been obtained using the radar for mapping the avalanches on steep slopes [33].

Monitoring of vegetation or trees by GBSAR (see Figure 1.9) [69] is again a marginal application (2% of the total).

Finally, it is worth noting two very peculiar applications. On January 2012, the Italian cruise ship *Costa Concordia* ran aground and overturned after striking an underwater rock close to the *Isola del Giglio*, Tuscany. The wreck came to rest on a rock ledge several months before its translation and decommissioning. In this period, an interferometric radar was installed over a rock of the island for monitoring possible displacements of the wreck [72]. The radar detection of the displacement of a pier pulled by a tugboat is the second noteworthy application [73].

These are the applications that we can find in the scientific literature, but



they surely do not exhaust all the possibilities of GBRI. Just as an example of a possible interesting development, we can refer to some preliminary works on the use of radar for monitoring wind turbines [74], [75]. The rotation of the blades gives a peculiar doppler signature (named “sinogram”); Li et al. [76] had the idea to apply the ISAR (Inverse Synthetic Aperture Radar) techniques for focusing the sinograms. In this way they obtained high-resolution radar images of the blades. A further step could be processing interferograms between different rotations for detecting the deformation of the blades under stress. The same technique could be used for monitoring any other turbines like steam turbines and turbofans of airplanes.

## 1.2 Multiple Input Multiple Output (MIMO)

The linear GBSAR as well as any rotary radar and C-SAR need the physical movement of a radar head. The mechanical moving parts are the most prone to failures, especially in systems that operate outdoors for long periods. This is the case with the monitoring of mines and slopes. The phased array radar [77] is a possible solution. This technology is well-known and widely used in the military field. Its problem is the cost, which is too high for civil applications. An emerging paradigm in the radar field is the MIMO (Multiple Input Multiple Output). The idea is to use a set of  $N_{TX}$  transmitting antennas and a separate set of  $N_{RX}$  receiving antennas suitably positioned in space (see Figure 1.10).

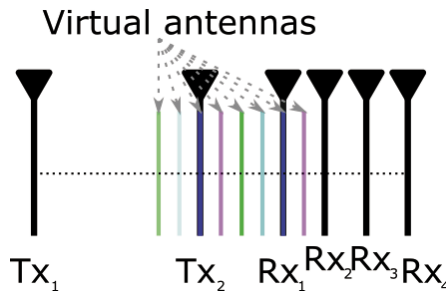


Figure 1.10: MIMO working principle,  $N_{TX}$  transmitting antennas with  $N_{RX}$  receiving antennas are equivalent to  $N_{TX} \times N_{RX}$  “virtual” antennas.

For each transmitting antenna, all the receiving antennas are working (simultaneously or sequentially), so the number of independent measurements is given by  $N = N_{TX} \times N_{RX}$ . The resulting system is a radar equivalent to a phased array that needs much less transmitting/receiving channels.

The first to propose this approach for a GBSAR was Hong in 2010 [78]. Tarchi et al. published in 2013 [25] a notable implementation of MIMO-

GBSAR named MELISSA; 16 transmitting antennas operating with 16 receiving antennas, an equivalent aperture of 2.56 m and an acquisition time of 3.6 ms. This very high speed of acquisition opens new interesting perspectives to this kind of radar, especially in the dynamic monitoring of buildings, towers and bridges. The MIMO approach, a radar like MELISSA, is again an equipment rather complex and expensive, that hardly can find an industrial justification in the market of monitoring equipment.

### 1.3 Detection of the Displacement Vector

The interferometric radar detects only the displacement component along the view direction. The real displacement (of slope, building, bridge, tower, ...) is retrieved with some hypothesis about the motion. For example, in a slope, the displacement can be supposed along the gradient, in the lower deck of a bridge along the vertical axis and in a tower along the horizontal. These suppositions can be reasonable in most cases, but there are important exceptions. As Dei et al. in 2013 [79] demonstrated for bridges, some targets, that are not at the center of the span, have a component of horizontal displacement during static monitoring of bridges. If this horizontal displacement is not considered, the results are absurd (a deck that rise when it is loaded). Figure 1.11 shows how this effect is in the relationship with the thickness of the deck and the position of its neutral axes.

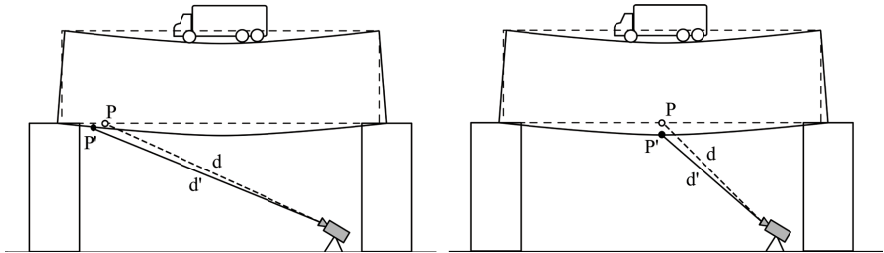


Figure 1.11: Effective displacement of a point  $P$  at an edge and close to the central span during the static test of a bridge.

The case of slope monitoring can be more complex. For example, for detecting the real displacement pattern of Lamosano village in Italian Alps, built on a landslide, it has been necessary to combine data from both interferometric radar and lidar [42]. Unfortunately, this complex behaviour of landslides is rather common.

In order to obtain more than one component of the displacement vector, in 2014, Severin et al. [80] used two GBSAR systems in different positions

that monitor the same slope. In 2015, Zeng et al. [81] proposed the same principle using two MIMO. Two radar systems operating independently can be a solution, but surely is expensive and not practical.

Other solutions are effective only in short range; Hu et al. [82] proposed to divide the scan in two sub-apertures for obtaining two points of view with the drawback to reduce the angular resolution; Pieraccini et al. [83] proposed to use the rotation of the antenna in a vertical plane for obtaining two or three components. They tested the technique during the static test of a bridge in Florence, Italy [84].

## 1.4 Three-dimensional Imaging

The idea of obtaining three-dimensional radar images using a GBSAR started with this radar itself. Already in 2000 Lopez-Sanchez [85] described a SAR migration algorithm for focusing three-dimensional images in an anechoic chamber. In the same year, Tarchi et al. [86] developed a GBSAR that obtains a 3D image of the reproduction (in scale 1:2) of an ancient façade.

Generally speaking, complex targets like buildings, tunnels, and construction works would require 3D imaging capability, but there are two practical problems. The first is the long acquisition time. With reference to Figure 1.12, in order to image in the three-dimensional space using a linear SAR, the radar head must scan step-by-step and line-by-line a planar surface. As an example, a fast GBSAR able to scan a line of 100 points in 5 minutes [87], will scan a plane of 100 lines in more than 8 hours. It means that the radar is able to detect only very slow movements. The second problem is the size and bulk of the mechanical system, which makes its deployment hard.

These are the main reasons why GBSARs with 3D imaging capability are not very popular.

The use of higher frequency (e.g., W-band) mitigates the problem of the bulky equipment, and partially even the problem of acquisition time, as the movements are smaller and, therefore, faster. The radar HYDRA [88] is a step in this direction.

A more radical solution is a two-dimensional MIMO [89]. These are exciting developments, but they are again prototypes in a laboratory and not suitable to be used in the field.

## 1.5 Objective

More than 415 scientific papers on GBRI have been published from 1997. The linear SAR is the most common system, followed by the no-DOA sys-

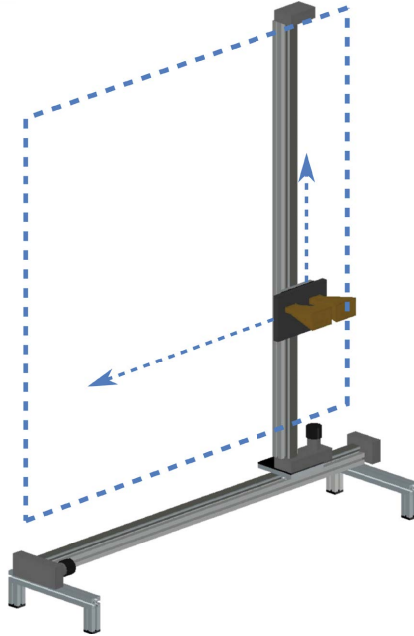


Figure 1.12: GBSAR with 3D imaging capability.

tems. The majority of radar systems work in Ku-band. More than 40% of case studies are relative to landslides followed by bridges (30%) and buildings (20%).

There are several open issue in the GBRI systems that can involve their application, e.g. wind turbines, or their technological improvement. The main technological development directions are forward faster radar (i.e. from SF modulation to FM modulation), radar with wider view angle (using ArcSAR configurations [22], [23], [24]), MIMO radar, radar with capability to detect the vector of displacement and not only a single component, and small size radars operating at higher band (in Ka or W band).

Currently, FM modulation and ArcSAR appear already mature for the market of monitoring equipment. Some manufacturers have products with these characteristics. MIMO GBSAR is at a good level of industrialization and probably, in a short time, we will see its diffusion. The detection of the displacement vector is again at the level of prototypes, but its usefulness is evident, and it will probably soon be established as a standard technique. Finally, interferometric radar in Ka or W band are again laboratory prototype, but probability they will have a role in the future, as well as radars with 3D imaging capability.

The aim of this work is to present some solutions founded during the doctoral course of the author. In the next chapters a bistatic system for retrieving the displacement vector, a Compressive Sensing MIMO system and some 3-D radar systems are presented.



# Basic principles of Ground-Based Radar Interferometer

In this chapter a theoretical background of GBSAR are introduced. The main definitions (i.e. range resolution, azimuth resolution) and concepts (i.e. focussing algorithm) of ground-based/terrestrial radar are summarize. In the next chapter, when it is needed, the concepts are extended or resumed.

## 2.1 Target detection

Radar is an electromagnetic devices able to locate reflective objects called targets. The basic principle of radar is illustrated in Figure 2.1. A transmitter generates a signal (e.g. a short pulse or a sine function) that is radiated by the TX antenna. A portion of the transmitted signal is backscattered by the target in many directions. The backscattered signal directed back towards the radar (named echo) is collected by the RX antenna which delivery it to a receiver. Therefore it is processed to detect the presence of the target and its location.

General speaking, the distance, or range, to a target can be calculated by measuring the time that signal takes to travel to target and return back to the radar, according to the follow equation:

$$R = \frac{c \cdot \Delta T}{2} \quad (2.1)$$

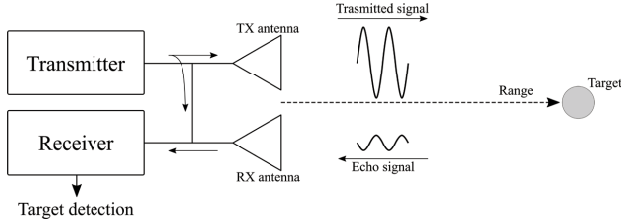


Figure 2.1: Basic principle of radar.

Where  $R$  is the range to the target,  $c$  is the speed of light and  $\Delta T$  is the travel time.

Radars can operate by using several kinds of signal: short pulse, Stepped-Frequency, frequency modulation. Usually, Stepped-Frequency (SF) waveform (see Fig. 2.2) is used in terrestrial interferometer. Indeed, the first terrestrial interferometric radar used a Vector Network Analyzer (VNA) as transceiver [5] that operated a Stepped-Frequency (SF) waveform.

Most of the commercial equipments use SF modulation, even if, recently the radar interferometers of IDS geo-radar [90] and meta-sensing [91] are both Frequency-Modulated (FM) systems.

In this thesis most of the radar systems operates a SF signal (after [24]).

Figure 2.2 shows an example of SF waveform. The SF radar sends a sweep of frequencies from the starting frequency  $f_1$  to the end frequency  $f_{N_f} = f_1 + B$ , where  $B$  is the bandwidth, with  $N_f$  steps.

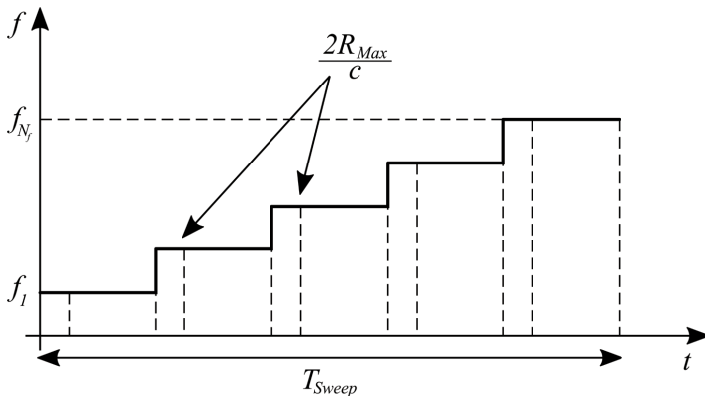


Figure 2.2: Step Frequency modulation.

The in-phase ( $I_j$ ) and quadrature ( $Q_j$ ) component of scattered signal is

detected for each  $j$ -frequency

$$E_j = I_j + iQ_j \quad (2.2)$$

where  $E_j$  is echo received by radar and  $i$  is the imaginary unit.

The radar image can be obtained by calculating the inverse Fourier transform (IFFT) of the echo [24]:

$$I = \text{IFFT}(E, N_f \cdot F) \quad (2.3)$$

where  $I$  is the obtained radar image and  $F$  is the padding factor.

In order to reduce the side lobes and improve the quality of the image a frequency windowing can be applied to the echo before calculating the IFFT

$$E_j^W = E_j \cdot W_j \quad (2.4)$$

where  $W$  is the windowing function and  $E_j^W$  is the  $j$ -component of echo after window.

There are several windowing functions, Figure 2.3 shows an example of some possible of them [92]. The windowing decrease both the side lobe level and resolution.

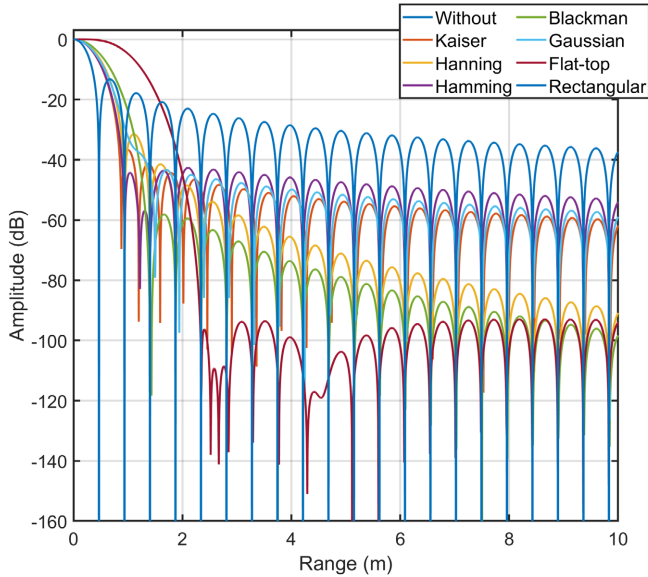


Figure 2.3: Example of windowing functions.

In this thesis a Kaiser window has been used:

$$w(n) = \frac{I_0\left(\beta\sqrt{1 - \left(\frac{2n}{N} - 1\right)^2}\right)}{I_0(\beta)} \quad (2.5)$$

where  $0 \leq n \leq N$ ,  $N$  is the number of samples of the window (equal to the number of frequencies),  $I_0$  is the zeroth-order modified Bessel function of the first kind and  $\beta$  is a non-negative real number that determines the shape of the window. The  $\beta$  used in this thesis is usually equal to 5.

### Range resolution and unambiguous range

The transmitted signal utilized a frequency bandwidth in order to separate and distinguish the targets. Indeed, single targets can be discriminated in range if their separation is bigger than [93]:

$$R_{res} = \frac{c}{2B} \quad (2.6)$$

This equation represents the range resolution ( $R_{res}$ ) of a radar.

The unambiguous range of a radar is the maximum range at which a target can be located so as to guarantee that the reflected signal/pulse from that target corresponds to the most recent transmitted pulse. In other word, if a target is farthest than the unambiguous range, it appear to be close to radar system as shown in Figure 2.4.

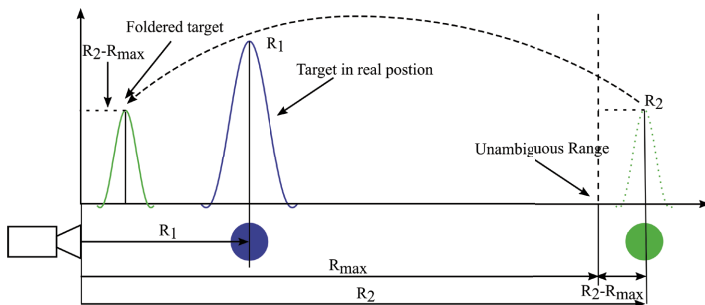


Figure 2.4: Unambiguous range.

In reference with Figure 2.4 the unambiguous range,  $R_{max}$ , can be found as follow:

$$R_{max} = \frac{c}{2B} N_f \quad (2.7)$$

### Azimuth resolution and angular ambiguity

While the range can be detected by using the bandwidth of the transmitted signal, the direction of arrival can be detected by exploiting the movement of the antennas.

The azimuth resolution is the minimum angle separation in order to resolve different target located at the same range (see Figure 2.5(a)). If the angular separation of two targets in the same range is smaller than the azimuth resolution (full width half maximum), their coherent summation results to be one single peak as shown in Figure 2.5(b).

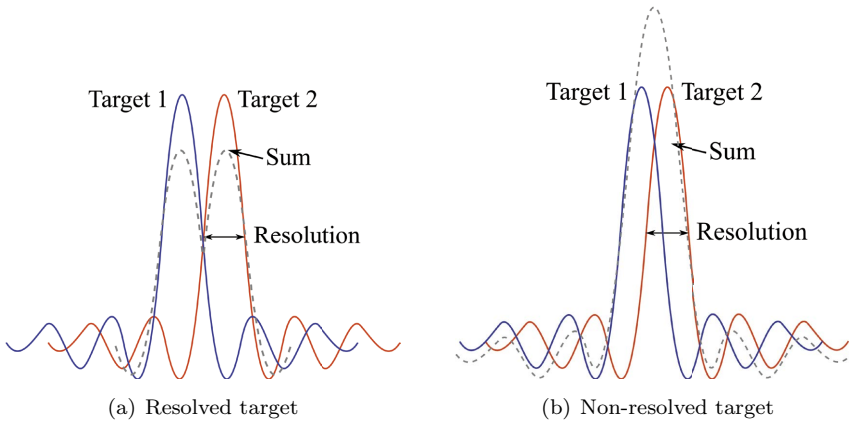


Figure 2.5: Azimuth resolution.

The most advanced radar systems are able to detect the direction of arrival through synthetic aperture (SAR: Synthetic Aperture Radar). In Figure 2.6 is shown the basic principle of a linear GBSAR, but all the followed conclusion can be generalized for any GBSAR system.

With reference to Figure 2.6(a), the signal received by the radar in position  $x=0$ , at central frequency  $f_0$ , from a target located in  $R_0$  is

$$E = e^{-i\frac{4\pi}{c} f_0 R_0} \quad (2.8)$$

while, the signal received in a generic position  $x$  is

$$E(x) = e^{-i\frac{4\pi}{c} f_0 (R_0 - x \sin \theta_0)} \quad (2.9)$$

A rather easy method for obtaining a spatial image of a GBSAR is to

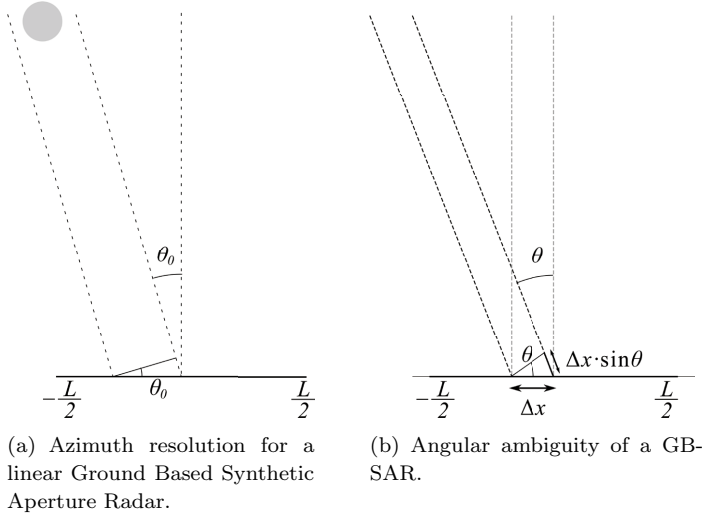


Figure 2.6: Basic principle of a linear GBSAR.

calculate the Fourier transform of the signal in spatial domain.

$$\begin{aligned}
 f(\theta) &= \frac{1}{L} \int_{-L/2}^{L/2} E(x) e^{j \frac{4\pi}{c} (-x \sin \theta)} dx = \\
 &= \frac{e^{-i \frac{4\pi}{c} f_0 R_0}}{L} \int_{-L/2}^{L/2} e^{i \frac{4\pi}{c} (f_0 x \sin \theta_0)} e^{j \frac{4\pi}{c} (-x \sin \theta)} dx
 \end{aligned} \tag{2.10}$$

where  $f(\theta)$  is the radar image.

By solving the integral in (2.10),  $f(\theta)$  is

$$f(\theta) = e^{-i \frac{4\pi}{c} f_0 R_0} \frac{\sin \left[ \frac{2\pi L f_0}{c} (\sin \theta - \sin \theta_0) \right]}{\frac{2\pi L f_0}{c} (\sin \theta - \sin \theta_0)} \tag{2.11}$$

The Equation (2.11) represents a sinc. Conventionally the full width half maximum (resolution) of a sinc is given

$$\frac{2\pi L f_0}{c} (\sin \theta - \sin \theta_0) = \pi \tag{2.12}$$

The angular resolution can be found by inserting the Taylor series expansion of  $\sin \theta|_{\theta=\theta_0}$  in (2.12)

$$\frac{4\pi L f_0}{c} \cos \theta_0 \Delta \theta \simeq 1 \tag{2.13}$$

where the second order of the series was used.

Therefore the angular resolution  $\Delta\theta$  is

$$\Delta\theta \cong \frac{\lambda}{2L\cos\theta_0} \quad (2.14)$$

with  $\lambda$  wavelength. The definition in (2.14) can be generalized for any different Synthetic Aperture system.

### Angular ambiguity

With reference to the unambiguous range, it is possible to define an angular ambiguity for the azimuth direction.

Generally speaking, to avoid the angular ambiguity, the step between two position in the GBSAR systems has to be smaller than a quarter of wavelength.

As shown in Figure 2.6(b) the phase difference between two radar positions, with step  $\Delta x$ , of a target in a generic angular position  $\theta$  can be write as  $\Delta x \sin(\theta)$ .

The phase difference between to position has to be

$$2 \times \Delta x \sin(\theta) = \frac{\lambda}{2} \quad (2.15)$$

in order to focus the target in the same position as shown in (2.9).

If  $\Delta x = \lambda/2$  the ambiguity,  $\theta_u$ , is in  $\pm\pi/2$  (Figure 2.7(b)). Instead, if  $\Delta x < \lambda/4$  all possible angular ambiguity is avoided. Figure 2.7 shows an example of angular ambiguity.

In real application the constrain given by (2.15) can be relaxed. Indeed, in real application the antennas are usually directional and it is enough that  $\theta_u$  is considerably larger than the angular aperture of the antenna.

## 2.2 Focusing algorithm

The measured echo signal in (2.9) can be write as follow:

$$E_{j,k} = I_{j,k} + iQ_{j,k} \quad (2.16)$$

where  $E_{j,k}$  is the echo of j-frequency taken from k-position of the radar.

With reference to Figure 2.8, the basic formula for focusing on a generic n-point (x, y, z) of the space surrounding the radar is [24]:

$$I_n = \sum_{j,k} E_{j,k} e^{i\frac{4\pi}{c} f_j R_{k,n}} \quad (2.17)$$

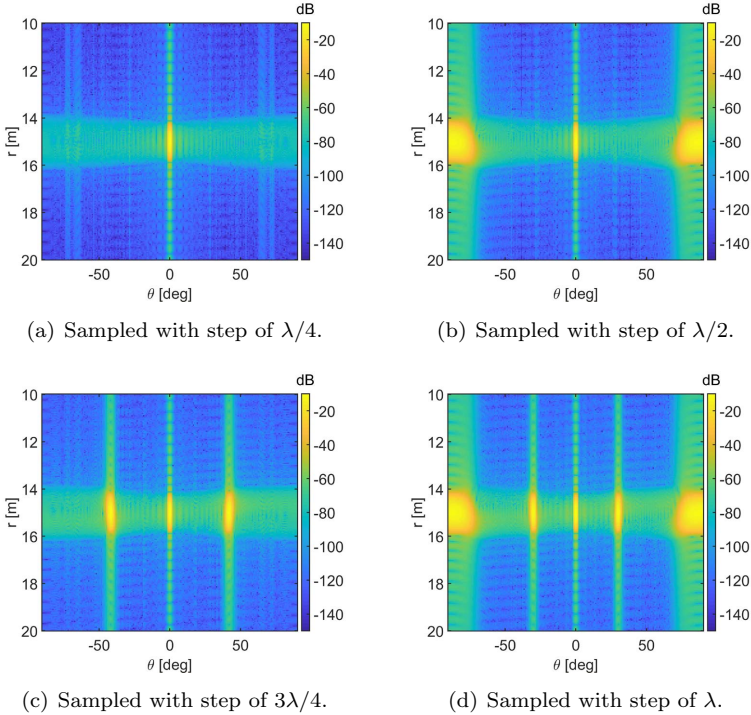


Figure 2.7: Example of angular ambiguity.

Equation (2.17) is rather computational heavy, so the key point of any focusing algorithm is to reduce its computational cost without a significant loss of generality and accuracy. A simple focusing algorithm has been proposed by Pieraccini et al in 2017 [24]

$$I(x, y, z) = \sum_k e^{j \frac{4\pi}{c} f_1 (p-1) \Delta R} \text{IFFT}_j(E_{j,k}, N_f \cdot F) e^{j \frac{4\pi}{c} \frac{B}{2} (R - (p-1) \Delta R)} \quad (2.18)$$

where  $I(x, y, z)$  is the radar image in point  $(x, y, z)$ ,  $c$  is the speed of light,  $f_1$  is the first frequency used in SF signal,  $B$  is the bandwidth,  $N_f$  is the number of frequency,  $F$  is the padding factor,  $\Delta R$  is define as

$$\Delta R = \frac{N_f - 1}{N_f F} \frac{c}{2B} \quad (2.19)$$

and  $p$  is an index defined by the  $k$ -position of antenna  $n$ -position on the grid:

$$p = \text{integer} \left( \frac{R_{k,n}}{\Delta R} \right) \quad (2.20)$$



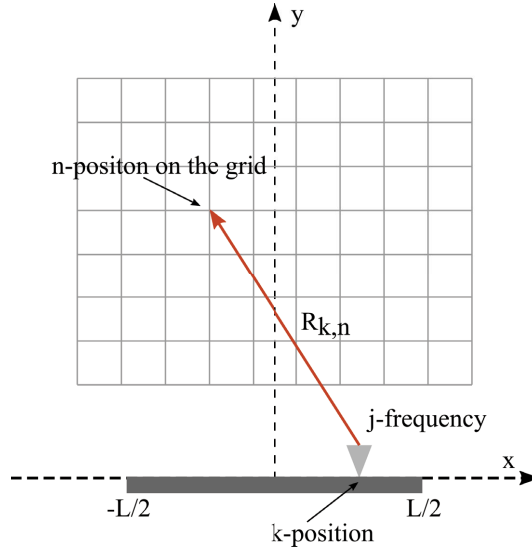


Figure 2.8: Focusing grid.

This focusing algorithm can be generalized for any kinds of synthetic aperture and signal used.

To improve the image quality a window can be applied also in cross-range direction.

### 2.3 Interferometry

The interferometric radar uses the phase information of the received signal to measure small displacement of the targets. Figure 2.9 shows the working principle of this technique, detailed description can be founded in the [8], [94], [95].

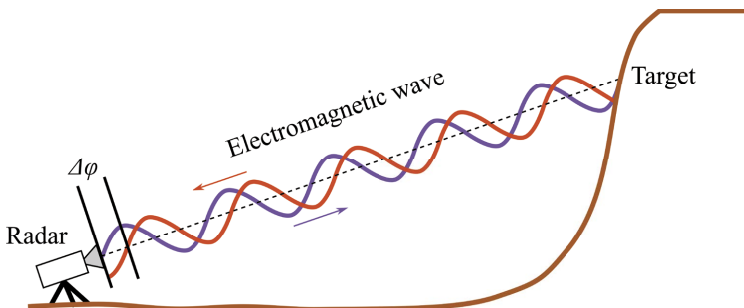


Figure 2.9: Working principle of ground based radar interferometry.

With reference to Figure 2.9 the phase difference between two acquisitions is given by:

$$\Delta\varphi = \Delta\varphi_{disp} + \Delta\varphi_{atm} + \Delta\varphi_{noise} \quad (2.21)$$

where  $\Delta\varphi_{disp}$  is related to a possible displacement of the target,  $\Delta\varphi_{atm}$  is related to the atmospheric conditions (humidity, temperature, pressure), and  $\Delta\varphi_{noise}$  is a phase noise contribution that can never be completely eliminated in experimental measurements.

The atmospheric phase contribution (usually named “atmospheric phase-screen” [96]) can be neglected for short-range short-term applications (indicatively when the distance radar-target is less than 100 - 200 m and the time between the acquisitions is shorter than 1 - 2 hours). In all other cases, the atmospheric phase-screen has to be removed with suitable processing techniques. The proposed algorithms for atmospheric correction are many [97], [98], [99]. Their working principle is always based on the identification of stable targets in the radar image. Using these stable targets the phase is compensated using a suitable (always approximated) atmospheric model. This phase-screen removal is a very critical point and limits the final accuracy in long term monitoring.

When the phase noise contribution is negligible and the atmospheric phase-screen is removed (or negligible), the possible displacement ( $\Delta R$ ) of the target between two acquisitions is detected as phase difference ( $\Delta\varphi$ ) through the following basic relationship [100]:

$$\Delta R = \frac{\Delta\varphi}{4\pi} \lambda \quad (2.22)$$

It is important to note that an interferometric radar is able to detect only the component of displacement in range direction.

Generally speaking an interferometric radar can be used both for dynamic and static test.

**Dynamic Monitoring:** in this case the main interest is to be able to retrieve the frequency spectrum of displacement. Nowadays, the dynamic monitoring is suitable for slender structure because of the high sample frequency (more than 100 Hz) does not allow to move the radar head to achieve the azimuth resolution.

**Static Monitoring:** the movement in this case is very slow (quasi-static) and the main interest is to detect precisely the displacement. While the frequency spectrum measurement does not present critical issue, the measure of absolute displacement is affected by systematic and deterministic error (phase noise, phase-screen, movement of structures, ...) that can be kept small but cannot be entirely eliminated [101]. In this case the measurement time is long enough to allow the movement of the radar in order

to achieve azimuth resolution. The static monitoring can be used for infrastructure (bridge and building) or for natural environment such as landslides.

In the next Chapters some prototypes of advanced interferometric radar are presented. Unfortunately, most of the measurements presented are related to static monitoring. This is due to the transceiver used: an old model of VNA (HP8720A). This VNA had a time-constraint for the data transmission with computer. Indeed , some of the radars presented could be used also for dynamic monitoring by using a more recent equipment.



## Radar systems for retrieving the displacement vector

The GBRI systems are able to provide maps of displacement along the range direction. Nevertheless, Severin et al. [80] demonstrated the great advantage of the vector displacement in slope monitoring, and Dei et al. [79] experimentally showed how the detection of only one component can give paradoxical results in structural monitoring (a bridge deck that is apparently raised when loaded).

In 2014, Crosetto et al. [102] proposed a non-interferometric procedure for detecting the transversal component of the displacement. In 2017, Hu et al. [82] proposed to process two half scans separately for obtaining two images with a baseline. Both methods are limited by the scan length: the larger is the scan the better is the accuracy of the traversal displacement.

In this chapter a GBSAR operating in monostatic and bistatic modality is presented [103], [104]. This system made use of a transponder as additional channel for performing the measurement. In this way, the same radar equipment is able to acquire two images taken from different points of view: so it is able to acquire two different components of the displacement of the targets. Contrary to the works [102], [82], the accuracy in the detection of the transversal displacement does not depend on the scan length (that in a GBSAR, installation can hardly overcome 2 - 3 m) but on the distance

between radar and transponder that can be tens or even hundreds meters.

In the last part of the chapter some other applications of this principle are presented [105], [106].

### 3.1 Working principle of bistatic

The working principle of the bistatic GBSAR is shown in Figure 3.1. A linear GBSAR acquires an image of its own field of view. Using a third antenna, it acquires a second image of the same scenario exploiting the bounce of the signal through a transponder. The transponder consists of a couple of antennas and an amplifier system.

The bistatic SAR image can be focused through the backprojection algorithm explained in Chapter 2. With reference to Figure 3.1, the back projection is implemented by compensating the phase history of any path radar-target-transponder-radar [104].

The monostatic and bistatic images are focused in the same grid, but generally this does not assure that they are coregistered [107], so they could need the application of a specific processing technique for associating the corresponding pixels in the two images. Nevertheless for targets that are smaller than resolution, and in an environment without heavy clutter, we can assume that the two images are coregistered. The experimental setup has been arranged according to this assumption.

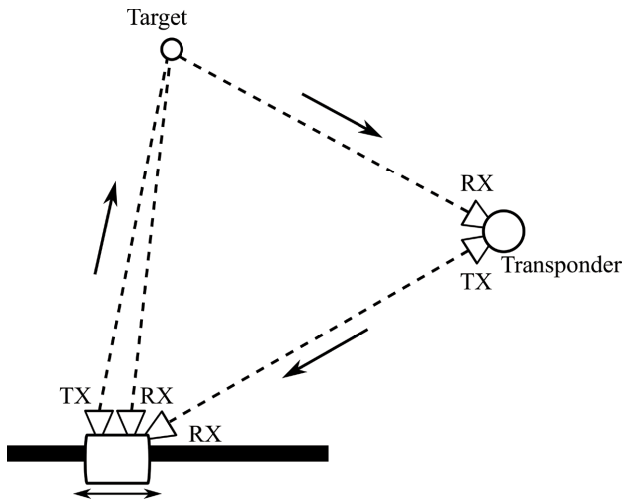


Figure 3.1: Working principle of bistatic GBSAR.

As known, in the monostatic configuration, when a target in the position

$(x_0, y_0)$  is displaced of a vector  $\vec{s}$ , the electromagnetic path is changed of

$$\Delta l_1 = 2(\vec{s} \cdot \vec{u}_1) \quad (3.1)$$

where  $\vec{u}_1$  is the unit vector from the radar to the target position (see Figure 3.2).

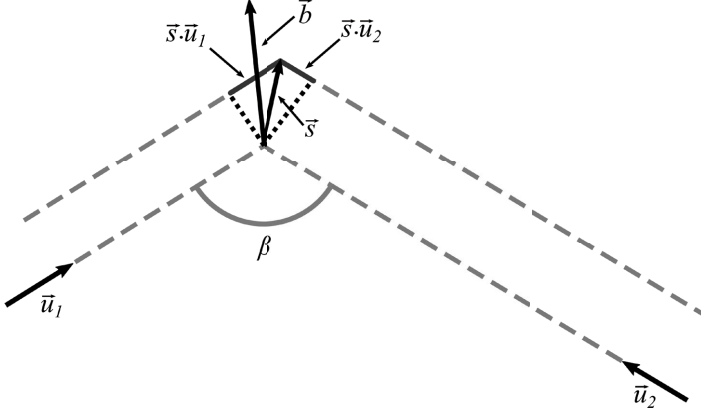


Figure 3.2: Detected displacements.

In accordance with (2.22) of the fundamental interferometric relation between phase ( $\Delta\varphi$ ) and displacement ( $\Delta l$ ) we can define:

$$\Delta s_1 \equiv \vec{s} \cdot \vec{u}_1 = \frac{\lambda}{4\pi} \Delta\varphi_1 \quad (3.2)$$

with  $\Delta\varphi_1$  differential phase measured by monostatic configuration.

In the bistatic configuration, when a target in the position  $(x_0, y_0)$  is displaced of a vector  $\vec{s}$ , the electromagnetic path is changed of

$$\Delta l_2 = \vec{s} \cdot \vec{u}_1 + \vec{s} \cdot \vec{u}_2 = \vec{s} \cdot \vec{b} |\vec{u}_1 + \vec{u}_2| = 2\vec{s} \cdot \vec{b} \cos\left(\frac{\beta}{2}\right) \quad (3.3)$$

where  $\vec{u}_2$  is the unit vector shown in Figure 3.2,  $\vec{b}$  is the bisector unit vector, and  $\beta$  is the bistatic angle.

Therefore the displacement measured by the bistatic configuration

$$\Delta s_2 = \vec{s} \cdot \vec{b} = \frac{\lambda}{4\pi \cos(\beta/2)} \Delta\varphi_2 \quad (3.4)$$

with  $\Delta\varphi_2$  differential phase in bistatic configuration. The detected displacements  $\Delta s_1$  and  $\Delta s_2$  are in linear relationship with the two orthogonal components  $\Delta x$  and  $\Delta y$  of the effective displacement

$$\begin{pmatrix} \Delta s_1 \\ \Delta s_2 \end{pmatrix} = M \begin{pmatrix} \Delta x \\ \Delta y \end{pmatrix} \quad (3.5)$$

with

$$M = \begin{bmatrix} \cos \vartheta_x^{(1)} & \cos \vartheta_y^{(1)} \\ \cos \vartheta_x^{(2)} & \cos \vartheta_y^{(2)} \end{bmatrix} \quad (3.6)$$

and

$$\cos \vartheta_x^{(m)} = \frac{\vec{s}_m \cdot \vec{i}}{|\vec{s}_m|}, \quad m = 1, 2 \quad (3.7)$$

$$\cos \vartheta_y^{(m)} = \frac{\vec{s}_m \cdot \vec{j}}{|\vec{s}_m|}, \quad m = 1, 2 \quad (3.8)$$

where  $\vec{i}$  and  $\vec{j}$  are the orthogonal basis of the Cartesian plane. Therefore

$$\begin{pmatrix} \Delta x \\ \Delta y \end{pmatrix} = M^{-1} \begin{pmatrix} \Delta s_1 \\ \Delta s_2 \end{pmatrix} \quad (3.9)$$

Equation (3.9) allows to calculate  $\Delta x$  and  $\Delta y$  from the measured  $\Delta s_1$  and  $\Delta s_2$ .

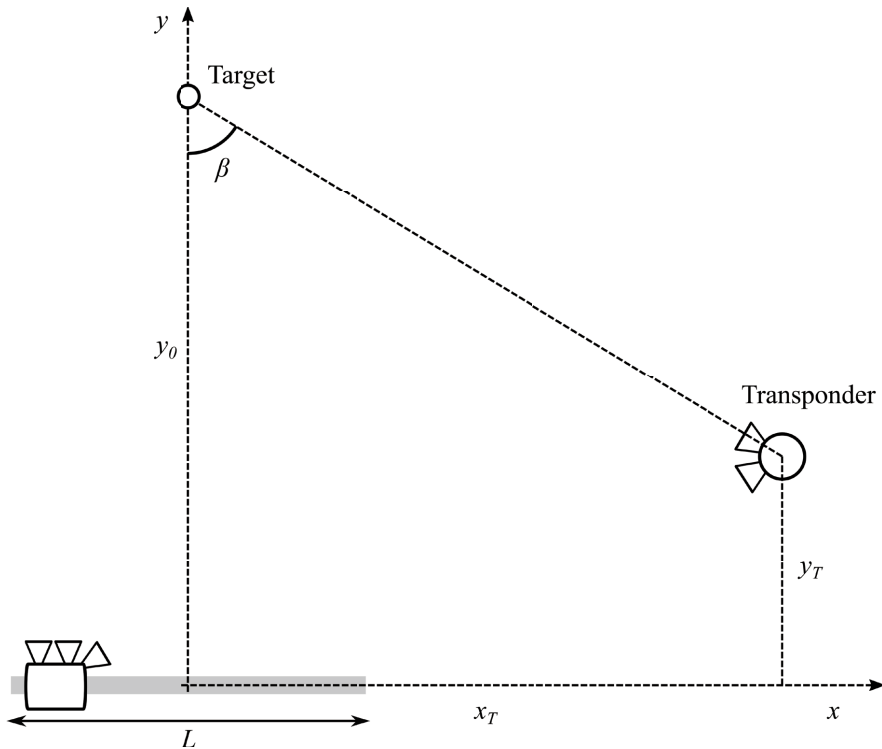


Figure 3.3: Measurement geometry.



In order to assess the measurement error, we can consider the case shown in Figure 3.3. The target is in front of the radar (along the  $y$ -direction) and the transponder is on a side. For this geometry, the matrix  $M$  results

$$M = \begin{bmatrix} 0 & 1 \\ \sin\left(\frac{\beta}{2}\right) & \cos\left(\frac{\beta}{2}\right) \end{bmatrix} \quad (3.10)$$

Let  $\delta\varphi_1$  be the phase uncertainty in monostatic configuration and  $\delta\varphi_2$  be the phase uncertainty in bistatic configuration, by inverting the matrix  $M$  and using (3.2) and (3.4), the displacement uncertainty along  $y$  ( $\delta y$ ) results

$$\delta y = \frac{\lambda}{4\pi} \delta\varphi_1 \quad (3.11)$$

while the displacement uncertainty along  $x$  ( $\delta x$ ) results

$$\delta x = \left| \cos\left(\frac{\beta}{2}\right) \right| \frac{\lambda}{4\pi} \delta\varphi_1 + \left| \frac{2}{\sin\beta} \right| \frac{\lambda}{4\pi} \delta\varphi_2 \quad (3.12)$$

This equation expresses how the uncertainty along  $x$ -axis depends on bistatic angle  $\beta$ . It is worth to note that  $\delta\varphi_1$  and  $\delta\varphi_2$  can be different. Indeed,  $\delta\varphi_2$  depends on bistatic radar cross section of the target (that is different from monostatic radar cross section) and even on the gain, noise figure, and phase stability of the transponder.

### 3.2 Range and angular resolution of bistatic GB-SAR

For estimating the range resolution we can refer to Figure 3.4. Considering the path C-A-T and the path C-B-T, they are separated in time if their difference is larger than the time resolution  $c/B$ , with  $c$  speed of light and  $B$  bandwidth.

Therefore

$$\Delta R + \Delta R \cos\beta = \frac{c}{B} \quad (3.13)$$

that is

$$\Delta R = \frac{c/B}{2 \cdot \cos^2\left(\frac{\beta}{2}\right)} \quad (3.14)$$

where  $\beta$  is again the bistatic angle.

It is worth to note as it differs from the well-known range resolution for a monostatic radar only for its dependence on the angle  $\beta$  and it coincides with the later when  $\beta = 0$ .

For estimating the angular resolution we have to take into account that the locus of points at the same time-delay are the points of the ellipse that has the scan center  $(0,0)$  and the transponder  $(x_T, y_T)$  as foci (see Figure 3.5).

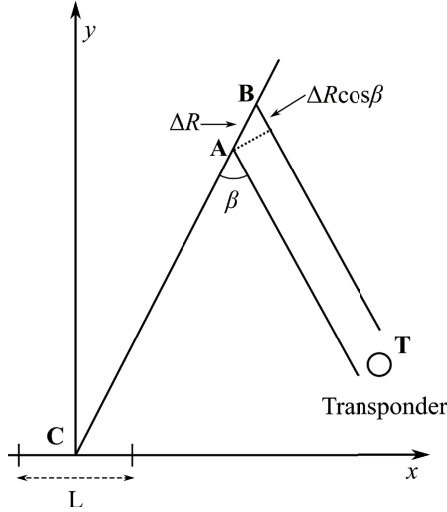


Figure 3.4: Estimation of range resolution.

Therefore it is convenient to define the angular resolution  $\Delta\phi_C$  with respect to the point  $(x_C, y_C)$  along the bisector of angle  $\beta$  crossing the straight line joining the scan center  $(0, 0)$  and the transponder  $(x_T, y_T)$ . If we shift the origin of axes in the point  $(x_C, y_C)$  the angular resolution will result well-defined.

By geometric consideration:

$$x_C = R_C \cos(\gamma) \quad y_C = R_C \sin(\gamma) \quad (3.15)$$

where  $R_C$  is the distance of  $(x_C, y_C)$  from the origin of axes. It can be obtained as

$$R_C = \left| \frac{\sin\left(\frac{\beta}{2}\right)}{\cos\left(\vartheta + \gamma - \frac{\beta}{2}\right)} \right| R_0 \quad (3.16)$$

with  $R_0$  in Figure 3.6.

Figure 3.6 sketches how to estimate the quantitative value of the angular resolution  $\Delta\phi_C$ .

It results with elementary geometrical considerations

$$\frac{\Delta\vartheta R_0}{\cos(\beta/2)} = \Delta\phi_C R_A \quad (3.17)$$

by using  $\Delta\vartheta$  from (2.14),  $\Delta\phi_C$  results

$$\Delta\phi_C = \frac{R_0}{R_A \cos(\beta/2)} \frac{\lambda}{2L \cos \vartheta} \quad (3.18)$$

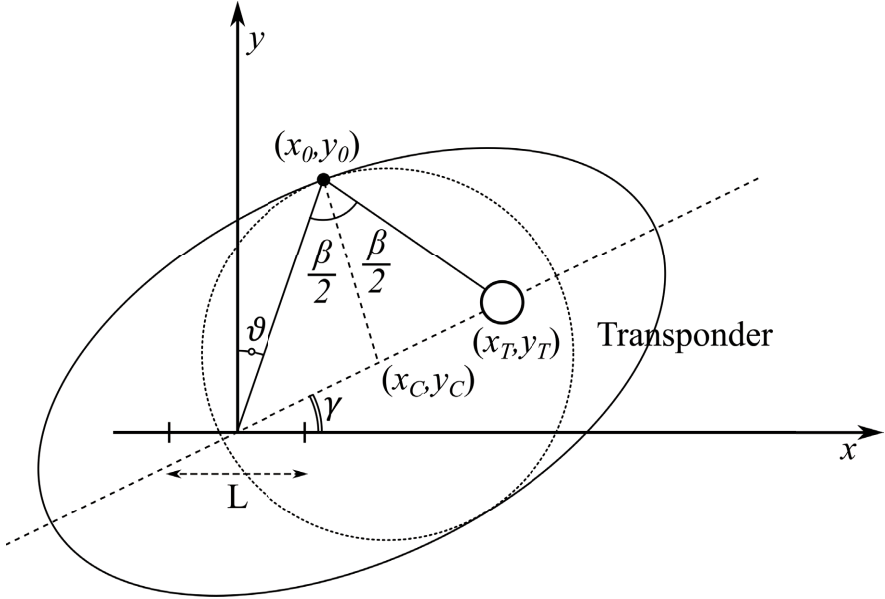


Figure 3.5: Constant time-delay ellipse.

### 3.3 Proof of principle

#### Equipment

Figure 3.7 shows a sketch of radar prototype that has been assembled for testing the working principle above described. The radar front end has been fixed on a mechanical axis controlled by a step motor. The maximum length of the axis was  $L = 1.80m$ .

A vector network analyzer (VNA) HP8720D operated as transceiver providing a continuous wave stepped frequency signal in the X-band with central frequency  $f_c = 10$  GHz, bandwidth  $B = 160$  MHz, and number of tones  $N_f = 401 \div 801$ . The radar operates step-by-step both in positions and frequencies.

A personal computer controlled the axis position and the data communications with VNA.

In reference to Figure 3.8, two RF cables linked the VNA to the front end. The VNA output power is 0 dBm, the one-way cable loss is -5 dB, and the TX amplifier gains 10 dB. Two single-pole double-throw (SPDT) switches provide a direct path (through a 40 dB attenuator) between the transmitter and the receiver in order to perform calibrated measurements. The aim of the calibration is to avoid the movements of the cables can affect

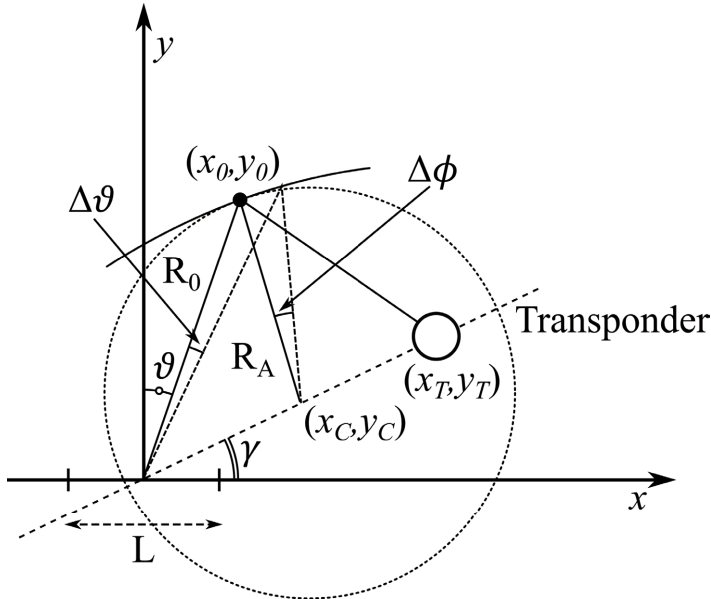


Figure 3.6: Geometry for the calculus of the angular resolution.

the phase measurement. An other SPDT switcher select the antenna that receive the echo from environment (monostatic channel) and the antenna for the signal trough the transponder (bistatic channel). The gain of the RX amplifier is 20 dB. The integration time of each tone was 1 ms.

The transponder consisted of two horns with 18 dB gain and a wideband amplifier (nominal gain: 50 dB, band: 6-18 GHz, and noise figure: 5 dB) on a tripod (see Figure 3.9).

The two antennas could be oriented and they were separated by a length of 1.44 m for minimizing the coupling and the possible oscillation of the transponder. Further details of transponder, i.e. its oscillation, will be given in the next section.

### Experimental test

For testing the capability to obtain bistatic radar images, the GBSAR and the transponder were installed in a garden of the University of Florence (Figure 3.10). At about 35 m in front of the radar there was a metallic fence, on the right a line of trees and a metallic signpost. The parameters used were:  $L = 1.80$  m,  $N_p = 240$ ,  $f_c = 10$  GHz,  $B = 160$  MHz,  $N_f = 801$ .

The transponder has been installed on the x-axis at 10 m on the left of the radar.

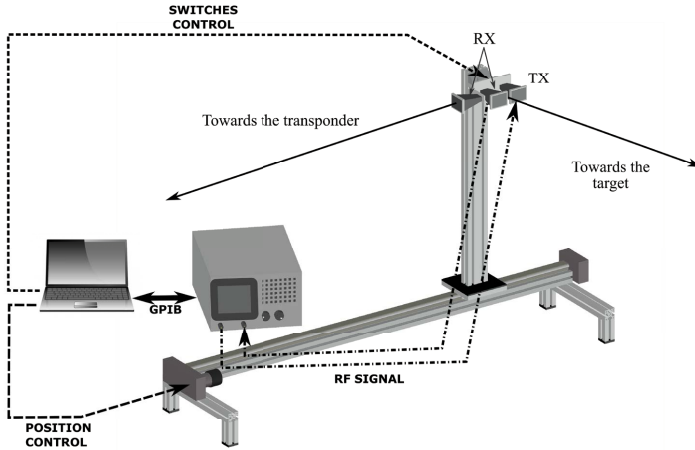


Figure 3.7: Radar prototype.

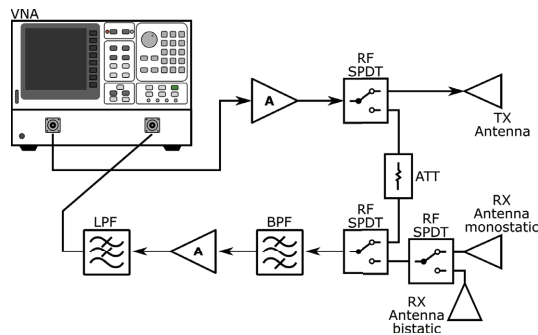


Figure 3.8: Block scheme of radar.

Figure 3.11 shows the focused bistatic image. The fence is well visible at about 35 m and on the right we can recognize the signal from the metallic signpost.

Figure 3.12 shows the plot of the amplitude in function of  $\phi_C$  (the angle with respect to  $(x_C, y_C)$ ) at the range of the metallic signpost that gives the maximum signal in the bistatic image. The plot relative to the target has been compared with the simulation of a point-target. The two plots were normalized at their maximum. The agreement between measurement and simulation is excellent and it confirms the bistatic radar imaging theory previously described.

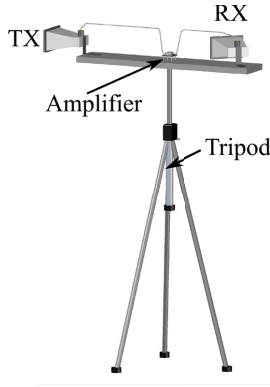


Figure 3.9: Transponder.

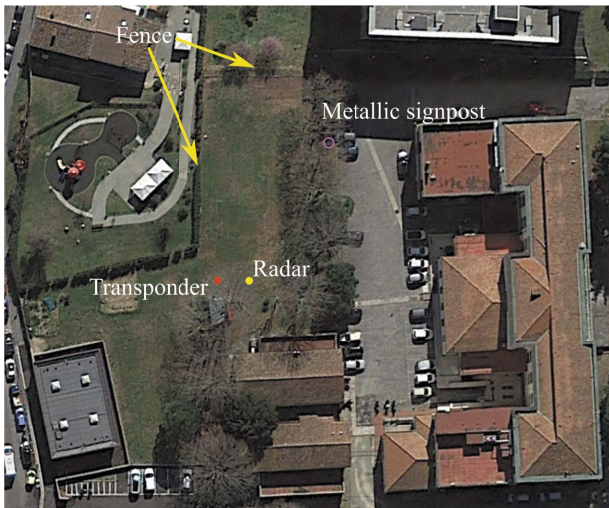


Figure 3.10: Aerial view of the University's garden.

### Measuring two components of displacement

The capability to measure two components of displacement has been tested in a controlled environment by making use of the same setup described before. The test site is an open field of University in Sesto Fiorentino, Florence, Italy.

A special target has been assembled aiming to test the capability of the radar to detect two components of the displacement. The target is a metallic pole provided with a small adjustable corner reflector  $10 \times 10 \text{ cm}^2$  and three grids disposed orthogonally, as shown in Figure 3.13. The aim of the grids

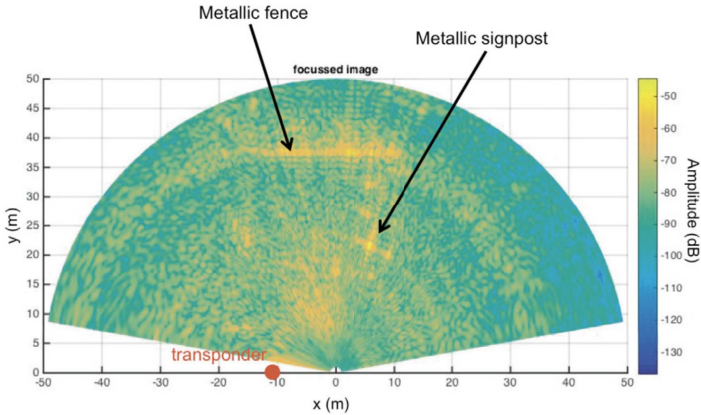


Figure 3.11: Bistatic radar image [104].

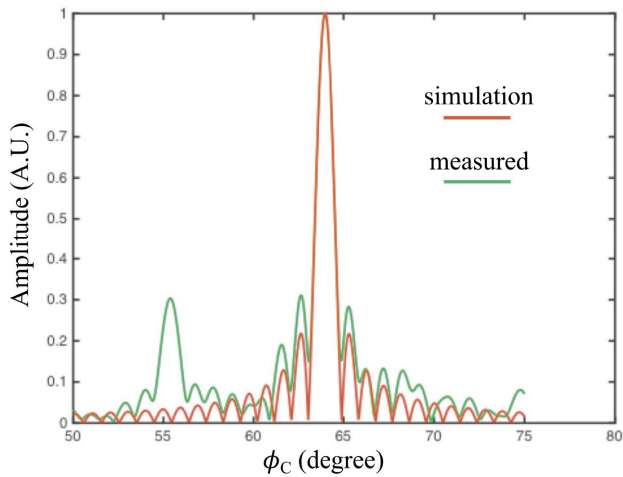


Figure 3.12: Measured angular plot of the metallic signpost compared with the simulation of a point-target [104].

is to provide a significant bistatic radar cross section.

The pole has been mounted on a linear micrometric stage platform with two orthogonal controlled movements on the  $xy$  plane with 0.1 mm nominal accuracy and 25 mm of maximum displacement. Some eccosorb has been used to cover the mechanical device. The micrometric stage was fastened to a wood table and a dead load kept the wood table fixed.

The target and the transponder were positioned, as shown in Figure 3.3.

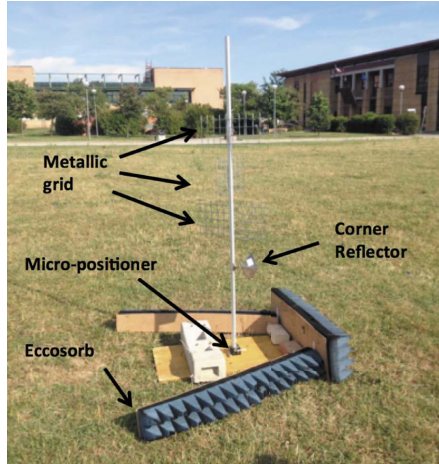


Figure 3.13: Picture of the target [103].

The distance target radar ( $y_0$ ) was 104.45 m, and the coordinates of the transponder were  $x_T = 39.53$  m and  $y_T = 45.80$  m.

Figure 3.14 shows the obtained monostatic image of the scenario where the radar has been installed, compared with an aerial picture. The more evident features are the large building at 300 m in front of the radar, the shack at about 200 m, and the corner of the building at about 130 m on the right. The target appears as a single point.

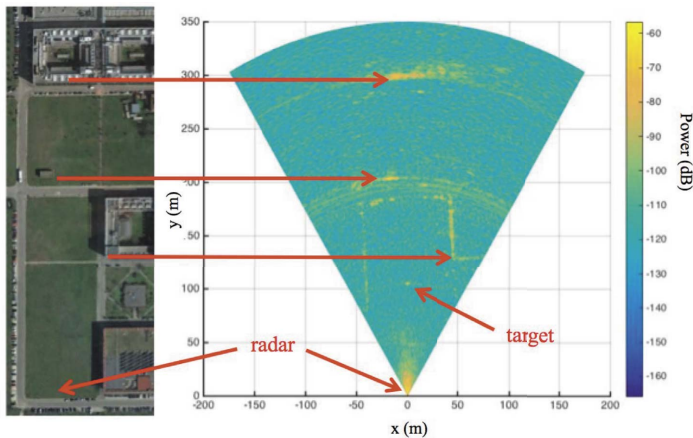


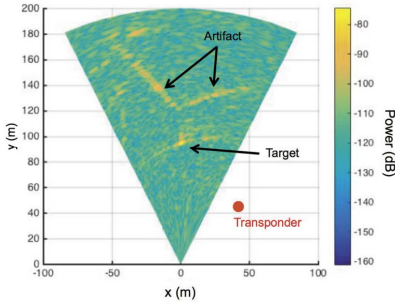
Figure 3.14: Monostatic radar image [103].

The obtained bistatic radar image of the same scenario is shown in Fig-

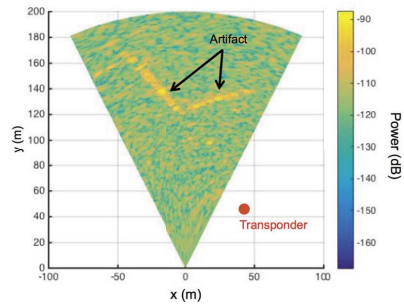


ure 3.15(a). The target is very recognizable as well as a feature (an artefact) that apparently does not correspond to any physical target.

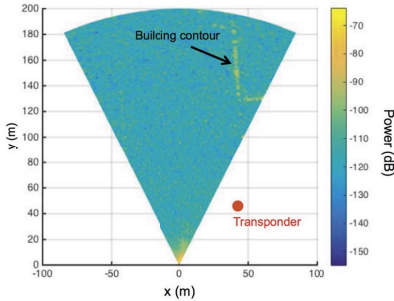
This artefact is due to the clutter behind the transponder that can give a monostatic signal even in bistatic configuration. This has been confirmed by focusing in bistatic modality an acquisition carried out when the transponder was switched OFF (Figure 3.15(b)).



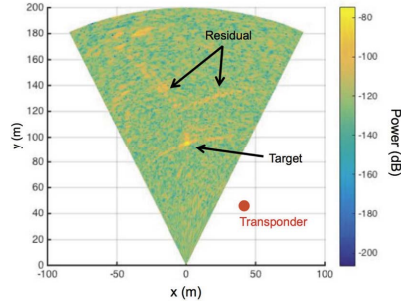
(a) Bistatic radar image [103].



(b) Bistatic radar image when the transponder was switched OFF [103].



(c) Radar image obtaining, focusing with the monostatic algorithm, the bistatic data acquired when the transponder was switched OFF [103].



(d) Bistatic radar image obtaining as subtraction of the images in Figure 3.15(a) and 3.15(b) [103].

Figure 3.15: Bistatic radar image and its artefacts [103].

By focusing the same acquisition in monostatic modality (performed when the transponder was switched OFF), it is evident that the artefact in bistatic image is due to the building behind the transponder on the right-hand side of the field of view (see Figure 3.15(c)).

This suggests a possible procedure for rejecting the artefact: to perform a bistatic acquisition when the transponder is switched ON and a second bistatic acquisition when the transponder is switched OFF. In the subtrac-

tion of the two images, the artefact results just a weak residual, as shown in Figure 3.15(d).

In order to evaluate the capability of the radar to detect two components of the displacement, the micrometric stage platform carried out displacements along x (toward the positive direction of the x-axis) at steps of 5 mm, from 0 to 25 mm. The  $\Delta x$  and  $\Delta y$  measured by the radar are shown in Figure 3.16.

The obtained mean absolute deviation of  $\Delta x$  around the nominal value was 1.74 mm, while the deviation of  $\Delta y$  was 0.60 mm. By considering each single step as an independent measurement, the mean value along x was 5.59 mm (to be compared to the nominal value 5 mm) with a standard deviation of 0.84 mm, while the mean value along y was -0.17 mm (to be compared to the nominal value 0 mm) with a standard deviation of 0.43 mm.

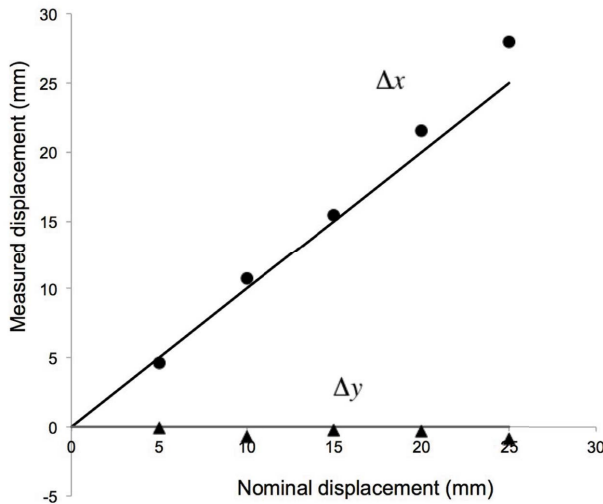


Figure 3.16: Displacements along x. Circles: measured displacements along x. Triangles: measured displacements along y. [103]

In a second measurement session, the same micrometric stage platform carried out displacements along y (toward the radar). In this case the distance target-radar ( $y_0$ ) was 75.39 m, and the coordinates of the transponder were  $x_T = 35.10$  m and  $y_T = 37.53$  m. The  $\Delta x$  and  $\Delta y$  measured by the radar are shown in Figure 3.17.

The obtained mean absolute deviation of  $\Delta x$  around the nominal value was 2.16 mm, while the deviation of  $\Delta y$  was 1.67 mm. By considering each single step as an independent measurement, the mean value along x was -0.41

mm (to be compared to the nominal value 0 mm) with a standard deviation of 3.02 mm, while the mean value along y was 5.33 mm (to be compared to the nominal value 5 mm) with a standard deviation of 0.64 mm.

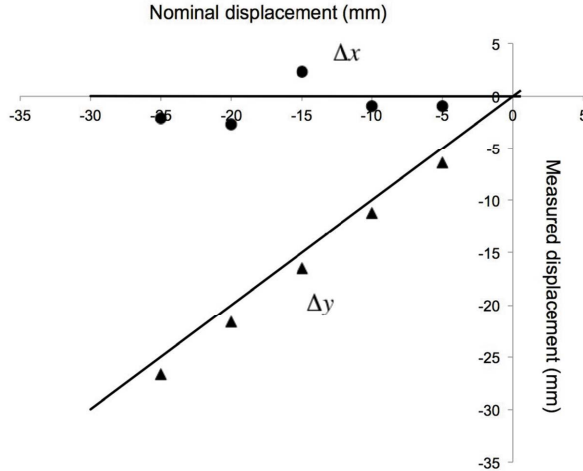


Figure 3.17: Displacements along y. Circles: measured displacements along x. Triangles: measured displacements along y. [103]

The capability of a monostatic/bistatic GBSAR to acquire the displacement vector was demonstrated with these two measurements section .

Some critical issues can be found in this basic approach: gain of transponder, “ghost targets”, long-term phase stability of transponder.

In the next Section possible solutions of these issues will be presented. Anyway, for some of them a simple solution can be found by using the before setup.

For avoiding the presence of “ghost targets” in the bistatic image, as a practical rule, the transponder should not be installed in a position, where there is heavy clutter in the background. Nevertheless, an effective countermeasure for rejecting/mitigating the “ghost targets” was to subtract the image acquired when the transponder was OFF from the image acquired when the transponder was ON. Anyway, the scenario can have small changes between the two acquisitions, so a weak residual could remain in the bistatic image.

A possible phase-changing of the transponder (phase of amplifier, small uncontrolled movement of the mechanical support of the transponder) can be treated as a change in the atmospheric phase screen and so can be compensated.

### 3.4 The transponder

As before mentioned a basic transponder consists in a couple of antennas and an amplifier. The gain of the amplifier has to be enough to compensate the path-loss and the noise.

In reference with Figure 3.18, by applying the radar equation [93] in monostatic and bistatic configurations, we obtain the following equations, respectively:

$$P_{rx}^{(mono)} = P_{tx} G_1 \frac{1}{4\pi R_{1,k}^2} \sigma^{(mono)} \frac{1}{4\pi R_{1,k}^2} G_2 \frac{\lambda^2}{4\pi} \quad (3.19)$$

$$P_{rx}^{(bist)} = P_{tx} G_1 \frac{1}{4\pi R_{1,k}^2} \sigma^{(bist)} \frac{1}{4\pi R_2^2} G_3 \frac{\lambda^2}{4\pi} A G_4 \frac{1}{4\pi R_{3,k}^2} G_5 \frac{\lambda^2}{4\pi} \quad (3.20)$$

where  $P_{tx}$  is the transmitted power;  $G_1$ ,  $G_2$ ,  $G_3$ ,  $G_4$ ,  $G_5$  are the gains of the five antennas;  $R_{1,k}$  is the distance between the radar head at the k-position along the mechanical guide and the target;  $R_1$  is the distance between the center of the mechanical guide and the target;  $R_2$  is the distance between the target and the transponder;  $A$  is the gain of the amplifier of the transponder;  $R_{3,k}$  is the distance between the radar head at the k-position along the mechanical guide and the transponder;  $R_3$  is the distance between the center of the mechanical guide and the transponder;  $\sigma^{(mono)}$  is the radar cross section in monostatic configuration;  $\sigma^{(bist)}$  is the radar cross section in bistatic configuration; and  $\lambda$  is the wavelength.

In practical deployments, the following assumptions are reasonable:

1. All the antennas have the same gain  $\Rightarrow G_1 = G_2 = G_3 = G_4 = G_5 = G$ .
2. The length ( $L_0$ ) of mechanical guide is much smaller than the radar-target and target-transponder paths  $\Rightarrow R_{1,k} = R_1$  and  $R_{3,k} = R_3$ .
3. Although  $R_1$  and  $R_3$  are not equal, they can be reasonably similar  $\Rightarrow R_1 \simeq R_3$ .
4.  $\sigma^{(mono)} \simeq \sigma^{(bist)}$ .

The last assumption is rather hard, but it can be done when the aim of the calculation is just a rough estimate of the received power. With these assumptions, the (3.19) and (3.20) become:

$$\frac{P_{rx}^{(bist)}}{P_{rx}^{(mono)}} = A \left( \frac{G\lambda}{4\pi R_3} \right)^2 \quad (3.21)$$

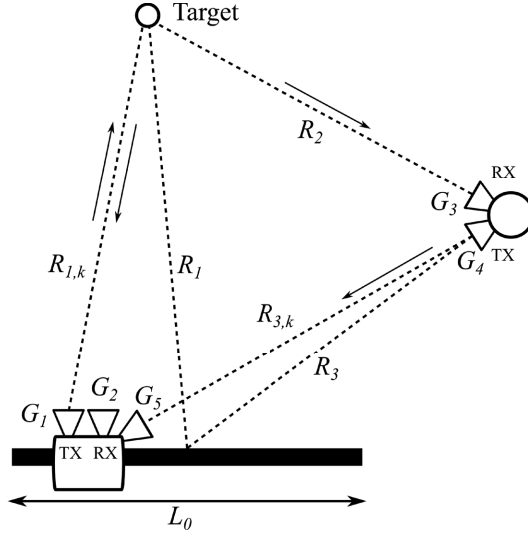


Figure 3.18: Monostatic/bistatic GBSAR with transponder.

Hence, in order to compensate the loss due to the path transponder-radar, the gain of the transponder should be as follows:

$$A = \left( \frac{4\pi R_3}{G\lambda} \right)^2 \quad (3.22)$$

This gain value compensates the loss; however, with this value of gain, the noise figure of the transponder is added to the noise figure of the first amplifier of the radar head. In order to improve the noise figure, the gain has to be increased. Indeed, as it is well known, the noise figure of the whole system is equal to the only noise figure of the transponder amplifier (i.e., the first stage of the receiver chain) if the gain of this is much greater than the loss of the path. In practice, a reasonable rule of thumb for the gain of the transponder could be the following:

$$A \geq 10 \left( \frac{4\pi R_3}{G\lambda} \right)^2 \quad (3.23)$$

For obtaining good displacement measurements in both directions with the bistatic configuration,  $L$  should be in the order of magnitude of the distance between radar and target (see (3.12)).

The operative distance of a GBSAR can reach up to 5 km. However, a value between 50 m and 500 m is reasonable in most applications. Therefore, by considering an antenna gain ( $G$ ) of 15 dB and a wavelength of 3 cm (10

GHz), we obtain that the transponder gain (A) could range between 66 dB and 86 dB, with L ranging between 50 m and 500 m.

However, a major problem of any transponder is its possible oscillation. The isolation between the two antennas has to be higher than the gain in order to avoid the oscillation.

A way to increase the isolation between two linearly polarized antennas is to rotate one of them by 90°. For real antennas, the cross-polarization can provide an isolation of 20-30 dB in addition to the co-polarized isolation (see for example the reference in [108]). In the specific case of the transponder described above, the cross-polarization of the antenna pointing at the radar does not affect the bistatic operation if the second receiving antenna of the radar head is cross-polarized with respect to the transmitting antenna (see Figure 3.19).

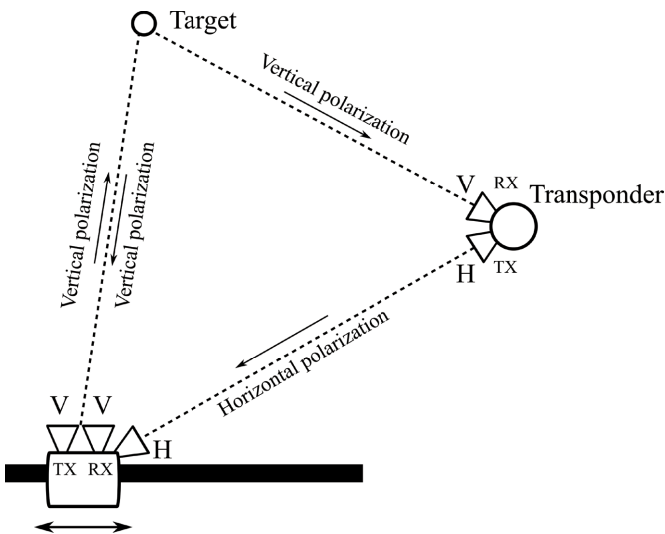


Figure 3.19: Monostatic/bistatic GBSAR with cross-pol transponder.

A further advantage of the cross-polarization is that monostatic and bistatic signals have different polarizations, so possible artefacts due to the mixing of bistatic are greatly mitigated.

This simple solution is not enough in practical application when the distance radar-transponder has to be higher than 100 m.

### Cross-pol Transponder with frequency shifter

Another effective way to avoid the oscillation of a high gain transponder is to shift the output frequency using a suitable frequency shifter. Figure 3.20

shows the scheme of a bistatic radar that uses a transponder with frequency shifter.

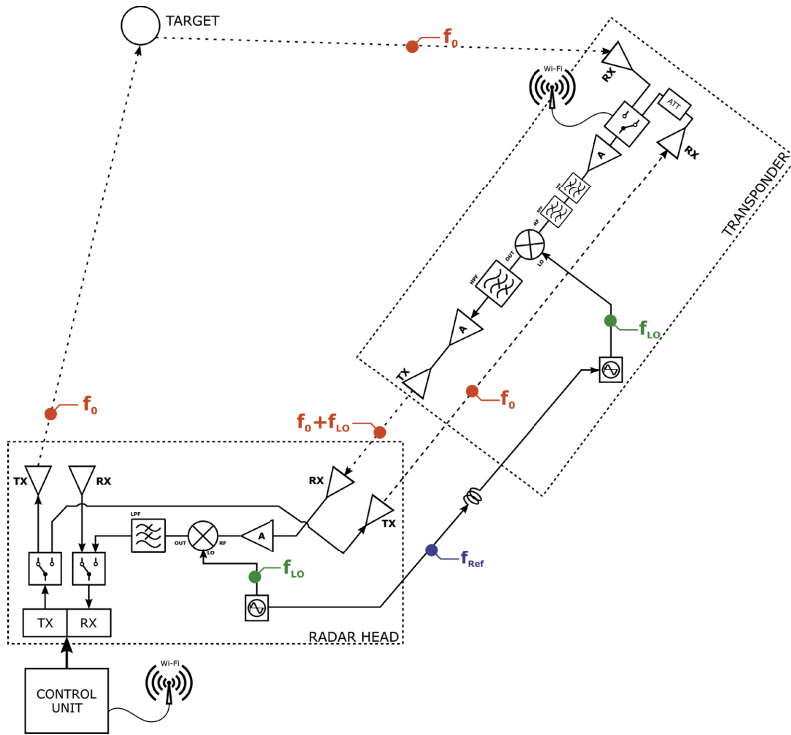


Figure 3.20: Monostatic/bistatic GBSAR with frequency shifter transponder.

The radar operates at central frequency  $f_0$ . The transponder has its own local oscillator (LO). A mixer and a high-pass filter operates as up-converter and shifts the central frequency, so the frequency of the signal transmitted from the transponder to the radar head is  $f_0 + f_{LO}$ . In the radar head, a down-converter (a mixer and a low-pass filter) brings the signal back to frequency  $f_0$ . The two LOs have to be coherent and synchronized, so a reference signal at low frequency  $f_{REF}$  is shared with a cable.

As the cable could move during the movement of the radar head along its mechanical guide, a calibration path is necessary to compensate possible phase shift of the reference signal. Moreover, the calibration provides long-term phase stability and compensates possible phase changes that can occur when the equipment is switched off and on again. Therefore, the radar head has a second transmit channel (selected by a Radio Frequency switch) that provides a calibration signal directly transmitted to the transponder. The

transponder has two receiving antennas (one pointed at the target and the other one pointed at the radar). A RF switch, controlled by a Wi-Fi device, selects between the two antennas (measurement and calibration).

### Test Bench of the System

Figure 3.21 shows the implementation of a up-converter realized with a mixer (SPECWAVEMM96P-L15), a LO at 2.0 GHz (HP 8672A), and a high-pass RF filter (FILTRONIC SB 029). Two band-pass filters (MINICIRCUITS VHF-3800+ and FBP-5.8-11G tuned in the band 5.8 GHz - 10.1 GHz) are used for limiting the input band.

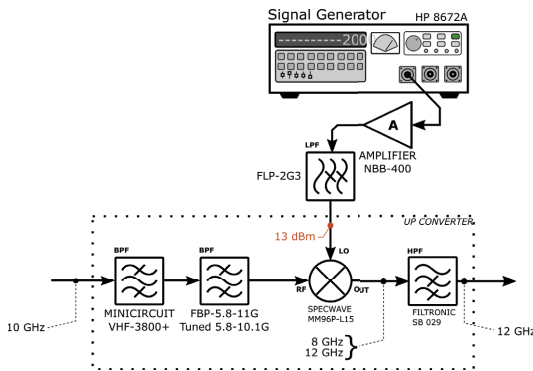


Figure 3.21: Up-converter operating at 10 GHz with 2 GHz frequency shifter.

The isolation of the transponder with the up-converter was measured with the test bench depicted in Figure 3.22.

Figure 3.23 shows the amplitude plot in frequency of the signal before the up-converter (“direct path” in Figure 3.23) and after. The minimum isolation resulted in 71.90 dB, which was enough to prevent the oscillation of an amplifier with gain up 50-60 dB.

The up-converter requires a down-converter at the radar head. In order to test the capability of the up and down-converters to correctly detect the phase of the radar signal, the test bench shown in Figure 3.24 was implemented. In order to simulate the measured differential phase of a target, a manual phase shifter (ARRA 9428B) was inserted between the Vector Network Analyzer (VNA) and the up-converter. The two signal generators at 2.0 GHz were locked up with a 50 m coaxial cable that shared the 10 MHz reference signal.

Figure 3.25(a) shows the phase measured when the signal passes through the up and down-converters and the phase measured directly (bypassing the



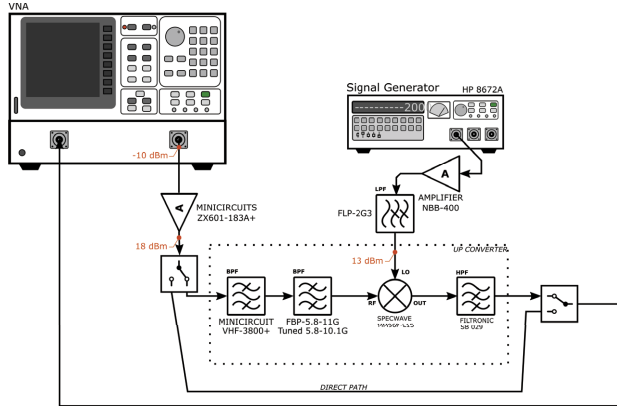


Figure 3.22: Test bench for measuring the isolation of an up-converter operating at 10 GHz with 2 GHz frequency shift.

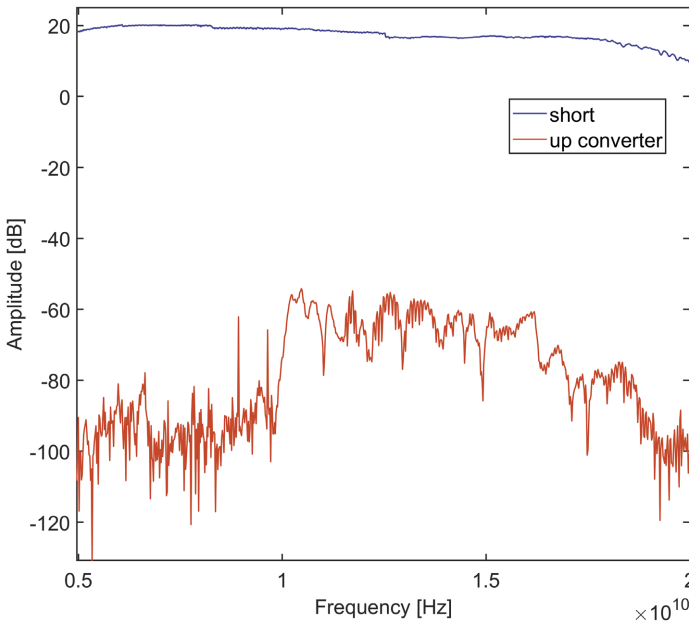


Figure 3.23: Plot in frequency. Red represents the amplitude of the signal through the chain with up and down-converters; blue represents the amplitude of the signal that bypass the chain through the “direct path” [109].

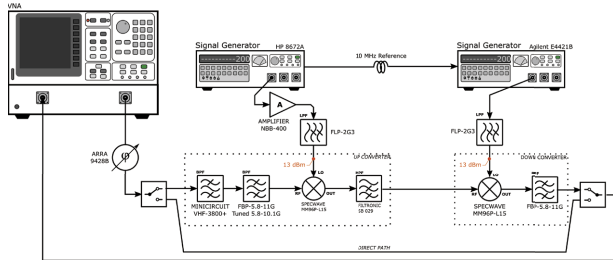
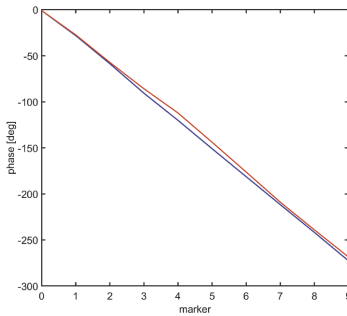


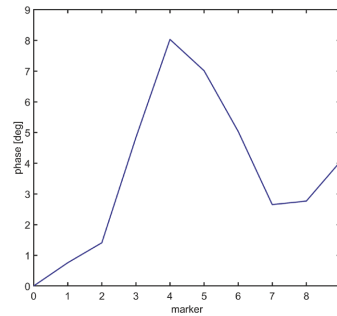
Figure 3.24: Test bench for testing the phase shift detection.

up and down-converters). The x-axis represents the marker number of the manual roll of the phase shifter (ARRA 9428B).

Figure 3.25(b) shows the plot of the differences. The average difference was 2.78 deg. This difference appears to be a systematic error (probably due to nonideality of the mixers and filters), which is compensated by the calibration procedure and which cannot anyway affect the differential measurement of the targets' displacements in any case.



(a) Measured phase by rotating the handle of the manual phase shifter. Red represents the phase measured through the up and down-converters; blue represents the phase measured bypassing the up and down-converters.



(b) Difference between the phase measured when the signal passes through the up and down-converters and the phase measured directly (bypassing the up and down-converters).

Figure 3.25: Phase phase measured when the signal passes through the up and down-converters and the phase measured directly.

## Field test

Figure 3.26 shows the aerial picture of the test site where the radar equipment was installed. The radar was facing a seven-storey building at 130 m distance. The transponder was at the right side of the radar at 22.2 m distance. Figure 3.27 shows a picture taken by the radar position.

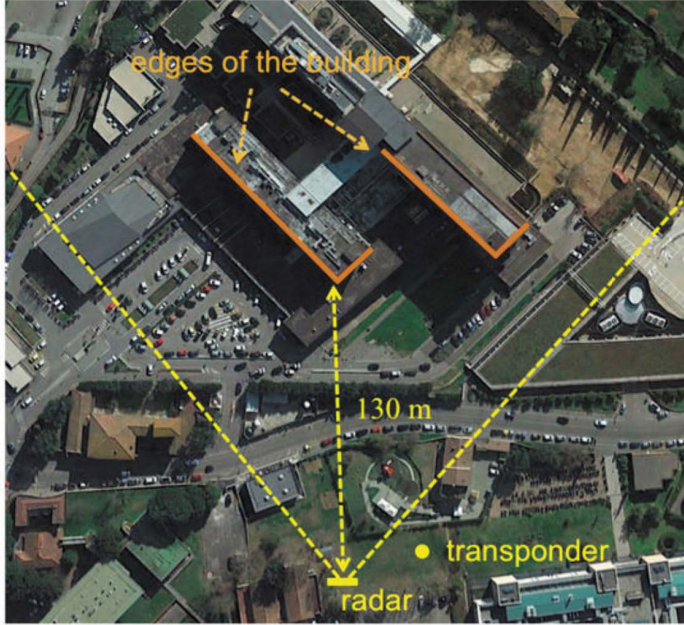


Figure 3.26: Aerial view of the test site [109].

The radar operated in the band 9.915 GHz - 10.075 GHz. The number of frequencies was 801. The length of the mechanical scan (orthogonal to the view direction) was 1.82 m. The number of steps along the scan was 180. The transmitted power was 19 dBm. The measured gain of the transponder (shown in picture in Figure 3.28) was 91 dB.

Figure 3.29 shows the obtained monostatic image. The edges of the building marked in the pictures in Figures 3.26 and 3.27 are well evident. The amplitude scale of the image is in signal to thermal noise ratio (STNR), which has been calculate as outlined in Reference [110]:

$$STNR_{ij} = \frac{|I_{ij}^{(foc)}|^2 P_0 T_{meas} A_{cal}}{k_B T} \quad (3.24)$$

where  $I_{ij}^{(foc)}$  is the radar image focused using the algorithm;  $P_0 = 19$  dBm is the transmitted power;  $T_{meas}$  is the integration time that is given by the time

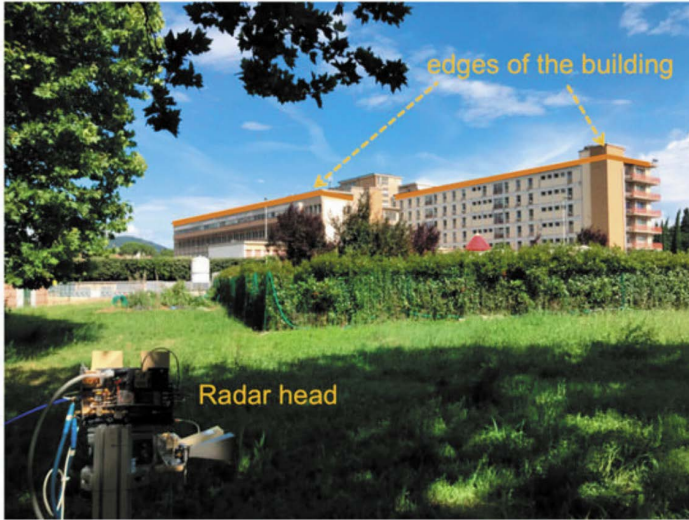


Figure 3.27: Picture taken from the radar position in front of the building in the field of view of the radar [109].

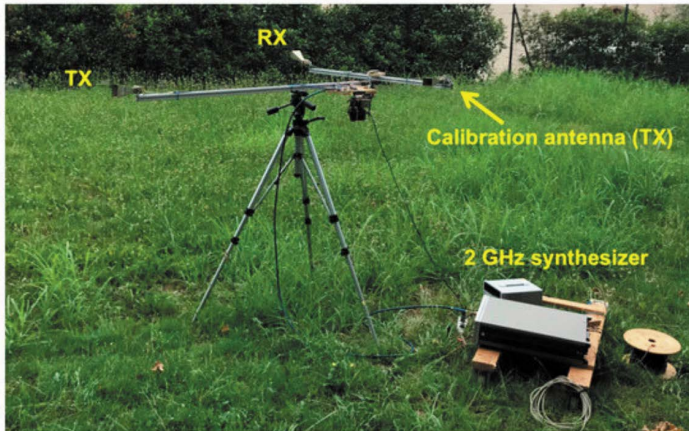


Figure 3.28: Picture of the transponder in the field [109].

of a single continuous wave (CW) measurement multiplied by the number of frequency ( $N_f = 801$ ) and the number of positions ( $N_p = 180$ );  $A_{cal} = 40$  dB is the attenuation of the internal calibration path of the radar head;  $k_B$  is the Boltzmann's constant; T is the absolute temperature (300 K).

In order to test the phase stability of the radar system, 13 images in 7 h were acquired. The interferograms has been calculated between any image

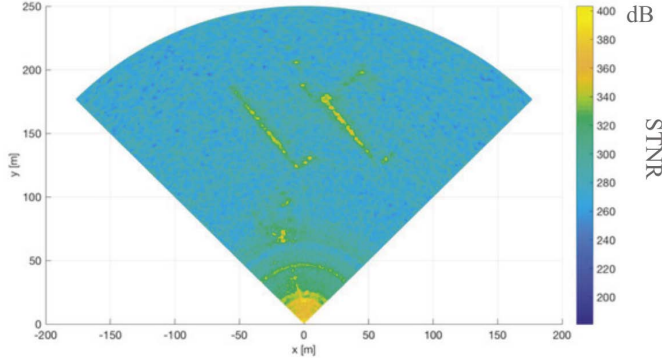


Figure 3.29: Monostatic radar image [109].

and its subsequent image. Figure 3.30 shows one of these interferograms. The pixels relative to the building appear rather stable in-phase.

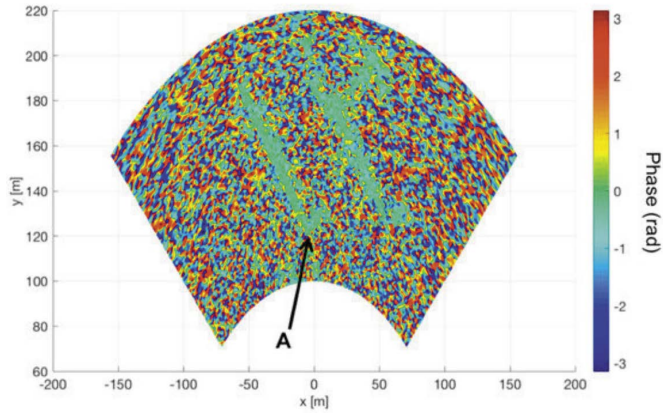


Figure 3.30: Interferogram between two monostatic radar images [109].

The obtained bistatic image is shown in Figure 3.31. The image quality is comparable with the monostatic image.

The amplitude scale of the image in Figure 3.31 is STNR calculated using (3.24), where  $A_{cal}$  is not longer the attenuation of the internal calibration path but is the attenuation of the external bistatic calibration path estimated as follows:

$$\begin{aligned}
 A_{cal} = & \frac{G_{TX-rad\text{ar}}}{4\pi R_3^2} \frac{G_{RX-transp} \lambda_1^2}{4\pi} A_{att} \cdot \\
 & \cdot A \frac{G_{TX-transp}}{4\pi R_3^2} \frac{G_{RX-rad\text{ar}} \lambda_2^2}{4\pi} A_{RX-rad\text{ar}}
 \end{aligned} \tag{3.25}$$

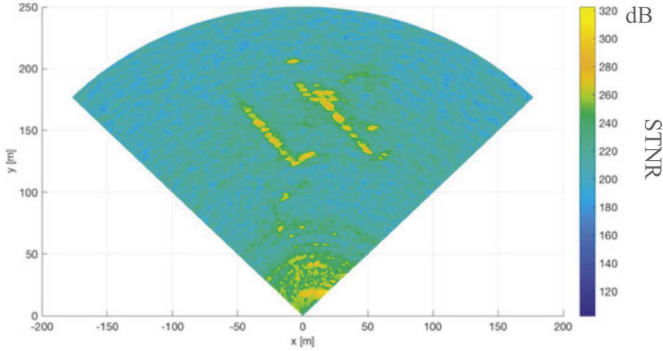


Figure 3.31: Bistatic radar image [109].

With reference to the block scheme in Figure 3.32,  $G_{TX-rad\text{ar}} = 14$  dB is the gain of the transmitting antenna of the radar pointed at the transponder;  $R_3 = 22.2$  m is the radar-transponder distance;  $G_{RX-rad\text{ar}} = 14$  dB is the gain of the receiving antenna of the transponder pointed at the radar;  $\lambda_1$  is the wavelength at 10 GHz;  $A_{att} = -30$  dB is the attenuation of the attenuator in the calibration channel of the transponder;  $A = 91$  dB is the gain of the transponder;  $G_{TX-transp} = 14$  dB is the gain of the transmitting antenna of the transponder pointed at the radar;  $G_{RX-transp} = 14$  dB is the gain of the receiving antenna of the radar pointed at the transponder;  $\lambda_2$  is the wavelength at 12 GHz; and  $A_{RX-rad\text{ar}} = -2$  dB is the gain of frequency shifter of the radar.

Even in bistatic configuration, 13 images were acquired. Figure 3.33 shows one of the interferograms obtained with a couple of calibrated bistatic images.

The point marked with “A” was used to quantify the phase stability both in monostatic and bistatic interferograms. The “apparent” displacement ( $\Delta R$ ) was calculated as (2.22).

As the point marked with A is presumably a stable point, any displacement fluctuation is due to the radar system, atmospheric fluctuation, and environmental temperature changes. Figure 3.34 shows the time series of the three measured displacements of the point A: monostatic, bistatic without calibration, and bistatic with calibration.

The monostatic displacements had mean value of  $-0.1238$  mm and standard deviation of  $0.2753$  mm. These values are in agreement with other measurement campaigns with similar equipment [7], [111], [112].

The calibrated bistatic displacements gave mean value of  $-0.1361$  mm and standard deviation of  $0.3378$  mm, in perfect agreement with monostatic



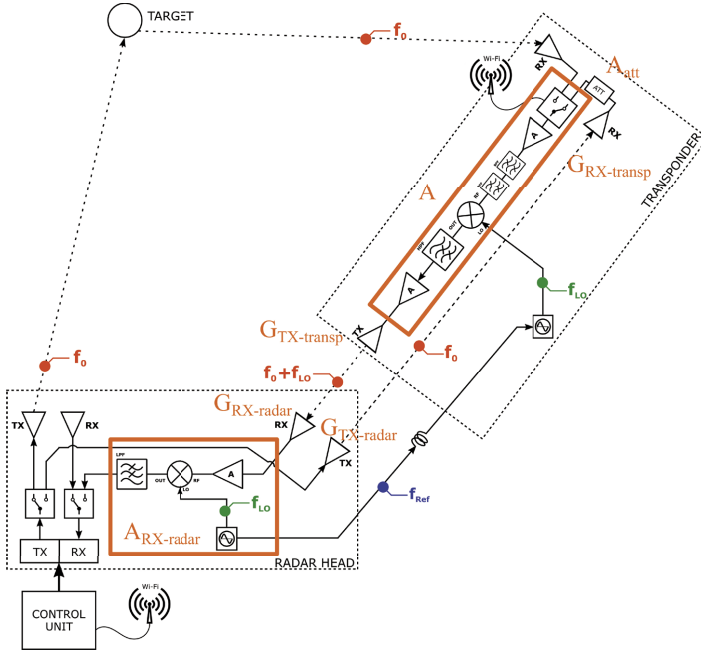


Figure 3.32: Bistatic block scheme.

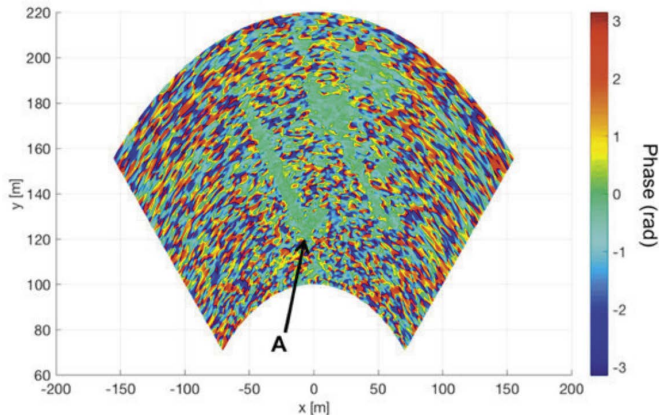


Figure 3.33: Interferogram between two bistatic radar images [109].

measurements. This means that the up and down-frequency converters did not introduce uncontrolled phase shift.

It is important to note that the same values could not be obtained without the calibration path provided by the third antenna of the transponder.

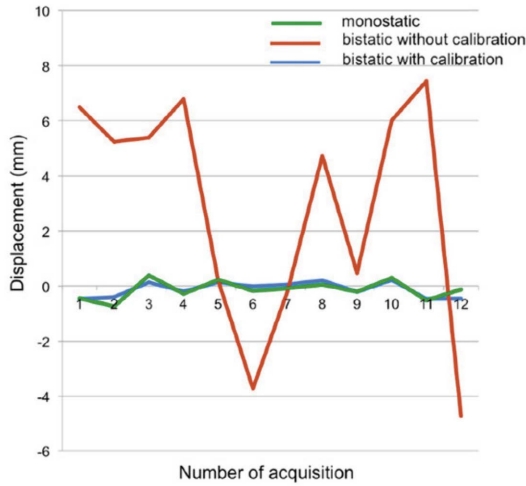


Figure 3.34: Time series of the three measured displacements: monostatic, bistatic without calibration, and bistatic with calibration [109].

Indeed, the bistatic radar image was acceptable even without calibration of the transponder, but the mean value of the displacement of point A resulted in mean value of 2.840 mm with a standard deviation of 4.247 mm, as shown in Figure 3.34. These values prevented any possible use of the interferograms for detecting displacements.

The reason for this phase instability is related to the coaxial cable that connects the radar head to the transponder for sharing the 10 MHz reference. When the radar head moves along the mechanical guide, the movement of the cable gives uncontrolled phase changes.

### Cross-pol long-cable Transponder

An other possible solution to increase the isolation between the two antennas of the transponder is to enlarge the mutual distance. This solution is suitable also when the line of sight between radar and transponder is not present.

In this case the two antennas are cross-polarised, as well as shown in Figure 3.19 and 3.35. An RF cable separates the two antennas of the transponder. The transponder has two amplifiers  $A_1$  and  $A_2$  at the two ends of the cable. The gain of  $A_1$  is 84 dB and the gain of  $A_2$  is 28 dB. The loss of the RF cable is - 30 dB. Therefore, the effective transponder gain is 82 dB.

Figure 3.36 shows the aerial picture of the test site, where the radar equipment was tested. The radar was facing a seven-storey building at 140 m distance. The TX antenna of the transponder was at the right-hand side



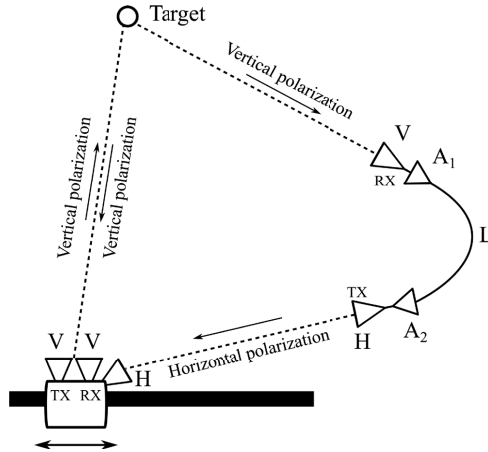


Figure 3.35: Working principle of monostatic/bistatic GBSAR using cross-polarised long-cable transponder.

of the radar at 53 m distance. The RX antenna of the transponder was at 31 m distance from the TX antenna. The radar operated in the band 9.915-10.075 GHz. The number of frequencies was 801. The length of the mechanical scan (orthogonal to the view direction) was 1.82 m. The number of steps along the scan was 180. The transmit power was 19 dBm.

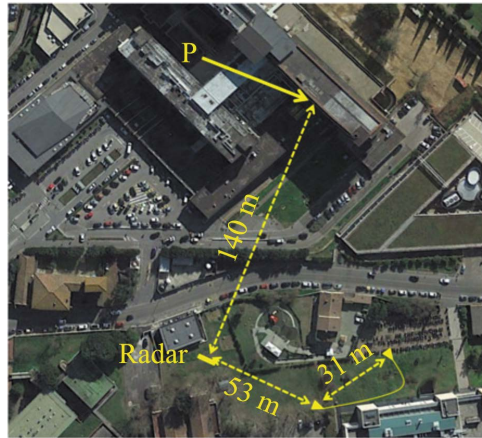
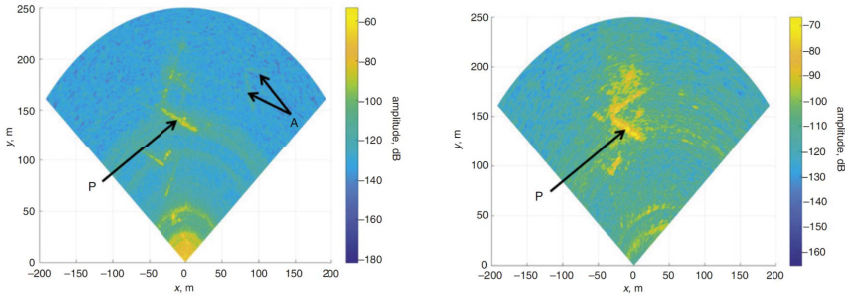


Figure 3.36: Aerial picture of test site.

Figure 3.37(a) shows the obtained monostatic image. The edges of the building are well-evident. The bistatic image is shown in Figure 3.37(b). The arrow indicates the same point P in the aerial picture, the monostatic

image, and the bistatic image.



(a) Monostatic radar image of test site [113]. (b) Bistatic radar image of test site [113].

Figure 3.37: Monostatic/bistatic radar image of test site [113].

The TX antenna of the transponder and the monostatic RX antenna of the radar are cross-polarised, so their coupling should be low. Nevertheless, the transponder (with 82 dB gain) is active even when the radar operates in monostatic modality. Therefore, a weak signal can pass through the transponder producing some artefacts. To verify it, the bistatic signal has been focused with the monostatic algorithm. The obtained image is shown in Figure 3.38. The feature marked with A in the monostatic image (Figure 3.37(a)) can be the “ghost” image of the building. Its amplitude is low (40 dB lower than the highest signal), but it must not be mistaken for a true target.

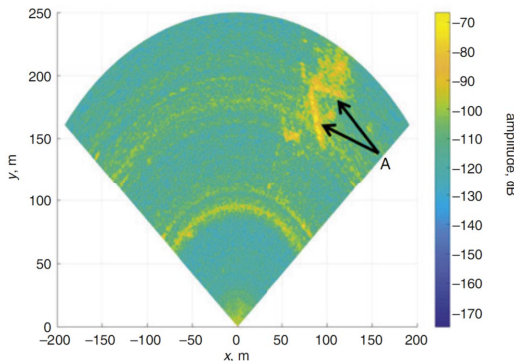


Figure 3.38: Bistatic signal focused with monostatic algorithm [113].

To test the phase stability of the equipment, 12 images (monostatic and

bistatic) in 8 h were acquired and the interferograms between any image and its subsequent image has been calculated. As an example, Figure 3.39 shows one monostatic interferogram. The pixels relative to the building appear rather stable in phase.

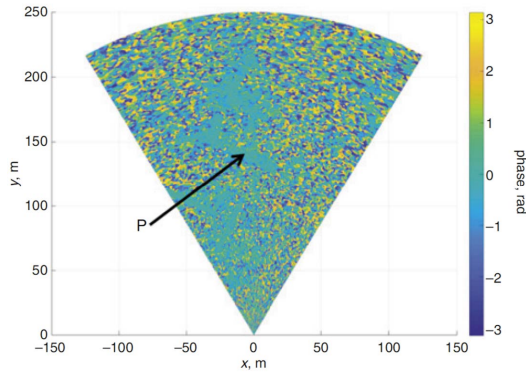


Figure 3.39: Example of monostatic interferogram [113].

To quantify this phase stability, the “apparent” displacement of the point marked with P has been calculated as (2.22).

As the point marked with P is presumably a stable point, any displacement fluctuation is due to the radar system, atmospheric fluctuation, and environmental temperature changes. Figure 3.40 shows the plots of these displacements for monostatic and bistatic configurations. These statistical fluctuations are in good agreement with other measurement campaigns with similar equipment [7], [112].

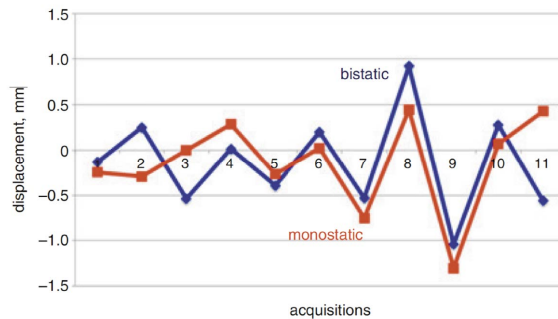


Figure 3.40: Displacement of point P as detected by 11 monostatic and bistatic interferograms [113].

### 3.5 Other applications

#### Bistatic ArcSAR

ArcSAR is a particular implementation of GBSAR, which has been receiving increasing interest in the last years. The great advantage of ArcSAR is its capability to synthesize images at  $360^\circ$  with constant resolution in azimuth [24].

Figure 3.41 shows a sketch of the radar prototype assembled for testing the working principle of bistatic ArcSAR [105]. The vector network analyzer (VNA) HP8720D operated as transceiver providing a continuous wave stepped frequency signal (SFCW) in X-band with central frequency  $f_c = 10$  GHz and bandwidth  $B = 160$  MHz. Two RF cables linked the VNA to the front-end fixed at the tip of the rotating arm.

Before the receiving chain a switcher selected the signal from the monostatic/bistatic antenna. The bistatic antenna (omnidirectional) was connected to the front-end trough a 25 m long RF cable. Two 40 dB amplifiers compensate the cable loss.

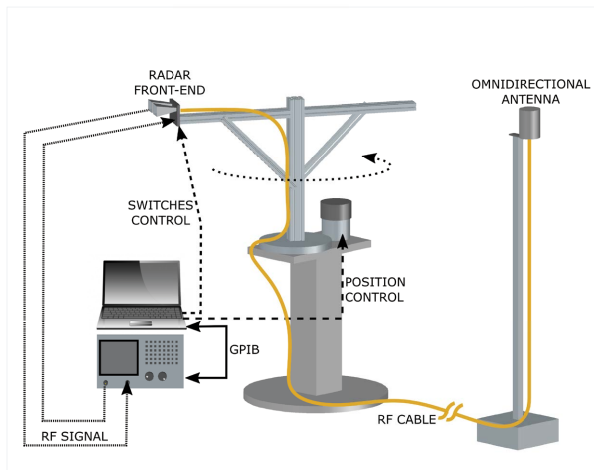


Figure 3.41: Bistatic ArcSAR prototype [105].

For testing the capability to obtain monostatic and bistatic radar images the ArcSAR and the transponder were installed in a garden of the University of Florence. In front and on the side of the radar there was a metallic fence as reported in the map in Figure 3.42.

Figure 3.43 shows the obtained monostatic and bistatic images.

Both images appear of good quality. As expected the resolution and the

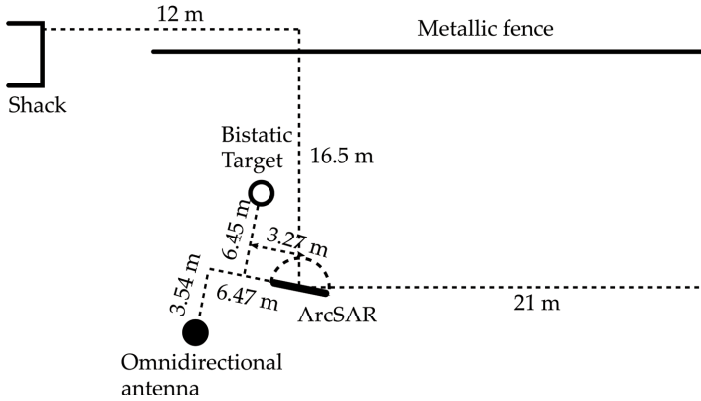
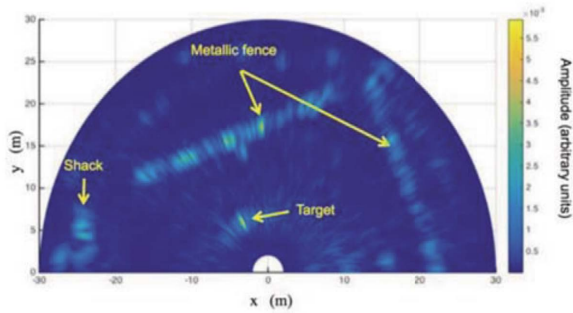
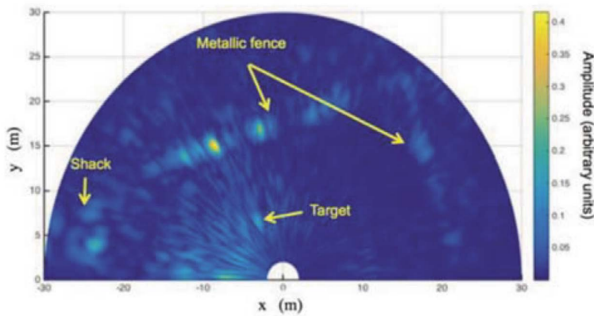


Figure 3.42: Map of the radar installation [105].

signal-to-noise ratio of the monostatic image are better.



(a) Monostatic image [105].



(b) Bistatic image [105].

Figure 3.43: Monostatic/Bistatic ArcSAR image.

With the aim to proof the capability of the bistatic radar to detect two components of the displacement a special target was assembled [105]. The target was mounted over a linear micrometric positioner for optical bench with 0.1 mm nominal accuracy.

The positioner was aligned along the y-axis. A reference couple of images (monostatic and bistatic) was acquired. Aftermath, the positioner was moved of 10 mm along y-axis, and a second couple of images was acquired.

The obtained displacements along y and x were +1.1 mm and -7.61 mm (the nominal values were 0.0 mm and -10 mm). The agreement is not perfect but the working principle has been demonstrated also in this case.

### Dynamic measurement for monitoring slender structures

The bistatic approach can be used also for monitoring slender structures like telecommunications towers, wind turbine towers, bell-towers, minarets, obelisks and other monuments. Indeed this slender vertical structures need both testing before going into service and periodic health monitoring. Their measured responses when subjected to dynamic stimula (e.g. wind or vehicular traffic) is a key parameter for assessing their structural integrity [114].

By using a bistatic approach it is possible to detect, at the same time, two components of the dynamic displacement and it has been possible to identify the axis of symmetry of the structure. Any rotation of this axis can be associated to a possible structural change and can be considered a warning for deeper investigations [115].

Figure 3.44 sketches the working principle of the monostatic/bistatic radar. An interferometric radar positioned in A detects the component of the displacement along the direction target-A (for any point scatterer of the tower). A transponder is positioned in B. The radar in A transmits a signal that is scattered by the tower, bounces through the transponder and comes back to the radar. As the electromagnetic wave is transmitted from A point and received in B point, the radar detects the component of the displacement at the bistatic angle (i.e. the bisector of the angle A-target-B). As the radar is able to perform the two measurements nearly simultaneously (4.3 ms of delay), the effective displacement vector in time (for any point target of the tower) is retrieved.

The radar is a modified version of IBIS-FM (see Figure 3.45), produced by IDS GeoRadar, Pisa, Italy [116]. It operates an FM signal in  $K_U$  bandwidth, with maximum operative bandwidth of 400 Hz. The radar is provided with 2 transmitting (TX) and 2 receiving (RX) channels. The radar can operate in standard configuration, by using one TX and one RX antenna, or

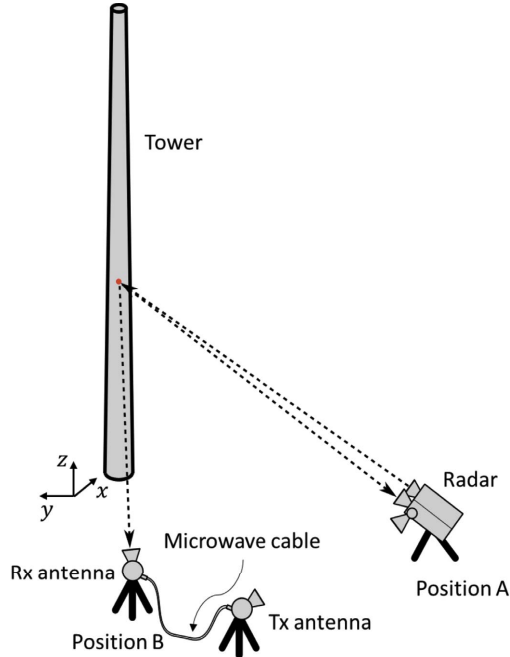


Figure 3.44: Working principle of monostatic/bistatic radar technique applied to the dynamic monitoring of a tower.

in MIMO (Multiple Input Multiple Output) configuration by using all the combinations of the four antennas sequentially. The transponder consists of a RX-antenna, a large-bandwidth amplifier (Gain: 56 dB), a 3.0 m RF-cable (attenuation: -5 dB), and a TX-antenna. The two antennas can be pointed using two tripods.

The radar system has been tested on a telecommunication tower in Florence, Italy. It is steel tower of 35 m height. Its basement has 1.17 m diameter. Figure 3.46 shows the measurement setup: on the left of the transponder, on the right the radar, and in the background the tower. A light wind was the only mechanical stimulus.

The radar operated in MIMO modality. The sampling frequency for each channel was 234.7 Hz. The starting frequency of radar was 17 GHz, the stopping frequency was 17.4 GHz with 1051 time-samples. The range resolution of the equipment was about 0.38 m. The set-up geometry is shown in Figure 3.47. The bistatic angle was  $27.37^\circ$ . The distance between radar and tower's basement was 9.82 m.

For obtaining the radar plot in time the Fast Fourier Transform (FFT) of the radar echo was calculated. In order to retrieve the displacement of

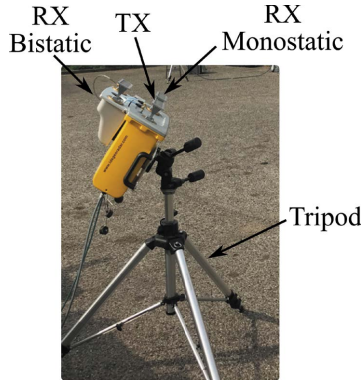


Figure 3.45: Modified version of IBIS-FM.



Figure 3.46: Measurement configuration.

the same target, the monostatic and bistatic plots have been projected on the tower axis by considering the electromagnetic phase history (see (2.18)).

With reference to Figure 3.48, the path between a generic  $k$ -point on the vertical axis is  $d_k^{Mono} = 2R_{(1,k)}$  for the monostatic, and  $d_k^{Bist} = R_{(1,k)} + R_{(2,k)} + L_{cable} + R_T$ , for the bistatic.

Figure 3.49 shows the plots obtained by compensating the paths. They show a notable overlapping, but a perfect correspondence of all peaks is not possible, as each target could have a different response in the monostatic and bistatic configuration. The target at 19.55 m height has been selected



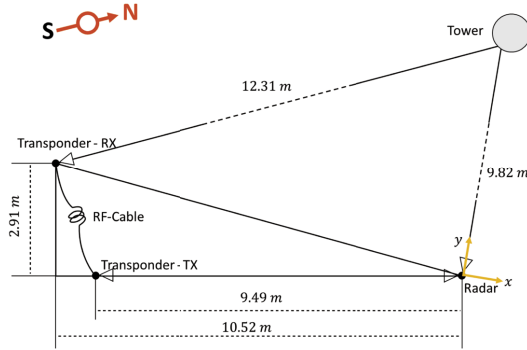


Figure 3.47: Picture of measurement configuration.

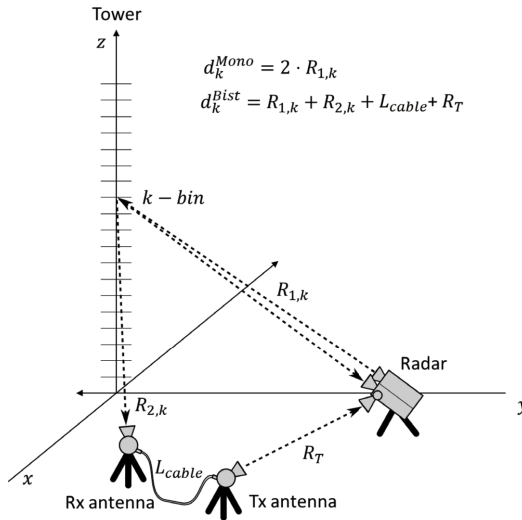


Figure 3.48: Measurement configuration.

for retrieving the displacement.

The duration of the whole measurement was about 15 minutes. Figure 3.50 is an example of only 18 s. We can observe that the two displacements, monostatic and bistatic, are in phase.

For retrieving the natural frequency, the Joint Time Frequency Analysis (JTFA) was applied to the displacement [117]. The Fourier transform of displacement has been evaluated in a sliding-windows of 76.83 s with an overlapping of 90%.

The spectrum of natural frequency (calculated as average in time of the

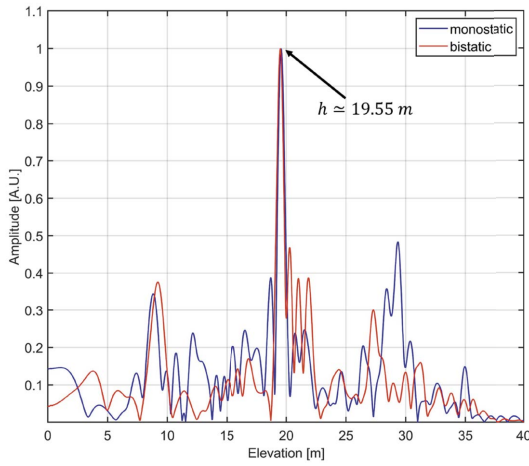


Figure 3.49: Radar plot for monostatic (blue) and bistatic (red).

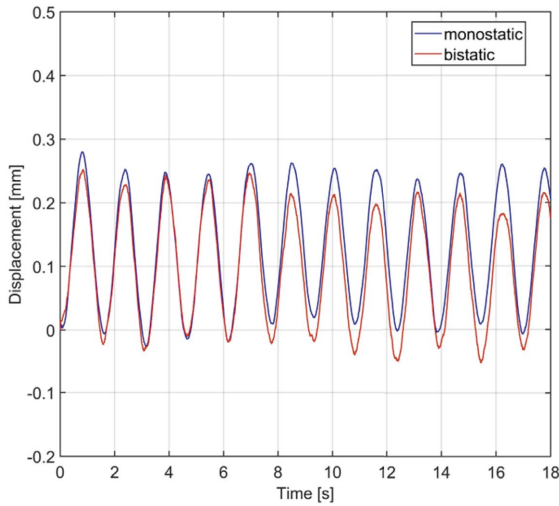


Figure 3.50: Comparison between displacement measured by monostatic (blue) and bistatic (red) in a period of 18 s.

absolute value of JTFA) is shown in Figure 3.51. The natural frequency of the tower was in 0.65 Hz both for monostatic and bistatic.

The x and y components of displacement are shown in Figure 3.52.

In order to find the axis of symmetry of the tower, the x-y components

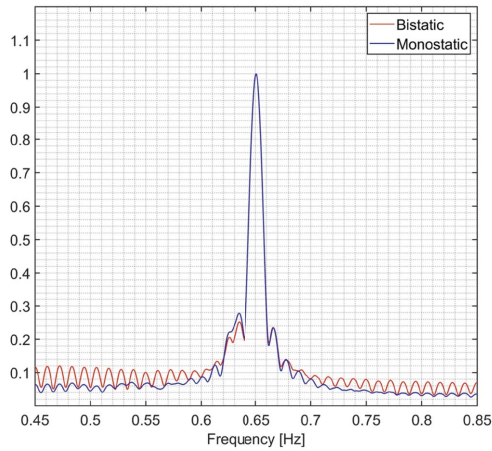


Figure 3.51: Natural frequency of the tower obtained by a time-average of the amplitude of the JTFA (mostatic-blue, bistatic-red).

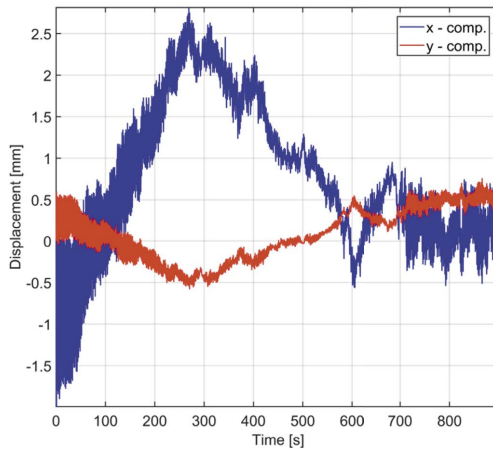


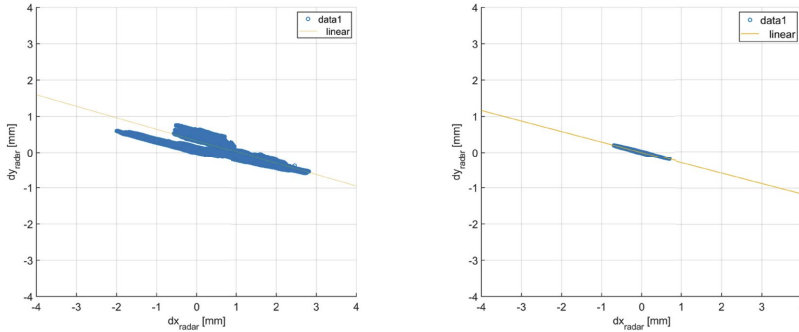
Figure 3.52: x (blue) and y (red) components of displacement of the tower.

have been reported in a scatter plot by considering the full acquisition time.

A liner fit has been applied on the scatter plot in order to estimate the direction of axis of symmetry (Figure 3.53(a)). The axis of symmetry can be estimated as  $(-17.59 \pm 0.05)^\circ$ .

A better estimation of axis of symmetry can be obtained by filtering the signal at the natural frequency using a bandpass Butterworth filter with 6

poles with central frequency 0.65 Hz and band 0.04 Hz. The axis of symmetry of the filtered displacement is shown in Figure 3.53(b). The points stand now precisely along a straight line. So a better evaluation of the axis results to be  $(-16.218 \pm 0.012)^\circ$ . This direction corresponds to  $102.8^\circ$  North.



(a) Axis of symmetry of the tower considering whole bandwidth. (b) Axis of symmetry of the tower filtering the data at the natural frequency.

Figure 3.53: Axis of symmetry of the tower considering whole bandwidth (a) and filtered (b).

### 3.6 Conclusions

In this chapter a GBSAR operating in monostatic and bistatic modality has been presented. A transponder was made use in order to obtain a secondary image, and one other component of displacement, from different point of view.

The radar has been tested with a basic transponder (two antennas and an amplifier) in a controlled environment and it was able to detect two components of displacement.

In order to improve the SNR of the bistatic measurements two enhanced transponders, with an high gain, were presented.

The first transponder made use of a frequency shifter in order to insulate the two antennas and achieved a gain of 91 dB. The artefacts did not affect the measurement with this transponder, but its implementation is rather difficult in practical cases.

The other is a long cable transponder with a gain of 82 dB. This transponder appear to be more practical for most of the uses.

Other application of bistatic technique was presented. A notable application is monitoring slender structures. In this application it was possible to measure the natural axis of a telecommunication tower.

# Compressive Sensing MIMO Radar

The working principle of GBSAR is based on dense spatial sampling (steps smaller than a quarter of wavelength) along the synthetic aperture (usually a linear mechanical guide) as explained in Chapter 1.

Compressive Sensing (CS) is a recent sampling paradigm [118], [119] which asserts that it is possible to recover certain signals from far fewer samples or measurements than traditional methods use. Its basic idea relies on the “sparsity” of the signals of interest (the radar signals typically have this property [120]), and the incoherence of the sensing modality. The latter property is obtained through random sampling.

Generally speaking, CS can be applied in frequency domain (for reducing the number of transmitted frequencies) or in spatial domain (for reducing the number of spatial steps along the synthetic aperture).

In 2010, Huang et al. [121] applied CS to step-frequency through-wall radar that scanned along a horizontal mechanical guide. In 2011, Karlina and Sato [122] proposed to apply CS to GBSAR and they performed simulations, as well as Zonno in 2014 [123]. Yigit [124] extended CS to GB-SAR/ISAR acquisition modality and performed measurements in controlled environment. The interferometric properties of CS-GBSAR have been demonstrated by Giordano et al. [125] in 2015.

At the state of the art, CS techniques appear very promising for GBSAR applications, but all the cited works are relative to radar acquisitions in controlled environments (anechoic chamber or short-range experiments with controlled targets). Therefore, the crucial question is if these techniques are effectively applicable with data acquired in real scenarios, like GBSAR images of large buildings, landslides, open-pit mines, and glaciers.

Furthermore, a few specific questions about the CS methods have to be addressed. The first one is how to choose the orthogonal set of functions (the basis) that are used for recovering the signal. The possible bases are countless. The possible recovery algorithms are many as well. Therefore, a general selection criterion is necessary both for basis selection and recovery method. Another question is: what is an acceptable compression for real data. The claims declared in works that use simulated data or acquisitions performed in very cooperative scenarios are probably too optimistic.

Finally, in previous papers [123], [125] it is possible to note that the  $\varphi$  matrix (see next paragraph for his definition) is built by under-sampling the complete set of data acquired along a single scan. It means that each line could use a different set of positions along the scan. In this article, the  $\varphi$  matrix is built using the same reduced set of data for all the lines. This could reduce the incoherence of sampling (and so the quality of reconstruction), but it is a solution that could be easily implemented with a physical array or with a MIMO (multiple input multiple output), such as in [126], [25], [26].

In this Chapter the theory of Compressive Sensing will be introduced. After, a systematic study about basis, reconstruction algorithm and the acceptable compression value will be presented [127]. Finally, a Compressive Sensing Interferometric MIMO Radar is introduced [30] with some of its application for bridges monitoring [128].

## 4.1 Compressive sensing

Compressive sensing theory states a sparse signal can be recovered by fewer samples than what is required by the Nyquist theorem. With reference to Figure 4.1, a standard GBSAR transmits and receives at  $N$  positions along a linear mechanical guide. The Nyquist theorem requires that the spatial step has to be smaller than a quarter of wavelength ( $\lambda/4$ ) for omnidirectional antennas (this constraint is a bit more relaxed for directional antennas, but it is not essential in the discussion that follows). Let  $E$  be the vector of the  $N$  samples acquired according the Nyquist theorem. A subset of  $M$  random positions is selected between the  $N$  positions. These  $M$  positions are the effective points where the radar-head performs the measurements that will be used for recovering the complete set of  $N$  samples.

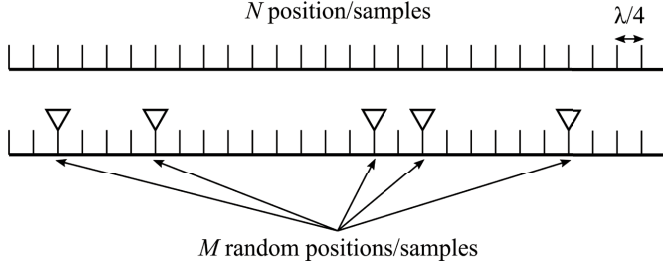


Figure 4.1: Sampling along the linear mechanical guide of a GBSAR.

The next step is to define  $M$  variables ( $y_m$ ) as random linear combinations of the  $N$  samples using only the  $M$  positions as sketched in Figure 4.2.

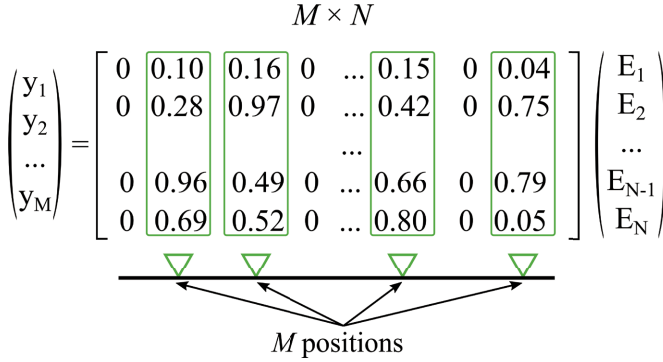


Figure 4.2: Definition of the  $M$  variables  $y_m$ . The number different from zero in the matrix are selected randomly between 0 and 1.

The vector  $y$  of the  $M$  variables can be written as

$$y = \varphi E \quad (4.1)$$

with  $\varphi$  matrix  $M \times N$  as defined in Figure 4.2. It should be noted that the vector  $y$  is a measurable quantity, as it can be calculated from the  $M$  measurements.

A radar signal is often sparse in a suitable set of functions. As an example, an ideal scenario with a single point-target in far field appears as a single peak in the domain of spatial frequencies. Inspired by this idea, we can write the vector  $E$  as

$$E = \psi b \quad (4.2)$$

where  $\psi$  can be

$$\psi = IFFT \left( \begin{bmatrix} 1 & 0 & \cdots & 0 \\ 0 & 1 & \cdots & 0 \\ \vdots & \vdots & \ddots & \vdots \\ 0 & 0 & \cdots & 1 \end{bmatrix} \right) \quad (4.3)$$

and where  $b$  is the vector of the coefficients of spatial Fast Fourier Transform (FFT) of the signal. If the signal is sparse, many coefficient of basis  $b_n$  are almost null.

The FFT or the DCT (discrete cosine transform) should be able to effectively represent ideal point targets, but they could be a too rough approximation for more realistic distributed targets. Wavelets transforms give better results with distributed targets [129]. The possible complete sets of wavelets are countless, so this study has been limited to the most popular sets [129], [130], [131], [132] specifically: Haar wavelets, Daubechies wavelets, biorthogonal wavelet, coiflets, symlets, LeGall wavelets and discrete Mayer wavelets.

By substituting (4.2), in (4.1), the vector  $y$  can be expressed as

$$y = \vartheta b \quad (4.4)$$

with  $\vartheta = \varphi\psi$ . This matrix is the so-called ‘‘dictionary’’.

Equation (4.4) is a linear system with many more variables than equations. It is an ill-posed system but it can be solved with a suitable recovery method. The most popular are: l1-minimization [133], l2-minimization [134], and orthogonal matching pursuit [135]. Using one of these methods, the vector  $b$  is recovered, so the  $E$  vector of  $N$  samples is obtained by (4.2).

The procedure described above has to be repeated for each frequency for obtaining the matrix  $E_{k,i}$ , with  $k$ -index ranging from 1 to  $N_f$  and  $i$ -index ranging from 1 to  $N$ .

The next step is to focus the matrix  $E_{k,i}$  using the back-propagation algorithm described in Chapter 2.

## 4.2 Compressive sensing for GBSAR

In this section a systematic investigation of the possible dictionaries and recovery algorithms is presented.

In order to estimate the quality of the recovered images the peak signal-noise ratio (PSNR) was calculated. The PSNR is defined as

$$PSNR = 10 \log_{10} \left( \frac{\max(|I_{i,j}|^2)}{\frac{1}{mn} \sum_{i=1}^m \sum_{j=1}^n |I_{i,j} - R_{i,j}|^2} \right) \quad (4.5)$$



where  $R_{i,j}$  is the focused reference GBSAR image obtained from the data sampled according to Nyquist theorem without application of CS techniques;  $I_{i,j}$  is the image obtained using the CS techniques. Both images are complex matrix  $m \times n$ . As rule of thumb, images with PSNR lower than 20- 25 dB appear of low quality, with features hardly recognizable [136].

## Simulations

First of all the minimum compression has to be founded. For this reason, the CS algorithms have been preliminary tested with the simulation of a single target at 150 m distance in front of radar. The used parameters were: initial frequency  $f_1 = 9.915$  GHz, final frequency  $f_2 = 10.075$  GHz, number of frequencies  $N_f = 801$ , length of the mechanical scan  $L = 1$  m, number of samples (according to Nyquist theorem)  $N = 100$ .

The basis used was the Haar wavelets. The recovery method was l2-minimization (this choice of Haar wavelets will be motivated in the experimental section, l2-minimization has been selected because it works even with a number of variable smaller than the number of equations, nevertheless the choice of both basis and recovery method is not essential for the discussion that follows). The PSNR has been calculated for an image  $200 \times 200$  pixels in polar coordinates. The range limits were 100 m and 200 m. The azimuth limits were -30 deg and +30 deg.

Figure 4.3 shows the plots of PSNR versus  $M/N$ . Each PSNR was calculated as the average of 25 random iterations and the standard deviation of each value is reported in the plot (blue line). It is interesting to note that for  $M/N > 0.3$ , the PSNR increases linearly of 2.4 dB for each 10% increase of  $M/N$ . This is a notable result that is also true for simulations of more complex scenarios (several targets), using different measurement parameters, different dictionaries, and different recovery methods, and in experimental data too. Note that PSNR does not tend to infinity for  $M = N$ , but it stops at about 37 dB. The reason of it is related to the limited size of the  $\varphi$  matrix.

As it is known, the CS reconstruction relies on the incoherence of both random sensing and the random coefficients of the matrix  $\varphi$ . When  $M = N$ , the sensing is no longer incoherent, but the incoherence of the  $\varphi$  coefficients persists and limits the quality of reconstruction. The  $\varphi$  coefficients are uniformly distributed random numbers between 0 and 1. When  $M = N$ , the number of elements is  $N \times N = 100 \times 100 = 10000$ , the sum of 10000 uniformly distributed random numbers between 0 and 1 gives exactly 37.0 dB, that is just the maximum PSNR obtained in Figure 4.3.

The noise can affect both PSNR and displacement retrieved by inter-

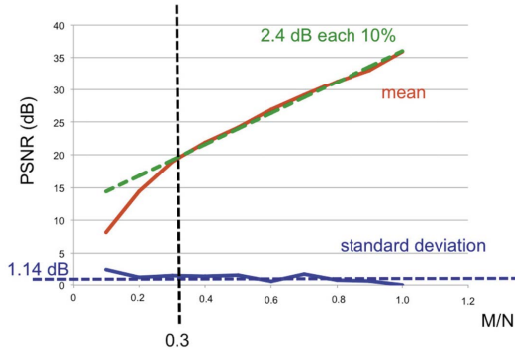


Figure 4.3: PSNR in function of  $M/N$  (simulated data) [127].

ferometry. In order to verify/evaluate it, we have repeated the simulations reported above with controlled Gaussian noise. Figure 4.4 shows the PSNR versus  $M/N$  calculated with different SNR values (the SNR reported in the plots is relative to one single measurement specified by one single frequency and one single position along the mechanical guide). Each PSNR value of the plots in Figure 4.4 is calculated as the average of 12 random iterations. As expected, by reducing the SNR the PSNR decreases. When the SNR of a single measurement is  $> 0$ , the PSNR is practically equal to the PSNR without noise calculated in the previously.

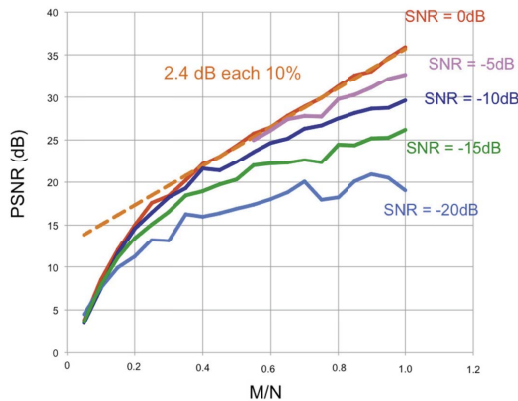


Figure 4.4: PSNR in function of  $M/N$  and SNR (simulated data) [127].

The noise can give an error in the displacement retrieved by interferometry. In order to verify/evaluate it, we have estimated the phase error ( $\Delta\phi$ ) and we have converted it in displacement error ( $\Delta R$ ) using the well-

known relationship (2.22).

Figure 4.5 shows the estimated error in function of SNR. Each PSNR value is calculated as the average of 40 random iterations. For  $N_A/N = 1$  the error plot in function of SNR overlaps perfectly the plot of the error calculated without CS that, in log scale, is a straight line with slope -1. As expected, for  $M/N = 0.5$  the error increases of 3dB and for  $M/N = 0.1$  the error increases of 10 dB.

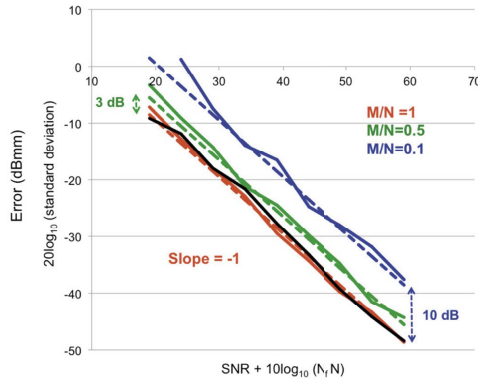
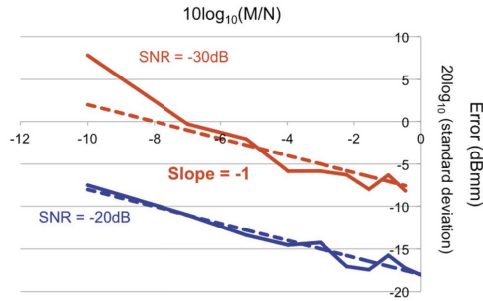


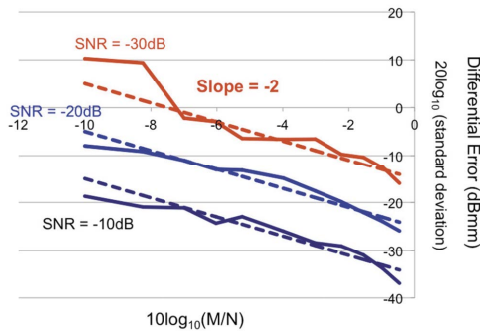
Figure 4.5: Displacement error in function of SNR for different  $M/N$  (simulated data). The dark line is the displacement error calculated without CS technique [127].

When  $M/N$  increases, the number of samples increases too. So the error should decrease. This intuitive idea has been verified with a simulation. Figure 4.6(a) shows how the error decreases increasing  $M/N$ , for two different values of the SNR. Both the plots are approximately straight lines with slope -1.

Generally speaking, the interferometric error could not depend only on Gaussian noise (i.e. on thermal noise). In that case, calculating the error in function of  $M/N$  does not make much sense, as it could be hard to obtain a straight line. On the contrary, the differential error (i.e., the error with respect to the image obtained using the CS with 100% of the samples) is expected to have a linear behaviour (in log scale). Figure 4.6(b) shows the differential displacement in function of  $M/N$  for three different SNR. It is evident that the plots can be approximated as straight lines with a slope of -2.



(a) Displacement error in function of  $M/N$  for different SNR (simulated data) [127].



(b) Differential displacement error in function of  $M/N$  for different SNR (simulated data) [127].

Figure 4.6: Displacement error and differential displacement error in function of  $M/N$  for different SNR (simulated data) [127].

### Experimental application

#### Sesto Fiorentino Campus

The CS techniques have been experimentally tested in a controlled scenario at the University of Florence (named Sesto Fiorentino Campus). A single metallic target, provided with a micrometric linear translator, has been positioned in front of the radar equipment at 150 m distance in a large flat garden, as shown in the pictures in Figure 4.7. The radar operates in monostatic modality.

The measurement parameters were the same used in the simulations. The acquired experimental data have been used for testing the most popular bases and recovery methods. Specifically we used discrete cosine transform (dct), fast Fourier transform (fft), the Haar wavelets (haar), the Daubechies wavelets from order 2 to order 10 (db2-db10), seven biorthogonal wavelets

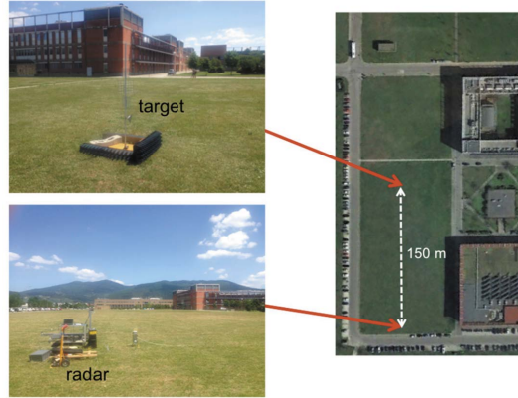


Figure 4.7: Experimental test site Sesto Fiorentino Campus [127].

(bior1.3, bior2.2, bior2.6, bior3.1, bior3.5, bior3.9, bior5.5), the “coiflets” from order 1 to 5 (coif1-coif5), the “simlets” from order 2 to 8 (sim2-sim8), LeGall wavelets (legal5.3), the discrete Meyer wavelets (dmey). As recovery methods, we used l1-minimization (L1), l2-minimization (L2), and orthogonal matching pursuit (OMP).

Table 4.1 reports the obtained PSNR for  $M/N = 0.5$  and  $M/N = 0.33$ . The PSNR has been calculated for an image  $200 \times 200$  pixels in polar coordinates. The range limits were 100 m and 200 m. The azimuth limits were  $-30^\circ$  and  $+30^\circ$ .

In the table, the highest (in bold) and the lowest (in italic bold) values were highlighted. Using 50% of data, PSNR varies between 26.01 dB (Haar wavelets, OMP) and 21.89 dB (FFT, OMP). Using 30% of data, PSNR varies between 20.03 dB (Haar wavelets, OMP) and 15.87 dB (Bior3.1 wavelets, OMP).

In simulated data, it is possible to note that PSNR increases linearly of 2.4 dB for each 10% increase of  $M/N$ . This relationship is perfectly confirmed also for these experimental data as shown in Figure 4.8.

For evaluating the interferometric error 100 measurements in 96 h were acquired. By considering one pixel associated to a stable point of one building at about 200 m in the background, the standard deviation of the displacement retrieved by interferometry has been evaluated. Figure 4.9 shows the obtained values varying  $M/N$ . The error is rather constant. It means that thermal (Gaussian) noise is not the main source of error. The effective contribution of thermal noise is more evident in the plot of the differential error (Figure 4.10) that confirms the error (in log scale) linearly decreases with slope -2, increasing the  $M/N$  (in log scale), as predicted by simulation.

	50%			30%		
	L1 (dB)	L2 (dB)	OMP (dB)	L1 (dB)	L2 (dB)	OMP (dB)
Dct	22.92	22.89	22.29	18.77	19.02	19.62
Fft	22.61	22.73	<b>21.89</b>	17	17.16	17.45
Haar	24.83	24.83	<b>26.01</b>	18.3	18.3	<b>20.03</b>
Db2	24.32	24.29	24.32	18.14	18.13	18.13
Db3	24.32	24.33	24.36	17.68	17.66	18.01
Db4	23.97	23.97	23.67	18.22	18.23	17.98
Db5	23.71	23.73	23.1	17.49	17.48	17.35
Db6	23.87	23.9	22.74	17.76	17.77	17.98
Db7	23.24	23.25	22.6	17.41	17.45	16.11
Db8	23.24	23.23	22.48	17.71	17.7	17.82
Db9	23.26	23.27	21.46	17.71	17.72	17.82
Db10	23.04	23.07	23.48	17.74	17.74	18.52
Bior1.3	24.65	24.64	25	18.16	18.16	19.51
Bior2.2	24.45	24.45	23.53	17	16.99	16.96
Bior2.6	24.22	24.21	23.37	17.65	17.65	17.37
Bior3.1	23.51	23.51	22.66	17.39	17.39	<b>15.87</b>
Bior3.5	24.29	24.28	23.5	17.99	17.99	17.21
Bior3.9	24	24.04	23.67	17.6	17.6	17.67
Bior5.5	23.97	23.98	23.62	18.04	18.07	18.23
Coif1	24.04	24.09	23.52	17.71	17.72	17.25
Coif2	24.2	24.21	24.04	16.84	16.84	17.26
Coif3	23.72	23.72	23.27	17.39	17.39	17.36
Coif4	23.47	23.47	22.74	17.49	17.51	17.52
Coif5	23.28	23.18	22.79	17.05	17.04	16.9
Sym2	24.32	24.29	24.32	18.14	18.13	18.13
Sym3	24.32	24.33	24.36	17.68	17.66	18.01
Sym4	24.42	24.44	24.08	17.29	17.28	17.04
Sym5	23.77	23.77	23.62	17.63	17.64	17.54
Sym6	24.24	24.15	23.78	17.64	17.64	16.94
Sym7	24.26	24.27	24.18	18.02	18.03	17.68
Sym8	24.1	24.11	23.53	17.94	17.94	17.04
Legall5.3	24.17	24.17	24.49	18.31	18.3	18.51
Dmey	23.6	23.6	23.56	17.93	17.94	17.96

Table 4.1: PSNR calculated with different bases and recovery methods for experimental data acquired at the test site Sesto Fiorentino Campus.

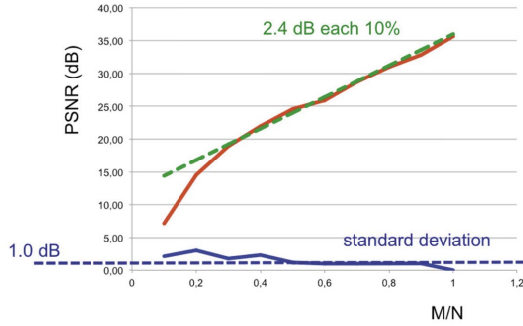


Figure 4.8: PSNR in function of  $M/N$  (data acquired at the experimental test site Sesto Fiorentino Campus) [127].

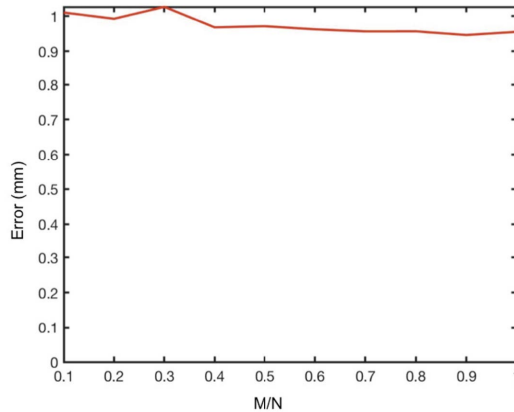


Figure 4.9: Displacement error in function of  $M/N$  for a stable point in the test site Sesto Fiorentino Campus [127].

The metallic target was provided with a micrometric positioner able to translate it with a nominal accuracy of 0.1 mm. So, we performed 20 radar acquisitions by moving the target of 1 mm forward the radar after each acquisition. Figure 4.11 shows the cumulative displacement detected by interferometry using 100% of data without CS, using 100% of data with CS, using 50% of data with CS, and using 30% of data with CS. The four plots are practically overlapping. Figure 4.12 shows the plots of the differences. In the worst case (CS with 30% of data) the error is lower than 25  $\mu\text{m}$ .

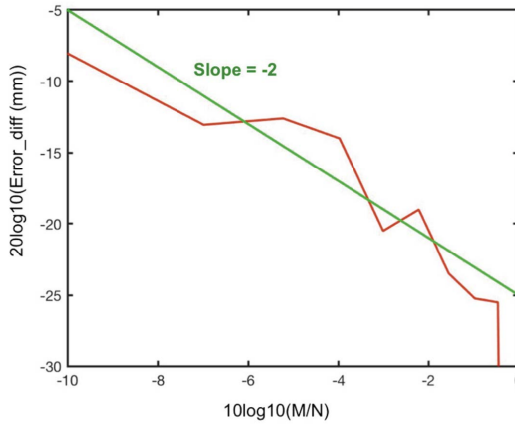


Figure 4.10: Differential displacement error in function of  $M/N$  for a stable point in the test site Sesto Fiorentino Campus [127].

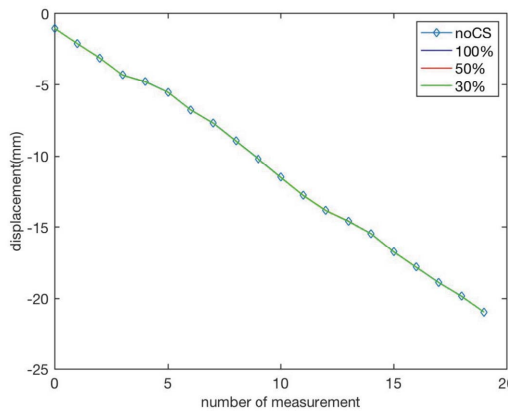


Figure 4.11: Cumulative measured displacement of the controlled metallic target at the test site Sesto Fiorentino Campus [127].

### A Seven-Storey Building

In order to test the application of CS techniques in an operative scenario representative of an urban environment, we performed radar measurements using as target the seven-storey building shown in Figure 4.13.

The measurement parameters were: initial frequency  $f_1 = 9.915$  GHz, final frequency  $f_2 = 10.075$  GHz, number of frequencies  $N_f = 801$ , length of the mechanical scan  $L = 1.8$  m, number of samples (according to Nyquist theorem)  $N = 180$ . The obtained radar image (without application of CS



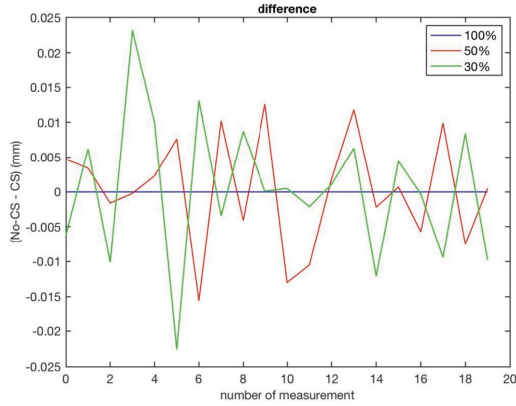


Figure 4.12: Differences between displacements detect through 100% CS, 50% CS, 30% and displacements detected using 100% of data without application of CS techniques (test site Sesto Fiorentino Campus) [127].

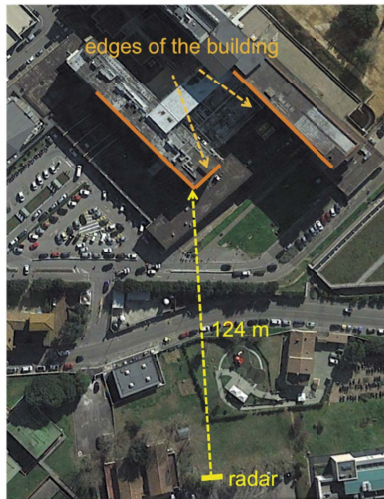


Figure 4.13: Aerial picture of the seven-storey building used as urban test site [127].

techniques) is shown in Figure 4.14

As well as for simulated data, and for the experimental data acquired at the “Sesto Fiorentino Campus” test site, the PSNR increases linearly of 2.4 dB for each 10% increase of  $M/N$  and this relationship has been perfectly confirmed also for these experimental data (for sake of brevity the graph is

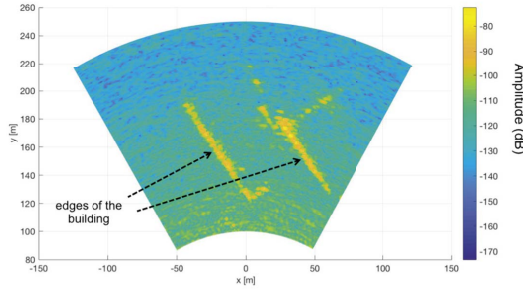


Figure 4.14: Radar image (without application of CS techniques) of the building shown in Figure 4.13 [127].

not reported).

The PSNR for  $M/N = 0.5$  and  $M/N = 0.3$  has been calculated (Table 2 in [127]). Using 50% of data, PSNR varies from 22.78 dB (db2 wavelets, OMP) to 8.19 dB (dct, OMP). Using 30% of data, the PSNR ranges between 19.12 dB (db5 wavelets or sym2 wavelets, OMP) and 1.80 dB (fft, OMP).

### An Open-Pit Copper Mine

The most popular use of the GBSAR systems is the monitoring of open-pit mines. Therefore, the CS techniques has been tested to a representative case study of a copper mine in South America. The measurement parameters were: initial frequency  $f_1 = 17.1$  GHz, final frequency  $f_2 = 17.3$  GHz, number of frequencies  $N_f = 5333$ , length of the mechanical scan  $L = 1.275$  m, number of samples (according to Nyquist theorem)  $N = 256$ . The obtained radar image (without application of CS techniques) is shown in Figure 4.15.

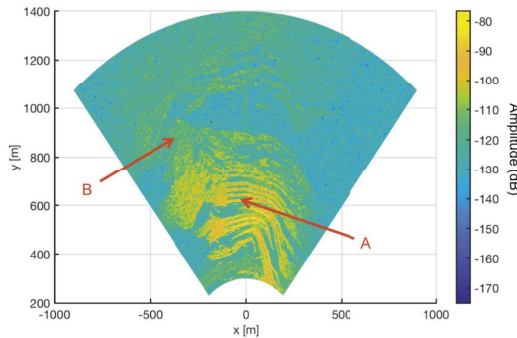


Figure 4.15: Radar image (without application of CS techniques) of a copper mine in South America [127].

As well as for previous data, the PSNR increases linearly of 2.4 dB for each 10% increase of  $M/N$  and this relationship has been perfectly confirmed also for these experimental data (for sake of brevity the graph is not reported).

Also in this case the PSNR for  $M/N = 0.5$  and  $M/N = 0.3$  has been evaluated (Table 3 in [127]). Using 50% of data, PSNR varies from 29.95 dB (Haar wavelets, OMP) to 17.25 dB (FFT, L2). Using 30%, the PSNR ranges between 29.44 dB (Haar wavelets, OMP) and 9.33 dB (FFT, OMP).

Figure 4.16 shows an interferogram between two images (focused without application of CS techniques) taken at different time. It shows a clear movement on the left side of the slope. In order to test the capability of the CS techniques to reconstruct interferograms, it is applied to 50% of data (Figure 4.17(a)) and to 33% of data (Figure 4.17(b)) using Haar wavelets and OMP.

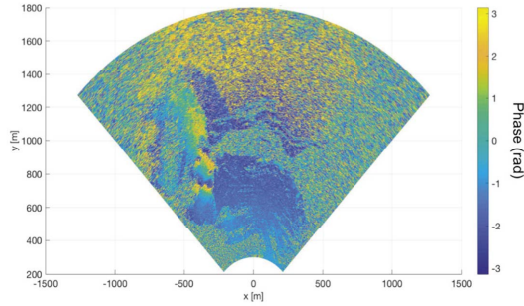
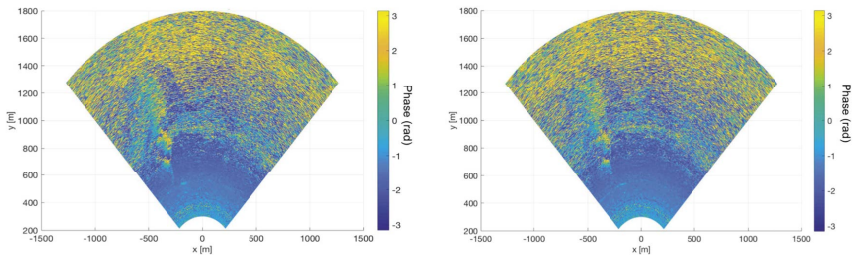


Figure 4.16: Interferometric image (without application of CS techniques) of a copper mine in South America [127].

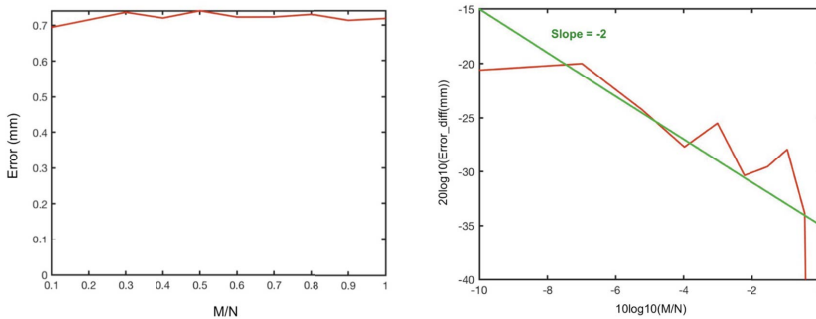


(a) Interferometric radar image obtained with 50% of data and CS [127].

(b) Interferometric radar image obtained with 33% of data and CS [127].

Figure 4.17: Interferometric radar image obtained with 50% and 33% of data and CS [127].

In order to evaluate the interferometric error, 41 measurements acquired in 4 h and 20 min have been processed. By considering one pixel associated to one stable point (without visible fringes), the standard deviation of the displacement retrieved by interferometry has been evaluated. The point is labelled with letter A in Figure 4.15. Figure 4.18(a) shows the error (calculated as standard deviation) of the displacement at the stable point A varying M/N. The error is rather constant. It means that thermal (Gaussian) noise is not the main source of error. The effective contribution of thermal noise is more evident in the plot of the differential error (Figure 4.18(b)). It confirms that the error linearly decreases (in log scale) with slope -2, increasing the M/N (in log scale), as predicted by simulation.



(a) Displacement error in function of M/N for a stable point in the open pit mine [127].

(b) Differential displacement error in function of M/N for a stable point in the open pit mine [127].

Figure 4.18: Displacement and differential displacement error in function of M/N for a stable point in the open pit mine [127].

In order to verify the capability of CS to detect a cumulative displacement, we have taken into account the point B in Figure 4.15 where several fringes are evident in the interferograms (see Figure 4.16). Figure 4.19 shows the plot obtained without CS and the plot obtained with CS applied to 100% of data are perfectly overlapping. The CS plots with 50% and 30% of data tend to underestimate the displacement.

## A Glacier

As test-site representative of a natural scenario we considered the “Belvedere” glacier in the Italian Alps. The data was acquired during a measurement campaign in 2006, whose details are reported in [137], [138], [139]. The measurement parameters were:  $f_1 = 5.97$  GHz,  $f_2 = 5.99$  GHz,  $N_f = 801$ ,

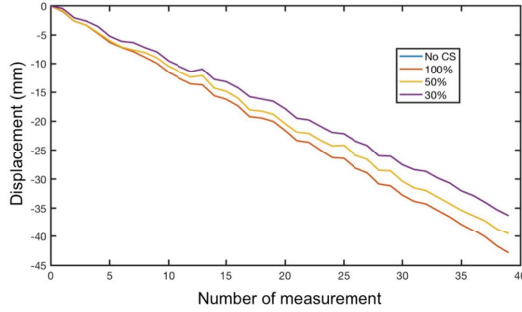


Figure 4.19: Cumulative measured displacement of the point B in the open pit mine [127].

$L = 1.71$  m,  $N = 141$ . The obtained radar image (without application of CS techniques) is shown in Figure 4.20.

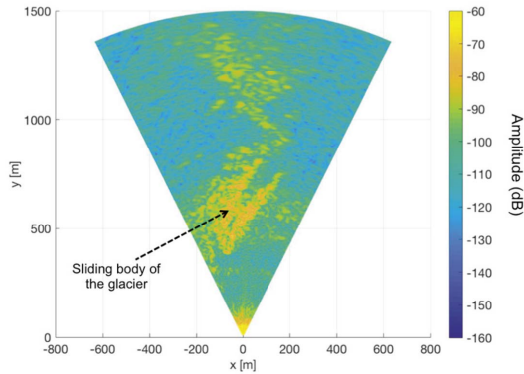


Figure 4.20: Radar image (without application of CS techniques) of a glacier in the Italian Alps [127].

As well as for previous data, we verified that PSNR increases linearly of 2.4 dB for each 10% increase of  $M/N$  and this relationship has been perfectly confirmed also for these experimental data.

The PSNR has been calculated for an image  $200 \times 200$  pixels in polar coordinates. The range limits were 350 m and 1000 m. The azimuth limits were  $-25^\circ$  and  $+25^\circ$ . Using 50% of data, PSNR varies from 21.16 dB (Haar wavelets, OMP) to -3.50 dB (DCT, L2). Using 30%, the PSNR ranges between 16.52 dB (Haar wavelets, OMP) and -5.09 dB (FFT, L1).

In order to verify the capability of CS to detect a cumulative displacement, we have taken into account a pixel inside the sliding body of the

	Campus	Building	Mine	Glacier
$f_1$ [GHz]	9.915	9.915	17.1	5.97
$f_2$ [GHz]	10.075	10.075	17.3	5.99
$N_f$	801	801	5333	801
$L$ [m]	1	1.8	1.275	1.71
$L$ [m]	1	1.8	1.275	1.71
$N$	100	180	256	141
PSNR max 50% [dB]	26.01	22.78	29.95	21.16

Table 4.2: Parameters of each measurement campaign and the highest value of PSNR obtained using 50% of data.

glacier. Figure 4.21 shows the plots obtained without CS and with CS applied to 100%, 50%, and 30% of data. The plots are almost perfectly overlapping.

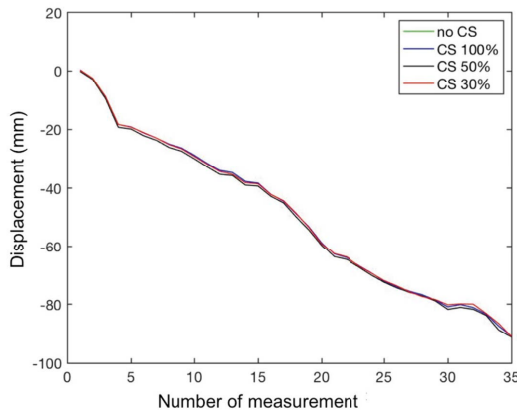


Figure 4.21: Radar image (without application of CS techniques) of a glacier in the Italian Alps [127].

Table 4.2 resumes the parameters of each measurement campaign and the highest value of PSNR obtained using 50% of data.

The CS techniques are able to reconstruct GBSAR images of good quality (PSNR > 20-30 dB) with almost 30 – 40% of data.

Nevertheless, the quality of reconstruction depends on the selected basis and recovery method. In a test site with just one single strong target, the best image has been obtained with FFT and OMP. In an urban scenario the best choice has been Daubechies wavelets and OMP. For an open-pit mine the highest quality image has been reconstructed with Haar wavelets and

OMP. For a natural slope (a glacier) the optimal choice has been again Haar wavelets and OMP. In all cases, Haar wavelets with OMP gave good results (even if not always the best).

Therefore, the Haar wavelets with OMP is a reasonable choice for most practical cases. Furthermore, we found that CS reconstruction does not worsen significantly the interferometric error. The plots of the cumulative displacement recovered with 100%, 50%, and 30% of data overlaps almost completely the plot obtained without application of CS techniques.

All these findings constitute the basic scientific starting point for designing optimal sparse array or multiple-input multiple-output (MIMO) radar able to exploit the CS techniques.

### 4.3 Compressive Sensing MIMO Interferometric Radar

The MIMO radar proposed in this Chapter exploits the random distribution of 4 transmitting (TX) antennas and 4 receiving (RX) antennas as shown in Figure 4.22.

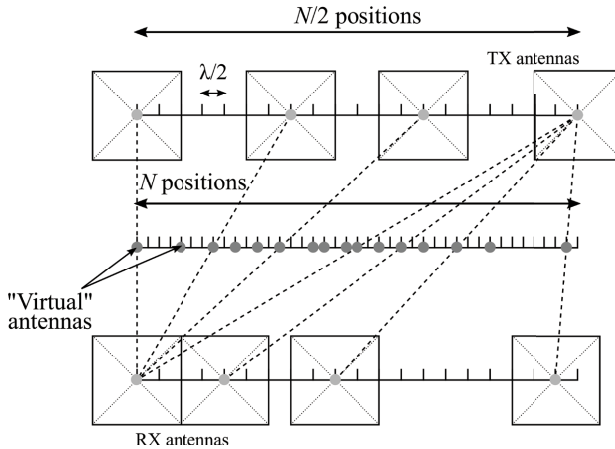


Figure 4.22: Sampling along the linear mechanical guide of a GBSAR.

When the TX antenna in the  $i$ -th position and the RX antenna the  $j$ -th position are both switched on (and all the others switched off), it is equivalent (in far field) to transmit and receive with one single “virtual” antenna along the median axis in the position  $(i+j)/2$ . Therefore for each combination of the TX and RX antennas a specific pattern along the median axis is defined. This pattern can be seen as a random sampling of the electromagnetic field backscattered by the targets in the field of view of the radar.

### Selection of optimal pattern

Generally speaking,  $N_{TX}$  antennas positioned along a guide with  $N/2$  possible positions and  $N_{RX}$  antennas positioned along another guide with  $N/2$  positions, give theoretically possible configurations  $(N/2)^{N_{TX}} \cdot (N/2)^{N_{RX}}$  (patterns).

Obviously many of these are repetitive and not practically feasible as it is not possible to put two antennas too close or in the same position. In order to select between them the patterns more suitable for the CS procedure we have established the following criteria:

1. the antennas must keep their order. It means that each antenna is numbered and antenna number  $n$  has to be always on the left of antenna  $n+1$ ;
2. as the antennas have a physical size, between two nearby antennas there must be at least  $\Delta p$  empty positions;
3. the number of “virtual” antennas along the median axis must be maximum, i.e.  $N_{TX} \times N_{RX}$ ;
4. equal patterns must be eliminated. For doing it any single pattern along the median axis is identified with a binary number of  $N$  digit. The true-value corresponds to one position occupied by one virtual antenna. The digit numbers are ordered and the double numbers discharged;
5. in order to exploit the whole synthetic aperture, the first and the last positions along the median axis must be occupied.

As an example we consider  $N_{TX} = N_{RX} = 4$ ,  $N = 40$ ,  $\Delta p = 4$ . The compression factor results in  $16/40 = 0.40$ . The patterns that respect the six conditions declared above are 132. Figure 4.23 shows these 132 patterns as they appear along the median axis of the MIMO. The “virtual” antennas occupy the yellow positions while the blue positions are empty.

All these patterns could work with CS techniques. Nevertheless, some simulations has been performed in order to select the best possible. The radar response of one single target at 50 m distance has been simulated.

The used parameters were: initial frequency  $f_1 = 9.84$  GHz, final frequency  $f_2 = 10.16$  GHz, number of frequencies  $N_f = 801$ . The obtained image (using the CS with Haar wavelets and OMP recovery method) has been compared with the image obtained sampling as required by Nyquist. The extremes of the image were from 25 m to 75 m in range and from  $-25^\circ$  to  $25^\circ$  in azimuth. The comparison has been performed estimating the Peak Signal Noise Ratio (PSNR) calculated as (4.5).



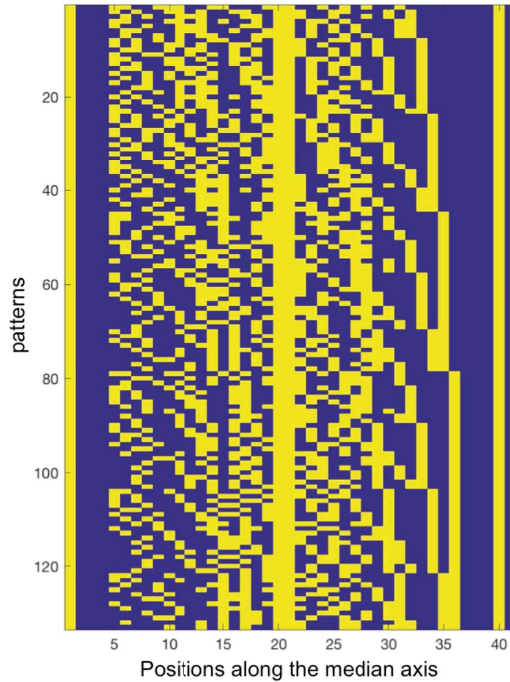


Figure 4.23: Possible patterns of “virtual antennas” along the median axis of MIMO [140].

The black plot in Figure 4.24 shows the PSNR for the 132 patterns as identified in Figure 4.23. All patterns give  $\text{PSNR} > 24$  dB and the maximum value is about 29.5 dB.

The performances of CS reconstruction depends on the specific image, generally they are better when the target is perfectly in front of the radar. In order to consider a more realistic scenario, the simulation has been repeated by shifting the target from  $x = -6$  m to  $x = 6$  m at 2 m step. The coloured plots in Figure 4.24 shows the PSNR for these targets.

For selecting the best pattern a relative threshold has been selected. The threshold was lower than 1, but close to 1. The patterns with PSNR higher than its highest value, multiplied the relative threshold, has been identified for each plot. After that, only the pattern that are over the threshold for all the plots has been selected. Finally the threshold was raised until obtain a single pattern. With reference to Figure 4.23 the selected pattern is the number 15.

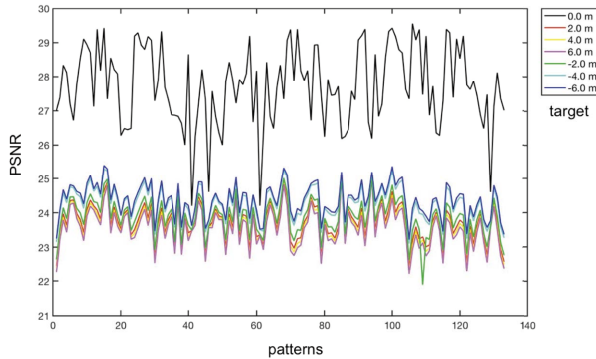


Figure 4.24: Simulated PSNR for different patterns and different target positions [140].

### Radar prototype

Figure 4.25(a) shows the block scheme of the radar prototype. The vector network analyser (HP8720D) operates as transceiver.

The switching system consists of eight single-pole double-through (SPDT) mod. MSP2T-18-12+ and ten high phase stability ( $\pm 0.5^\circ$ ) microwave cables (SUCOFLEX 126). Another couple of SPDT provides a calibration path (with a -40 dB power attenuator).

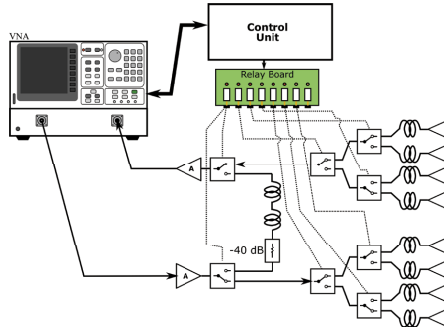
A relay board controls the switching system. The calibration path and all the paths between VNA and each antennas are of the same electromagnetic length in order to avoid any further calibration procedure. Figure 4.25(b) shows a photograph of the radar head.

The MIMO radar has been preliminary tested in a controlled experimental test site. In an open garden, a single corner reflector (CR) of 0.4 m side length was positioned at 13.4 m in front of the radar.

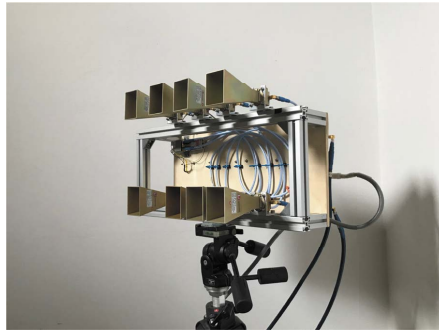
The measurement parameters were:  $f_1 = 9.84$  GHz,  $f_2 = 10.16$  GHz, and  $N_f = 801$ . Figure 4.26 shows the obtained radar image.

The red line in Figure 4.27(a) is the Point Spread Function (PSF) in azimuth at the distance of the CR. The blue line is the PSF obtained by simulating one point scatterer in front of the radar. The agreement between the two plots is very good.

As the CS performance depends critically on the view angle, we repeated the measurement moving the CR 2.80 m on the right. Figure 4.27(b) shows the measured and simulated power plots. Note that the angle  $\varphi$  is between the x-axis and the view direction, so  $90^\circ$  is in front of the radar and  $\varphi < 90^\circ$  is on the right side.



(a) Block scheme of the radar prototype.



(b) Photograph of the radar head.

Figure 4.25: Block scheme and photograph of the radar head.

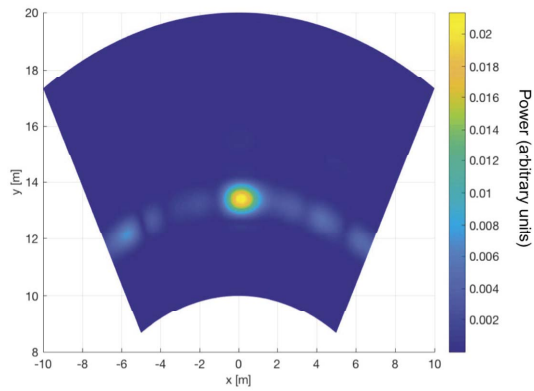


Figure 4.26: Radar image of a CR in front of the radar [30].

It is interesting to note that the simulated and measured plots have a small misalignment that cannot be easily corrected. Indeed, it is an effect

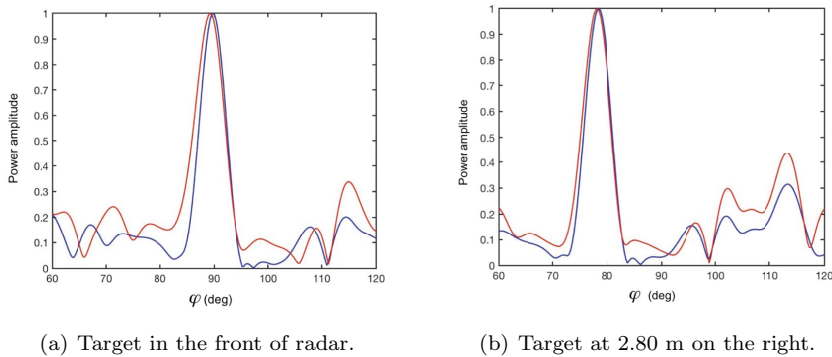


Figure 4.27: Experimental (red line) and simulated (blue line) PSF in azimuth of a CR in front of the radar [30].

of the non-linearity of the CS recovery.

In order to verify this statement, a simulation has been performed: a single target at 13.4 m distance with  $\varphi_0$  azimuth angle varying from  $80^\circ$  to  $100^\circ$  at step of  $0.5^\circ$ . The error  $\delta\varphi_0$  in the azimuth recovered using the CS has the non-linear behaviour shown in Figure 4.28.

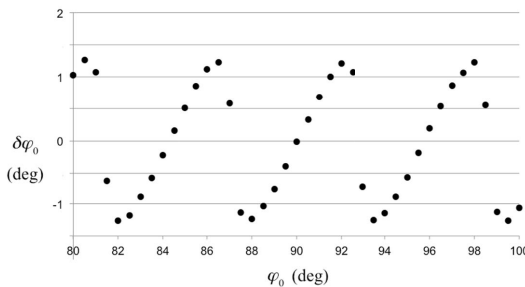


Figure 4.28: Error in the azimuth angle estimation by varying the azimuth angle [30].

A critical issue of any radar is the amplitude of the sidelobes. For a CS radar, this value could be rather erratic.

With the aim of evaluate it, the response of a single target at 13.4 m distance at  $\phi_0$  azimuth was simulated. The plot in Figure 4.29 shows the peak to sidelobe ratio (P/SL) in function of  $\phi_0$ .

Only the sidelobes inside the antenna lobe ( $\pm 20^\circ$ ) have been evaluated. It results that if the target is inside a view cone  $\pm 15^\circ$  the P/SL is always larger than 10 dB.

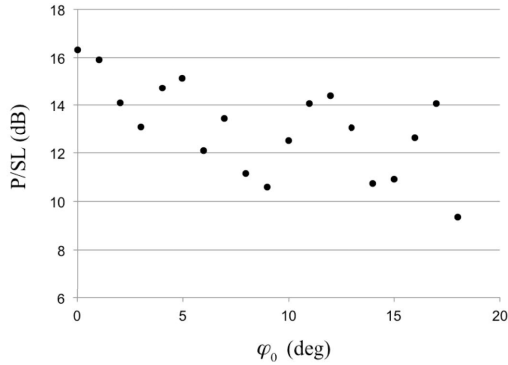


Figure 4.29: P/SL for a single target at 13.4 m distance at the azimuth angle between  $0^\circ$  and  $18^\circ$  at  $1^\circ$  step [30].

In order to test the capability of MIMO to detect displacement by interferometry, the CR was located on a micropositioner with 0.1 mm nominal accuracy. The CR was moved forward the radar at step of 5 mm.

Figure 4.30 shows the obtained results. The agreement with nominal values is better than 0.2 mm.

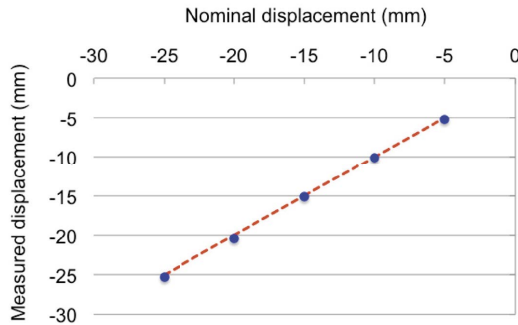


Figure 4.30: CR displacements detected by radar [30].

### In-field tests

The radar prototype has been in-field operated for monitoring a pedestrian bridge in Poggibonsi, Italy and Vespucci bridge in Florence, Italy. In the second case the results of radar prototype has been compared with a real-aperture radar in  $K_U$  bandwidth.

### Pedestrian bridge

The pedestrian bridge is located in Poggibonsi, Italy. The main span is 47.5 m long (Figure 4.31) and it is built with similar block of 2.5 m long and 2.8 m wide. In 2007, this bridge was tested with an interferometric radar. The experimental results were published in [111] and [141].

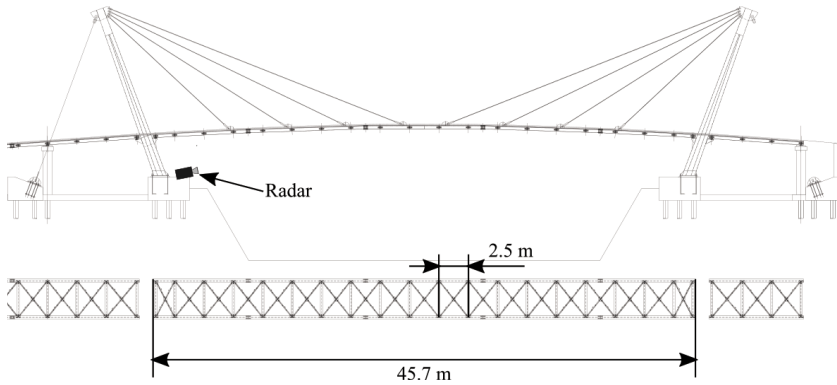


Figure 4.31: Pedestrian bridge of Poggibonsi, Italy.

The MIMO radar was installed close to one of the two pillars of bridge, as shown in Figure 4.31 and Figure 4.32. The measurement parameters were: initial frequency  $f_1 = 9.84$  GHz, final frequency  $f_2 = 10.16$  GHz, number of frequencies  $N_f = 801$ . Therefore, the range resolution was 0.47 m and the unambiguous range 375 m. The antenna aperture in the horizontal plan was about  $\pm 20^\circ$ . The transmitted power was 12 dBm. The radar completed a single acquisition in 31.4 s.



Figure 4.32: Photograph of the radar installation.

Figure 4.33 shows the obtained power image of the lower deck. The first nine transversal beams are well visible. The shape of the deck is recognizable. Unfortunately, due to the low transmitted power (12 dBm), the transversal beams are hardly visible in the portion of the deck farther than 24 m.

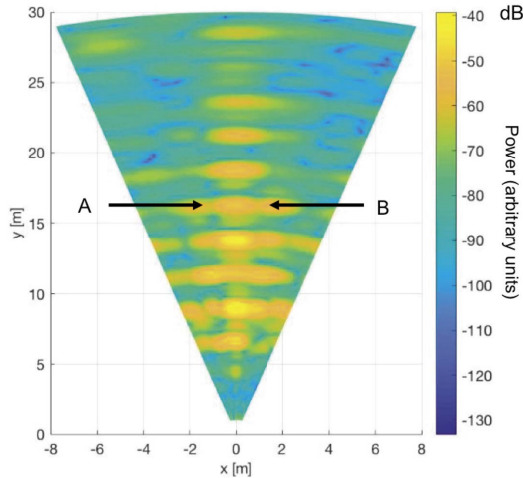


Figure 4.33: Radar image of the lower deck of the bridge [30].

The bridge was loaded with a small car (900 kg). It slowly went to the median point and came back. In order to evidence the effects of an asymmetric load the car was driven as on the left as it was possible (the bridge is wide 2.8 m, while the car was 2.6 m wide) as shown in Figure 4.34.



Figure 4.34: Test of the bridge using a small car as load.

Figure 4.35 shows the detected displacements (projected in vertical direction) of the points A (on the left side of the deck) and B (on the right side

of the deck) during the loading and downloading operations. In the x-axis, there is the number of acquisition (the radar acquired an image each 31.4 s) Both the points are at 16.18 m range, very close to the center of the span.

The car was slowly driven until to the center of span and it stayed there for about 12 min. As expected the point on the left had a larger displacement (about 2.0 mm). The difference of displacement between left and right sides is about 1 mm.

We note at the beginning of measurement session a slight uplift of the deck. In effect, as the pillars were about 10 m inside the riverbed (see Figure 4.31), when the car entered the bridge from one side the center of the span rose. Furthermore, the car passed the center and came back, so the plot in time shows two peaks (at 21st and 33rd measurements).

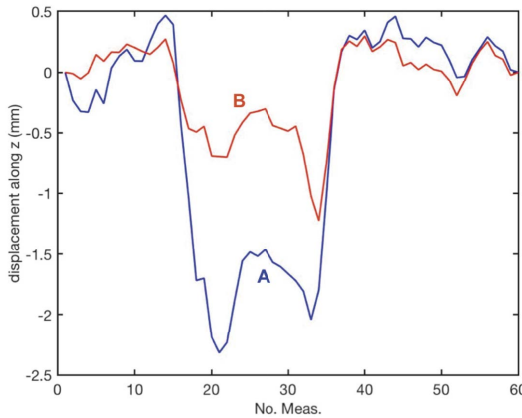


Figure 4.35: Plots of the displacements of points A and B [30].

### Vespucci bridge - Comparison with a real-aperture radar

The new Vespucci Bridge in Florence, Italy was inaugurated in 1957. It was not the reconstruction of the bridge destroyed by German mines during the WWII, but an original and innovative structure. Sixty years after its construction, the municipality commissioned an extensive monitoring campaign and possible restoration works.

An interferometric real aperture (RA) radar has been used for testing and calibrate some sensors for a long-term monitoring. This case study has been exploited even for testing the interferometric MIMO radar.

During the monitoring campaign of the Vespucci bridge the  $K_U$ -band RA (Ku-Ra) and the X-band MIMO (X-MIMO) radar have been positioned on the river bank close to a pillar (see map in Figure 4.36 and picture in



Figure 4.36). A Corner reflector (CR) has been installed on the lower deck (see pictures in Figure 4.36 and Figure 4.37(b)).

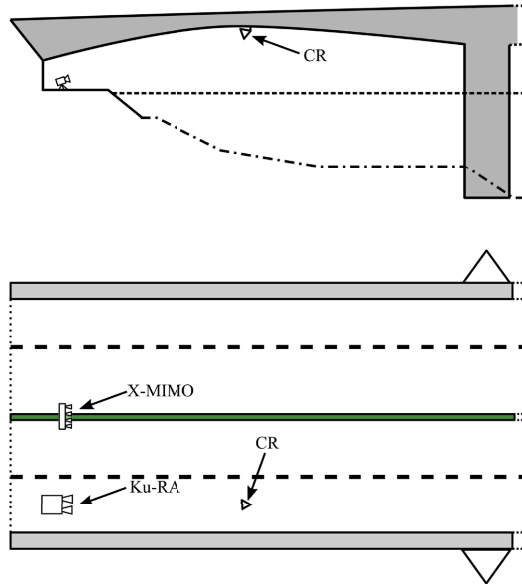
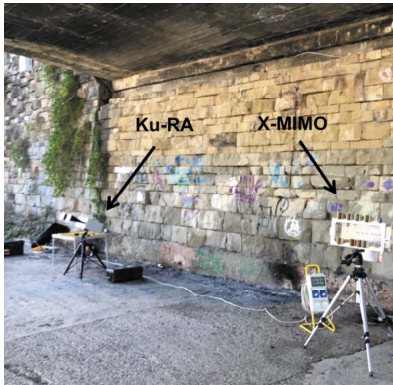
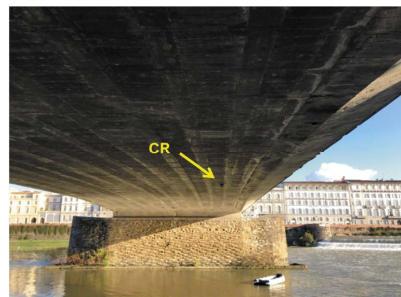


Figure 4.36: Map of the radar installation.



(a) Picture of the two radars.

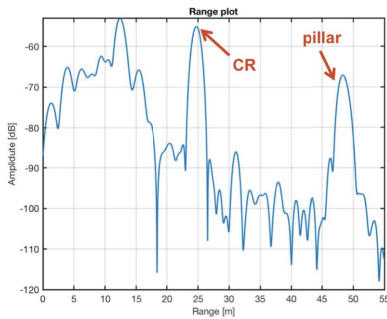


(b) Picture of the view from the radars.

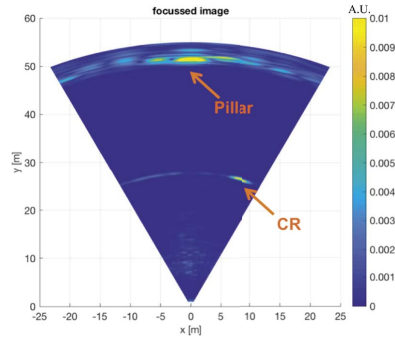
Figure 4.37: Radar setup.

Figure 4.38(a) shows the amplitude plot of the radar signal acquired by Ku-RA radar. The peak at about 25 m is the Corner reflector. The signal of the pillar in front of the radar is at about 47 m.

Figure 4.38(b) shows the image acquired by X-MIMO radar. The 2D imaging capability is demonstrated. The position of CR in the plan is correctly detected.



(a) Amplitude plot acquired by Ku-RA radar [128].



(b) Radar image acquired by X-MIMO radar [128].

Figure 4.38: Radar images.

The main scope of this experimental test was to compare the displacement of CR detected by Ku-RA radar and X-MIMO radar. The sampling time of Ku-RA radar was 4.1 ms, while the sampling time of X-MIMO radar was about 30 s.

Figure 4.39(a) shows the two plots in the same graph during the load operation of the bridge. Figure 4.39(b) shows the two plots during another measurement session, when the Ku-RA radar was operative only in the last 600 s. The agreement is rather good.

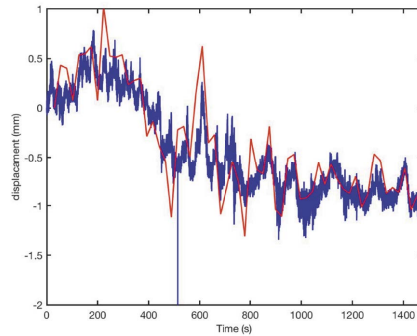
#### 4.4 Conclusions

An interferometric compressive sensing MIMO has been designed and successfully tested as geotechnical equipment for testing bridges.

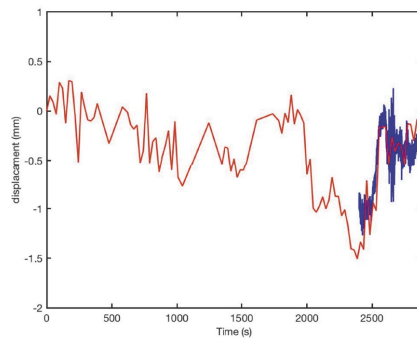
The radar has been tested in controlled environment and the experimental results have been compared with the simulations. This test was performed by using a corner reflector on a micro-metric positioner stage.

In-field test has been performed during a static test of a pedestrian bridge in Poggibonsi, Siena, Italy. The static load was located on the left side of the bridge and the radar was able to resolve different displacements of targets at the same range.

The measurements exploited with the CS MIMO were also compared with a conventional real-aperture radar during the static test of Vespucci



(a) Comparison between Ku-RA and X-MIMO radar [128]. Load operation.



(b) Comparison between Ku-RA and X-MIMO radar [128].

Figure 4.39: Displacement of CR detected by RA radar (blue) and by MIMO radar (red) [128]

bridge in Florence, Italy. The agreement between the results of two systems was good.

The sampling time of the radar prototype is about 30 s, but this relatively long time is due to the specific VNA that operated as transceiver. It was an old model (HP8720D) not designed for fast operation. In effect, as this radar does not have mechanical moving parts, it could acquire much faster than the current GB synthetic aperture radar (SAR) based on the movement of a radar head along a mechanical linear guide.

A fast interferometric radar can have single-tone integration time of  $10 \mu\text{s}$  with the number of frequency  $N_f = 500$ . It means an acquisition time of 20 ms using four antennas. A radar with 2-D imaging capability (provided by

the MIMO architecture) operating at this acquisition speed (50 Hz) opens exciting perspectives in the field of health monitoring and testing of large structure.

For the sake of simplicity, the radar is provided with eight antennas. This configuration can give high side clutter with targets at more than  $10^\circ$ - $20^\circ$  with respect to direction of view. Nevertheless, a MIMO based on the same working principle could be used for monitoring targets with larger angular extension (like building or slopes) by increasing the number of antenna. Probably a CS MIMO with  $8 \times 8$  antennas could cover the majority of applications.

# Advanced in 3 dimensional GBSAR

The current equipment exploits the movement of a radar head along a linear mechanical guide for synthesizing a large aperture [142]. Since the movement is along a single axis the obtained radar image does not have angular resolution in the plane orthogonal to the scan axis. In other words, if the radar head scans along the x-axis the radar image cannot have resolution in elevation angle. Figure 5.1 shows an example of resolution cell of the traditional systems.

This is not a serious problem when the scenario is a slope, where the altitude (z-axis) can be reasonably considered an unambiguous function of the (x,y) position. Unfortunately there are cases where the geometry of the structure under test is much more complex [39], [79].

A trivial solution is to scan the radar head along the x-z plane (or on a spherical shell [143]). In this way it is possible to obtain a 3D image of the targets in the field of view.

The problem is the measurement time can be very long. As an example, a fast GBSAR able to scan a line of 100 points in 5 minutes [87], will scan a plane of 100 lines in more than 8 hours. It means that the radar is able to detect only very slow movements.

In this Chapter two radars able to provide a 3 dimensional image are

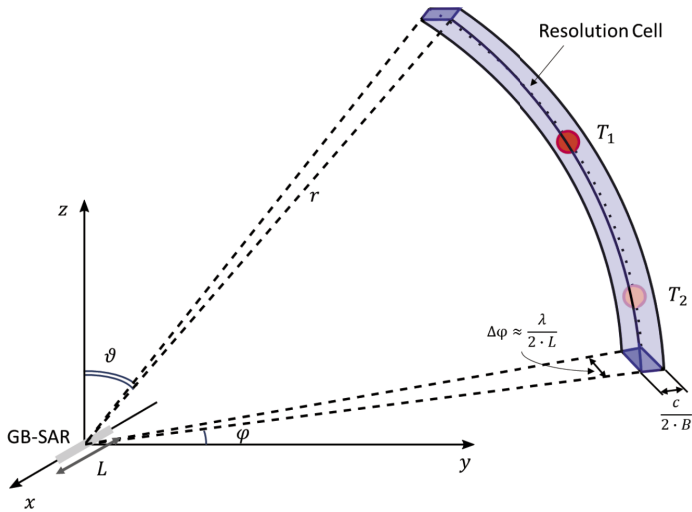


Figure 5.1: Resolution cell of traditional GBSAR systems.

proposed. These radars are based on the technology proposed in the previous Chapters: the first uses the bistatic technique [144], [145]; the second model uses the CS method [146]. Recently, some other solutions for 3D imaging are presented for example [88] and [147].

### 5.1 GBSAR with 3D bistatic imaging capability

A practical solution to achieve a 3D image could be a radar system able to acquire fast images without resolution in elevation and slow images with both azimuth and elevation resolution. The GBSAR presented in this section is a special bistatic GBSAR configuration that has this capability.

The radar head moving along x-axis has a second transmitting channel linked to a third antenna through a RF cable. This third antenna is moving along a mechanical vertical axis. For each horizontal scan the radar system acquires a monostatic image of its field of view without elevation resolution. When the radar system completes the whole acquisition (along both x-axis and z-axis), it obtains a 3D image of its field of view.

The sketch of the bistatic GBSAR system proposed is shown in Figure 5.2. A linear monostatic GBSAR is moving along a horizontal rail (along x-axis) by acquiring interferometric 2-D images. The radar head has a second transmitting channel for operating in bistatic modality. By using this channel, the radar transmits to a supplementary antenna that moves vertically along a mechanical axis.

The vertical axis is positioned at distance  $y_0$  behind the horizontal axis in correspondence of its central point. The lower position of the antenna vertically moving is at  $z_0$  over the x-axis. The radar head and the supplementary antenna are linked through a RF cable of length  $L_0$ . In this bistatic configuration the radar system is able to acquire data with spatial diversity in both direction (x and z) so it is able to obtain a 3D image of the targets in its field of view.

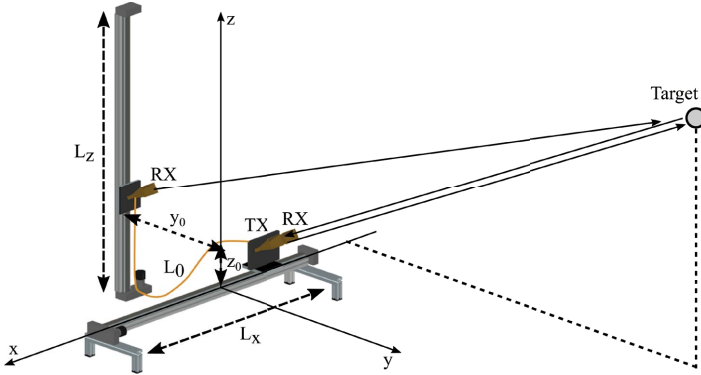


Figure 5.2: Working principle of the monostatic/bistatic GBSAR.

The images can be focused in the 3D space in front of the radar, by taking into account of the path radar head - supplementary antenna - image point. The algorithm used is a modified version of the back-propagation algorithm described in (2.18).

The advantage of this configuration with respect to other solutions [143], [148] is that for each horizontal scan the radar equipment is able to provide a monostatic image that can be used for detecting fast displacements. The complete 3D image is obtained only at the end of the vertical scan.

Monostatic and bistatic images have different angular resolutions. As it is known, the azimuth resolution ( $\Delta\varphi_m$ ) of a monostatic GBSAR image is given by (2.14)

$$\Delta\varphi_m \simeq \frac{\lambda}{2L_x} \quad (5.1)$$

with  $L_x$  the horizontal span.

With the aim to estimate the bistatic angular resolution, we have to take into account that transmitting from a point A and receiving from a point B is equivalent to transmit and receive from the median point C. With reference to Figure 5.3, the locus of median points is the dotted rectangle.

Therefore, the bistatic images have angular resolution in azimuth ( $\Delta\varphi_b$ )

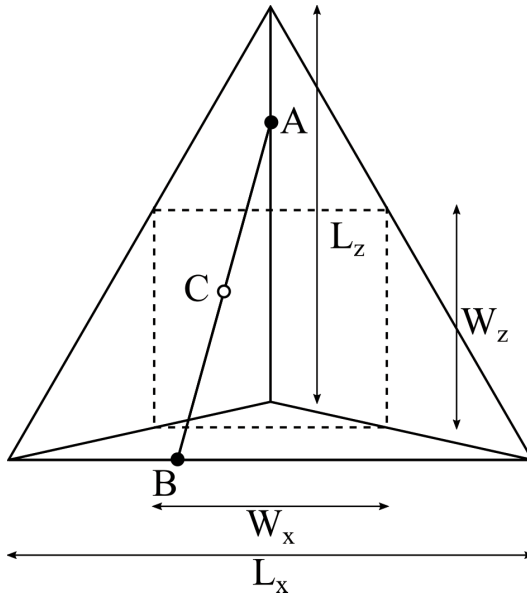


Figure 5.3: Bistatic geometry.

and elevation ( $\Delta\vartheta_b$ ) given by

$$\Delta\varphi_b \simeq \frac{\lambda}{2W_x} \quad \Delta\vartheta_b \simeq \frac{\lambda}{2W_z} \tag{5.2}$$

with  $W_x$  and  $W_z$  the two sides of the dotted rectangle in Figure 5.3. If the lower position of the supplementary antenna is close to the horizontal scan,  $W_z \simeq L_z/2$ . Therefore

$$\Delta\varphi_b \simeq \frac{\lambda}{L_x} \quad \Delta\vartheta_b \simeq \frac{\lambda}{L_z} \tag{5.3}$$

In other words, the azimuth resolution of the bistatic images is a factor 2 worse than monostatic images.

### Radar prototype

The GBSAR prototype we have assembled for testing the proposed working principle is shown in Figure 5.4.

The vector network analyzer (VNA) HP8720D operated as transceiver providing a continuous wave stepped frequency signal (CWSF) in X-band with central frequency  $f_c = 10$  GHz and bandwidth B. Two RF cables linked the VNA to the front-end moving along the horizontal mechanical axis. Two single-pole double-throw (SPDT) switches provided a direct path between



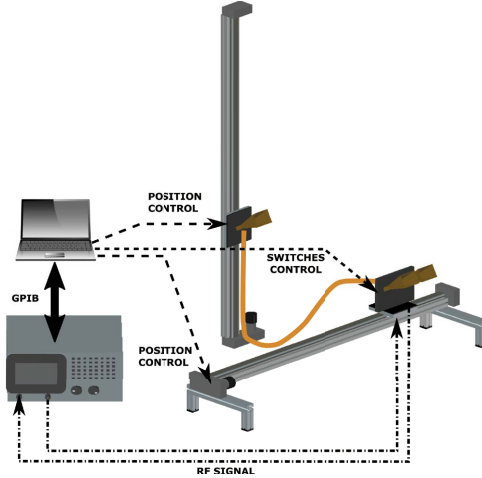


Figure 5.4: Sketch the GBSAR prototype.

the transmitter and the receiver in order to perform calibrated measurements. A third SPDT switched between the two TX antennas.

For each single step along the horizontal mechanical rail the radar carries out the two acquisitions (monostatic and bistatic). A monostatic acquisition is complete after  $N_x$  steps when the radar head has swept the horizontal axis, while the bistatic acquisition is complete only after  $N_z$  horizontal scans, i.e. after  $N_x \times N_z$  steps. The two mechanical axes spanned up to 1.50 m along x and up to 1.50 m along z.

## Experimental test

### Controlled environment

In order to test the radar equipment in a controlled environment, the sensor has been installed on a garden. The map of the test field is shown in Figure 5.5.

A corner reflector (CR) of 0.4 m side was positioned on the tip of 3.0 m high wood pole. The pole was in front of the radar at 17.1 m distance. A second CR of 0.27 m side was positioned on a tripod (height from ground: 1.2 m) on the right side of the radar. This CR could be moved along the view direction using a mechanical device with 0.1 mm nominal accuracy.

The radar parameters are:  $f_c = 10$  GHz,  $B = 160$  MHz,  $L_x = 1.5$  m,  $L_z = 1.02$  m,  $N_x = 150$ ,  $N_z = 102$ ,  $y_0 = 0.63$  m,  $z_0 = 0.19$  m,  $L_0 = 4.00$  m.

Figure 5.6 shows one of many monostatic images that have been obtained during the complete 3D bistatic acquisition. The acquisition time of each

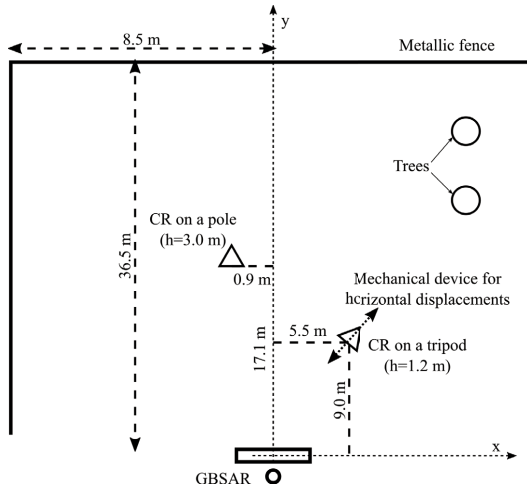


Figure 5.5: Map of the test field.

single monostatic image was 25 minutes, the complete 3D bistatic acquisition lasted about 42 hours. In the monostatic image are evident both the CR on the pole and the CR on the tripod, but obviously it is not possible to obtain their heights.

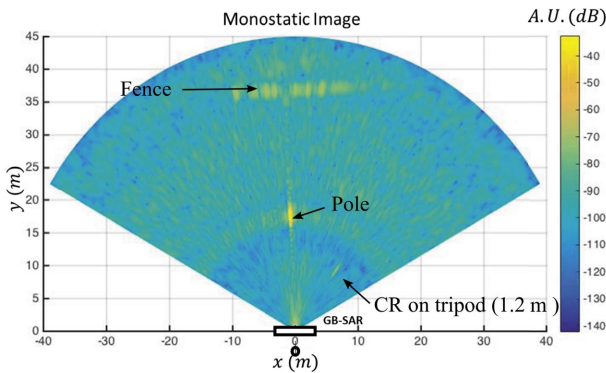


Figure 5.6: Monostatic radar image.

During the bistatic acquisition the CR on the tripod was moved along the view direction using a micrometric positioner with 0.1 mm accuracy. Figure 5.7 shows the measured and the nominal displacement of the CR during the 102 acquisitions. The mean error was 0.13 mm.

Finally, when the whole 3D bistatic acquisition was completed, it has been possible to focus in any arbitrary plane of the space in front of the

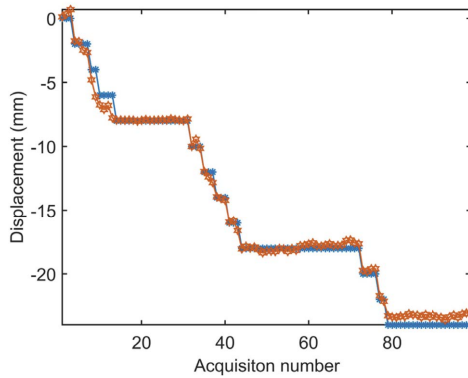


Figure 5.7: Measured (blue line with spots) and nominal displacement (red full line) of the CR on the tripod.

radar.

Figure 5.8 shows the bistatic image focused in the horizontal plane  $z = 1.0$  m, while Figure 5.9 shows the bistatic image focused in the horizontal plane  $z = 3.0$  m. It is interesting to note that in the lower plane ( $z = 1.0$  m) it is possible to see the CR on the tripod, the pole and the metallic fence, while in the upper plane ( $z = 3.0$  m) plane only the CR on the tip of the pole is well visible, the CR on the tripod is not visible and the metallic fence gives only a light residual.

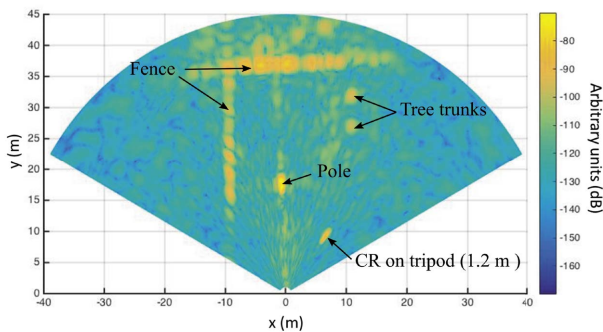


Figure 5.8: Bistatic radar image focused in the horizontal plane  $z = 1.0$  m.

Figure 5.10 shows the azimuth Point Spread Function of the corner reflector on the tripod focused in the same plane both for monostatic and bistatic. It is possible to note that the resolution of bistatic is twice worst

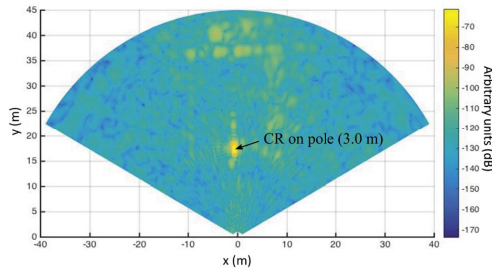


Figure 5.9: Bistatic radar image focused in the horizontal plane  $z = 3.0$  m.

than monostatic.

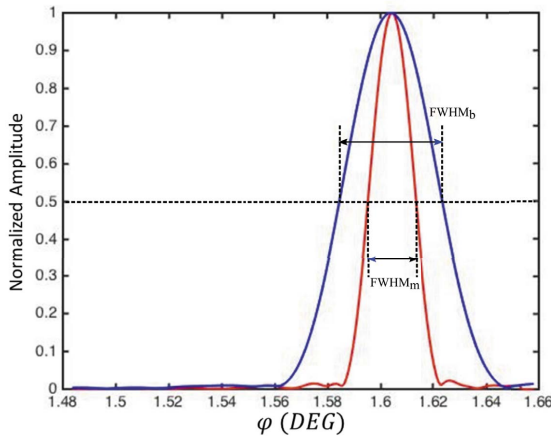


Figure 5.10: Azimuth Point Spread Function of monostatic (red) and bistatic (blue) image.

Figure 5.11 shows the bistatic image focused in the vertical plane at  $x = -1$  m. It is evident the radar fence and the CR on the tip of the pole at 3.00 m height.

Realistic scenario

With the aim of testing the equipment in a more realistic scenario, we pointed the radar forward a 7-storey building at about 140 m distance.

The radar parameters we have set are central frequency 10 GHz,  $B = 80$  MHz,  $L_x = 1.5$  m,  $L_z = 1.5$  m,  $N_x = 150$ ,  $N_z = 150$ ,  $y_0 = 0.62$  m,  $z_0 = 0.21$  m,  $L_0 = 4.00$  m.

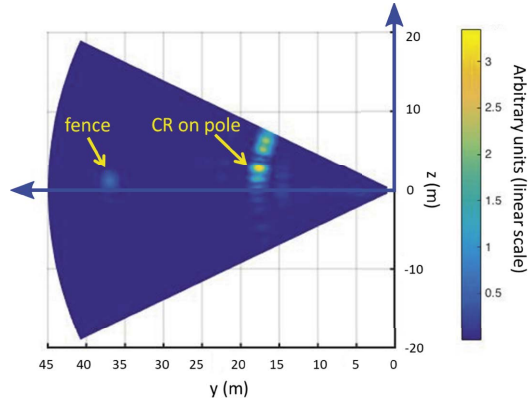


Figure 5.11: Bistatic radar image focused in the vertical plane  $x = -1.0$  m.

The obtained monostatic image is shown in Figure 5.12. The façade of the building is a clear oblique line. Obviously the monostatic (bi-dimensional) image cannot provide information about the height.

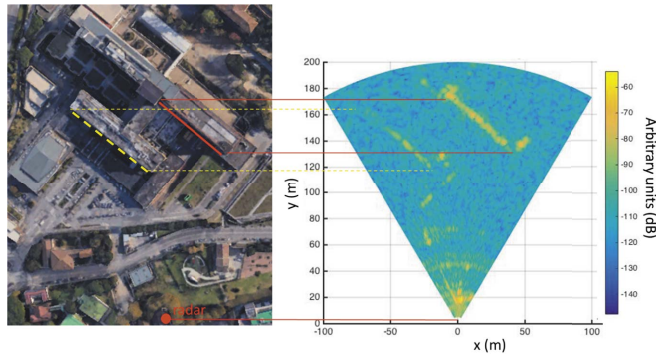


Figure 5.12: Monostatic image of the 7-storey building.

Figure 5.13 shows the obtained radar image focus in a horizontal plane  $z = 10.0$  m. Also in this image the façade are well visible as oblique line. Anyway, we can note that the resolution and the signal over noise are worst than Figure 5.12

Bistatic radar image focused on the façade plane is shown in Figure 5.14. In this image the edges and the roof of the building are detectable.

Finally, Figure 5.15 shows the radar image focused in the whole three-dimensional space in front of the radar. In order to remove the noise a threshold in amplitude equal to 1.7% of the maximum value was applied.

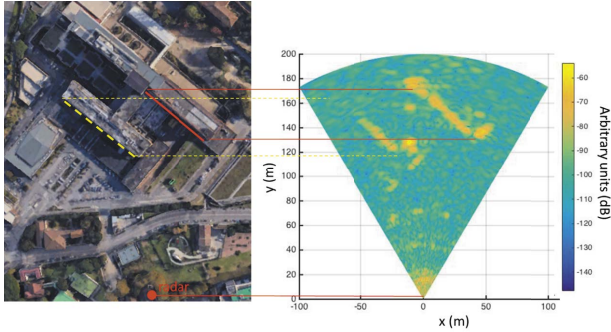


Figure 5.13: Bistatic radar image of the 7-storey building focused in the horizontal plane  $z= 10.0$  m.

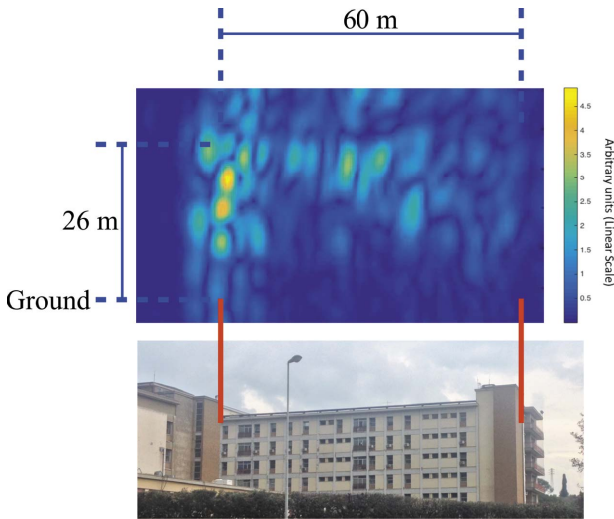


Figure 5.14: Bistatic radar image focused on the façade plane of the 7-storey building.

The façade of the building is an evident target in the 3D space.

## 5.2 GBSAR with 3D imaging capability using compressive sensing MIMO in elevation

An other solution, for obtaining resolution in elevation, is to combine a multiple output multiple input (MIMO) radar [149] head able to provide vertical resolution with a horizontal scan. Indeed, this idea is inspired to

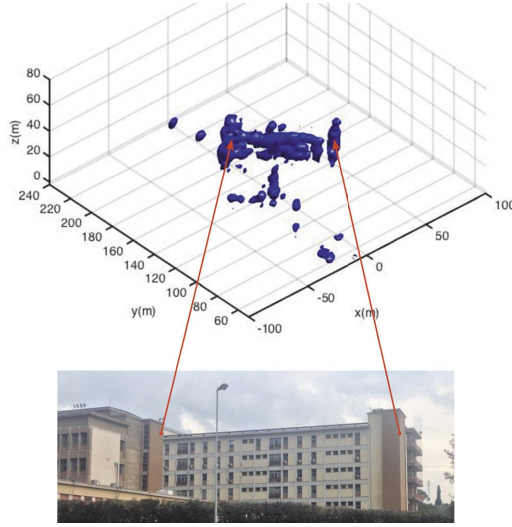


Figure 5.15: Bistatic 3D image.

Synthetic Aperture Radar (SAR) tomography spaceborne [150] or airborne [151] that combine different passages for obtaining information in the third dimension.

This hybrid approach has been tested in the same realistic measurement scenario of the preview system: a 7-storey building at about 140 m distance.

### Radar prototype

The sketch of the radar system is shown in Figure 5.16. A step-frequency continuous wave (SFCW) transceiver transmits  $N_f$  frequencies from  $f_1$  to  $f_2$  at step  $\Delta f$ . The radar head is moving along a horizontal rail (the x-axis).

The radar front-end was the same used in Chapter 4 for the interferometric CS MIMO. The pattern was the same of Chapter 4, though for this application the antennas were installed in vertical direction as shown in Figure 5.17.

In this case the angular resolution ( $\Delta\varphi$ ) in the horizontal plane (azimuth) is obtained by mechanical scanning, while angular resolution ( $\Delta\vartheta$ ) in vertical axis (elevation) is obtained through the vertical disposition of the CS-MIMO. In both cases the angular resolution depends on the synthetic aperture:

$$\Delta\varphi \simeq \frac{\lambda}{2L_x} \quad (5.4)$$

$$\Delta\vartheta \simeq \frac{2}{N} \quad (5.5)$$

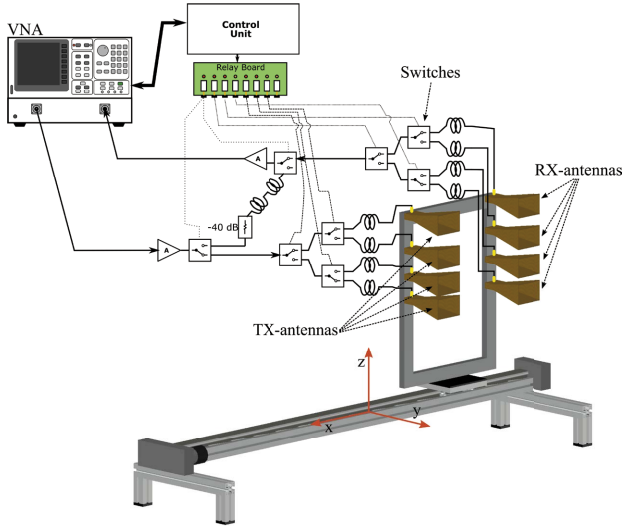


Figure 5.16: Sketch of the radar system.

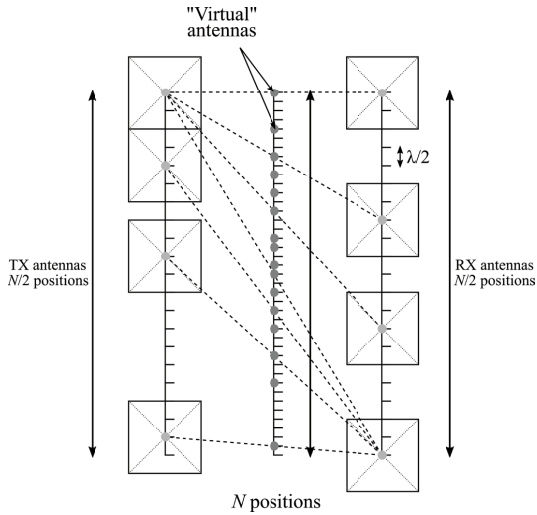


Figure 5.17: Configuration of antennas in MIMO radar head .

For the radar system tested,  $L_x=1.80$  m,  $\lambda=30$  mm,  $N=40$ , so  $\Delta\varphi = 0.45^\circ$  and  $\Delta\theta = 2.86^\circ$ .



### Experimental test in a real measurement scenario

The vector network analyzer (VNA) HP8720D operated as transceiver providing a continuous wave stepped frequency signal (CWSF) in X-band. The radar parameters were: central frequency  $f_c = 10$  GHz, bandwidth  $B = 310$  MHz, number of frequencies  $N_f = 801$ , length of the horizontal scan  $L_x = 1.8$  m, number of acquisition points along the x-scan  $N_x = 180$ , transmitted power  $P = 26$  dBm, gain of antennas  $G = 15$  dB, time of integration of each single tone  $\tau = 0.33$  ms. The integration time was  $t_{int} = \tau \times 16 \times N_f \times N_x = 769$  s.

In order to test the radar equipment in a controlled environment, the radar has been installed on a garden of the University (see Figure 5.18). The aerial picture of the test field is shown in Figure 5.19.



Figure 5.18: Picture of the equipment.

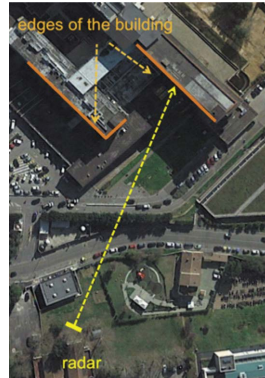


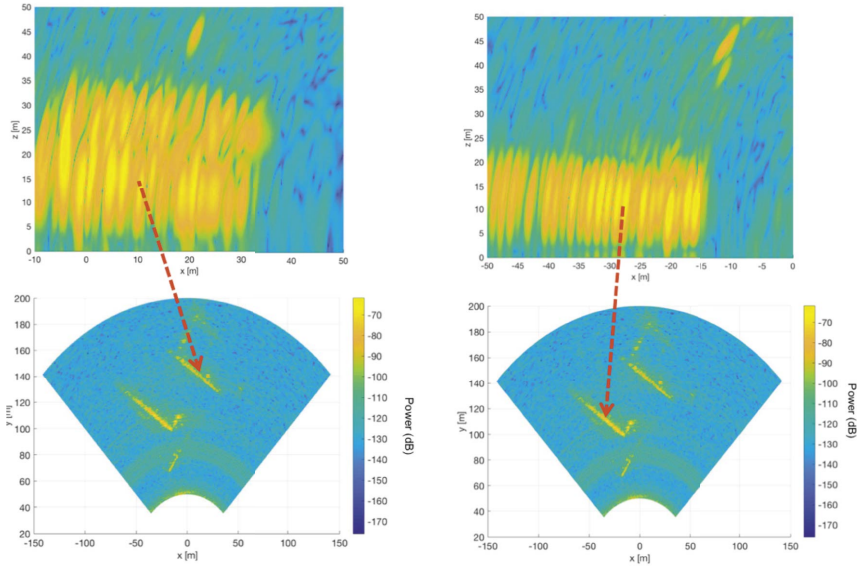
Figure 5.19: Aerial picture of the test site [146].

After a complete acquisition the measurement matrix  $E_{k,l,m}$  can be focused in the space in front of the radar.

Figure 5.20(a) shows the obtained radar image focused on the horizontal plane at 10 m height and the radar image focused on a vertical plane

approximately on the façade of the farthest building (at about 140 m).

The upper image in Figure 5.20(b) shows the radar image focused on a vertical plane approximately on the façade of the other building (at about 100 m).



(a) Below: radar image focused on the horizontal plane at 10 m height. Above: radar image focused on a vertical plane approximately on the façade of the farthest building (at about 140 m) [146].

(b) Below: radar image focused on the horizontal plane at 10 m height. Above: radar image focused on a vertical plane approximately on the façade of the closest building (at about 100 m) [146].

Figure 5.20: Radar images focused on the horizontal plane at 10 m height and radar images focused on a vertical plane approximately on the façade of the building.

Finally, Figure 5.21 shows the 3D contour plot of the iso-surface using a suitable power threshold. The shape of the two buildings are clearly recognizable.

### 5.3 Conclusions

In this chapter two GBSAR prototypes with 3D imaging capability were proposed.

The first GBSAR used the bistatic principle in order to obtain the elevation resolution. This monostatic/bistatic GBSAR system has been demonstrated able to produce 2D images in short times (about a half hour) and 3D

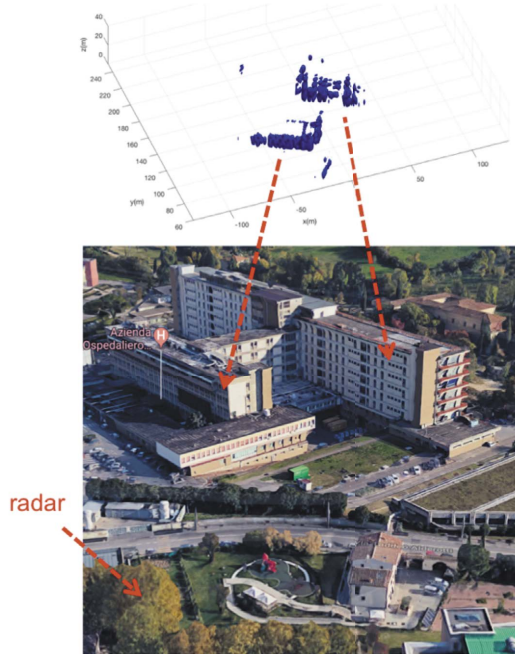


Figure 5.21: The 3D contour plot of the power iso-surface with a suitable threshold [146].

images in long times (several hours). It is worth to note that this radar configuration has been obtained as an upgrade of a linear monostatic GBSAR. The bistatic 3D system shares the radar head and the horizontal mechanical axis with the 2D linear monostatic GBSAR. To improve the images resolution the central frequency can be increased (the prototype operated in X band, but the majority of GBSAR operates in  $K_U$  band). It is possible also to increasing the height of the vertical axis twice. In practice, a GBSAR operating at 17 GHz with a 3 m vertical axis has vertical resolution four times better to the equipment presented in this thesis, and this can make the difference in many applications.

The second GBSAR system used an hybrid working principle: synthetic aperture for azimuth resolution, and compressive sensing MIMO for elevation resolution. Also this system is able to provide a 3D image and the azimuth resolution can be improved by increasing the bandwidth and the scan length. On the contrary of azimuth resolution, elevation resolution does not depend on central frequency, but on the number of antennas used as shown in (5.5).



# Conclusions

The research activity, presented in this thesis, concerns design and development of some advanced Ground Based Radar Interferometric systems. These systems are related to the following issue: detection of displacement vector, Multiple Input Multiple Output (MIMO) and radars with 3D capability.

The basic principle of this radar systems has been presented. All systems proposed have been successfully tested in controlled and real environment and, wherever possible, their performance have been compared with conventional systems.

## Radar systems for retrieving the displacement vector

A GBSAR operating in monostatic and bistatic modality was presented. The sensor detects the first component of displacement as the conventional GBRI (monostatic) and an additional component through a transponder (bistatic).

The radar has been tested with a basic transponder (two antennas and an amplifier) in a controlled environment and it was able to detect two components of displacement. The gain of the basic transponder was about 50 dB. In this case the measurements were affected by some artefacts due to the signal leaked from transponder during the monostatic measurements.

In order to improve the SNR of the bistatic measurements two enhanced transponders, with an high gain, were presented.

The first transponder made use of a frequency shifter in order to insulate the two antennas and achieved a gain of 91 dB. The artefacts did not affect the measurement with this transponder, but its implementation is rather difficult in practical cases.

The other is a long cable transponder with a gain of 82 dB. This transponder appears to be more practical for most of the uses.

Other application of bistatic technique was presented. A notable application is the monitoring of slender structures. In this application it was possible to measure the natural axis of a telecommunication tower for the first time with a GBRI.

The issue of retrieving displacement vector is still open. Indeed the GBRI presented in this thesis is able to detect only two components, the next step will be to generalize this theory in order to retrieve the whole displacement vector.

## Compressive Sensing MIMO Radar

An interferometric compressive sensing MIMO has been designed and successfully tested as geotechnical equipment for bridges. The radar has been tested in controlled environment and the experimental results have been compared with the simulations.

In-field test has been performed during a static test of bridge. The radar was able to resolve displacements of targets at the same range.

The measurements exploited with the CS MIMO were also compared with a conventional real-aperture radar and the agreement was good.

The sampling time of the radar prototype is about 30 s, but this relatively long time is due to the specific VNA that operated as transceiver. It was an old model (HP8720D) not designed for fast operation. In effect, as this radar does not have mechanical moving parts, it could acquire much faster than the current GB synthetic aperture radar (SAR) based on the movement of a radar head along a mechanical linear guide.

A fast interferometric radar can have single-tone integration time of 10  $\mu$ s with the number of frequency  $N_f = 500$ . It means an acquisition time of 20 ms using four antennas. A radar with 2-D imaging capability (provided by the MIMO architecture) operating at this acquisition speed (50 Hz) opens exciting perspectives in the field of health monitoring and testing of large structure.

For the sake of simplicity, the radar is provided with eight antennas. This configuration can give high side clutter with targets at more than  $10^\circ - 20^\circ$

with respect to direction of view. Nevertheless, a MIMO based on the same working principle could be used for monitoring targets with larger angular extension (like building or slopes) by increasing the number of antenna. Probably a CS MIMO with  $8 \times 8$  antennas could cover the majority of applications.

## Advanced in 3 dimensional GBSAR

Two GBSAR prototypes with 3D imaging capability were proposed.

The first GBSAR used the bistatic principle in order to obtain the elevation resolution. This monostatic/bistatic GBSAR system was demonstrated able to produce 2D images in short times (about a half hour) and 3D images in long times (several hours). It is worth to note that this radar configuration has been obtained as an upgrade of a linear monostatic GBSAR. The bistatic 3D system shares the radar head and the horizontal mechanical axis with the 2D linear monostatic GBSAR. To improve the images resolution the central frequency can be increased (the prototype operated in X band, but the majority of GBSAR operates in  $K_U$  band). It is possible also to increasing the height of the vertical axis twice. In practice, a GBSAR operating at 17 GHz with a vertical axis of 3 m has vertical resolution about four times better to the equipment presented in this thesis, and this can make the difference in many applications.

The second GBSAR system used a hybrid working principle: synthetic aperture for azimuth resolution, and compressive sensing MIMO for elevation resolution. Also this system is able to provide a 3D image and the azimuth resolution can be improved by increasing the bandwidth and the scan length. On the contrary of azimuth resolution, elevation resolution does not depend on central frequency, but on the number of antennas used.

The radar with 3D capability fascinates both the expert and the users. The solution presented in this thesis can be used for monitoring particular scenario while they are, in certain way, a retrofit of conventional GBSAR. This system, operating in higher (and wider) frequency could be used as high resolution 3D scanner.

## Industrialization

The radar systems presented in this thesis are subject of three patents (property of the University of Florence).

The patent related to bistatic radar was licensed by the University to a company, leader of GBRI sector, and probably it will be produce in short time. Regarding the patents on the CS-MIMO radar and ON the 3 di-

mensional GBSAR using monostatic/bistatic technique the University of Florence is currently negotiating for their licensing.



## References

- [1] M. Borgeaud, J. Noll, and A. Bellini, “Multi-temporal comparisons of ERS-1 and JERS-1 SAR data for land applications,” in *International Geoscience and Remote Sensing Symposium (IGARSS)*, vol. 3, 1994, pp. 1603–1605.
- [2] S. Srivastava, T. Lukowski, R. Gray, N. Shepherd, and R. Hawkins, “RADARSAT: image quality management and performance results,” in *Canadian Conference on Electrical and Computer Engineering*, vol. 1, 1996, pp. 21–23.
- [3] D. Massonnet, M. Rossi, C. Carmona, F. Adragna, G. Peltzer, K. Feigl, and T. Rabaute, “The displacement field of the Landers earthquake mapped by radar interferometry,” *Nature*, vol. 364, no. 6433, pp. 138–142, 1993.
- [4] S. Atzori, I. Hunstad, M. Chini, S. Salvi, C. Tolomei, C. Bignami, S. Stramondo, E. Trasatti, A. Antonoli, and E. Boschi, “Finite fault inversion of DInSAR coseismic displacement of the 2009 L’Aquila earthquake (central Italy),” *Geophysical Research Letters*, vol. 36, no. 15, 2009.
- [5] D. Tarchi, E. Ohlmer, and A. Sieber, “Monitoring of structural changes by radar interferometry,” *Research in Nondestructive Evaluation*, vol. 9, no. 4, pp. 213–225, 1997.
- [6] D. Tarchi, H. Rudolf, G. Luzi, L. Chiarantini, P. Coppo, and A. Sieber, “SAR interferometry for structural changes detection: a demonstration test

- on a dam,” in *International Geoscience and Remote Sensing Symposium (IGARSS)*, vol. 3, 1999, pp. 1522–1524.
- [7] M. Pieraccini, D. Tarchi, H. Rudolf, D. Leva, G. Luzi, G. Bartoli, and C. Atzeni, “Structural static testing by interferometric synthetic radar,” *NDT & E International*, vol. 33, no. 8, pp. 565–570, Dec. 2000. [Online]. Available: <http://linkinghub.elsevier.com/retrieve/pii/S096386950000027X>
- [8] D. Tarchi, N. Casagli, R. Fanti, D. Leva, G. Luzi, A. Pasuto, M. Pieraccini, and S. Silvano, “Landslide monitoring by using ground-based SAR interferometry: An example of application to the Tessina landslide in Italy,” *Engineering Geology*, vol. 68, no. 1-2, pp. 15–30, 2003.
- [9] T. Farr, P. Rosen, E. Caro, R. Crippen, R. Duren, S. Hensley, M. Kobrick, M. Paller, E. Rodriguez, L. Roth, D. Seal, S. Shaffer, J. Shimada, J. Umland, M. Werner, M. Oskin, D. Burbank, and D. Alsdorf, “The shuttle radar topography mission,” *Reviews of Geophysics*, vol. 45, no. 2, 2007.
- [10] L. Noferini, M. Pieraccini, D. Mecatti, G. Macaluso, G. Luzi, and C. Atzeni, “DEM by Ground-Based SAR Interferometry,” *IEEE Geoscience and Remote Sensing Letters*, vol. 4, no. 4, pp. 659–663, Oct. 2007. [Online]. Available: <http://ieeexplore.ieee.org/document/4317540/>
- [11] T. Carlà, V. Tofani, L. Lombardi, F. Raspini, S. Bianchini, D. Bertolo, P. Thuegaz, and N. Casagli, “Combination of GNSS, satellite InSAR, and GBInSAR remote sensing monitoring to improve the understanding of a large landslide in high alpine environment,” *Geomorphology*, vol. 335, pp. 62–75, 2019.
- [12] A. Corsini, P. Farina, G. Antonello, M. Barbieri, N. Casagli, F. Coren, L. Guerri, F. Ronchetti, P. Sterzai, and D. Tarchi, “Space-borne and ground-based SAR interferometry as tools for landslide hazard management in civil protection,” *International Journal of Remote Sensing*, vol. 27, no. 12, pp. 2351–2369, 2006.
- [13] H. Han and H. Lee, “Motion of Campbell glacier, east antarctica, observed by satellite and ground-based interferometric synthetic aperture radar,” in *3rd International Asia-Pacific Conference on Synthetic Aperture Radar, APSAR 2011*, 2011, p. 4.
- [14] M. Pieraccini and L. Miccinesi, “Ground-based radar interferometry: A bibliographic review,” *Remote Sensing*, vol. 11, no. 9, 2019.
- [15] M. Pieraccini, M. Fratini, F. Parrini, and C. Atzeni, “Dynamic Monitoring of Bridges Using a High-Speed Coherent Radar,” *IEEE Transactions on Geoscience and Remote Sensing*, vol. 44, no. 11, pp. 3284–3288, Nov. 2006. [Online]. Available: <http://ieeexplore.ieee.org/document/1717722/>
- [16] C. Atzeni, A. Bicci, D. Dei, M. Fratini, and M. Pieraccini, “Remote Survey of the Leaning Tower of Pisa by Interferometric Sensing,” *IEEE Geoscience and Remote Sensing Letters*, vol. 7, no. 1, pp. 185–189, Jan. 2010. [Online]. Available: <http://ieeexplore.ieee.org/document/5290014/>

- [17] G. Grazzini, M. Pieraccini, D. Dei, and C. Atzeni, "Simple microwave sensor for remote detection of structural vibration," *Electronics Letters*, vol. 45, no. 11, p. 567, 2009. [Online]. Available: <https://digital-library.theiet.org/content/journals/10.1049/el.2009.1107>
- [18] C. Farrar, T. Darling, A. Migliori, and W. Baker, "Microwave interferometers for non-contact vibration measurements on large structures," *Mechanical Systems and Signal Processing*, vol. 13, no. 2, pp. 241–253, 1999.
- [19] B. Reeves, G. Stickley, D. Noon, and I. Longstaff, "Developments in monitoring mine slope stability using radar interferometry," in *IGARSS 2000. IEEE 2000 International Geoscience and Remote Sensing Symposium. Taking the Pulse of the Planet: The Role of Remote Sensing in Managing the Environment. Proceedings (Cat. No.00CH37120)*, vol. 5. Honolulu, HI, USA: IEEE, 2000, pp. 2325–2327. [Online]. Available: <http://ieeexplore.ieee.org/document/858397/>
- [20] C. Werner, T. Strozzi, A. Wiesmann, and U. Wegmüller, "GAMMA'S PORTABLE RADAR INTERFEROMETER," in *13th FIG Symposium on Deformation Measurement Analysis*, Lisbon, Portugal, 2008, p. 10.
- [21] M. Pieraccini, "Real Beam vs. Synthetic aperture radar for slope monitoring," in *Progress in Electromagnetics Research Symposium*, 2013, pp. 1627–1632.
- [22] H. Lee, J.-H. Lee, K.-E. Kim, N.-H. Sung, and S.-J. Cho, "Development of a Truck-Mounted Arc-Scanning Synthetic Aperture Radar," *IEEE Transactions on Geoscience and Remote Sensing*, vol. 52, no. 5, pp. 2773–2779, May 2014. [Online]. Available: <http://ieeexplore.ieee.org/document/6553134/>
- [23] Y. Luo, H. Song, R. Wang, Y. Deng, F. Zhao, and Z. Xu, "Arc FMCW sar and applications in ground monitoring," *IEEE Transactions on Geoscience and Remote Sensing*, vol. 52, no. 9, pp. 5989–5998, 2014.
- [24] M. Pieraccini and L. Miccinesi, "ArcSAR: Theory, Simulations, and Experimental Verification," *IEEE Transactions on Microwave Theory and Techniques*, vol. 65, no. 1, pp. 293–301, Jan. 2017. [Online]. Available: <http://ieeexplore.ieee.org/document/7588999/>
- [25] D. Tarchi, F. Oliveri, and P. Sammartino, "MIMO radar and ground-based SAR imaging systems: Equivalent approaches for remote sensing," *IEEE Transactions on Geoscience and Remote Sensing*, vol. 51, no. 1, pp. 425–435, 2013.
- [26] C. Hu, J. Wang, W. Tian, T. Zeng, and R. Wang, "Design and imaging of ground-based multiple-input multiple-output synthetic aperture radar (MIMO SAR) with non-collinear arrays," *Sensors (Switzerland)*, vol. 17, no. 3, 2017.
- [27] K. Lukin, A. Mogila, P. Vyplavin, G. Galati, and G. Pavan, "Novel concepts for surface movement radar design," *International Journal of Microwave and*

- Wireless Technologies*, vol. 1, no. 03, p. 163, Jun. 2009. [Online]. Available: [http://www.journals.cambridge.org/abstract\\_S1759078709000233](http://www.journals.cambridge.org/abstract_S1759078709000233)
- [28] Online, accessed on 31 July 2019. [Online]. Available: <https://idsgeoradar.com>
- [29] Online, accessed on 30 July 2019. [Online]. Available: <https://www.groundprobe.com>
- [30] M. Pieraccini and L. Miccinesi, “An Interferometric MIMO Radar for Bridge Monitoring,” *IEEE Geoscience and Remote Sensing Letters*, pp. 1–5, 2019.
- [31] A. Martinez-Vazquez, J. Fortuny-Guasch, and U. Gruber, “Monitoring of the snow cover,” in *EARSel eProceedings*, 2005, p. 8.
- [32] G. Luzi, L. Noferini, D. Mecatti, G. Macaluso, M. Pieraccini, C. Atzeni, A. Schaffhauser, R. Fromm, and T. Nagler, “Using a Ground-Based SAR Interferometer and a Terrestrial Laser Scanner to Monitor a Snow-Covered Slope: Results From an Experimental Data Collection in Tyrol (Austria),” *IEEE Transactions on Geoscience and Remote Sensing*, vol. 47, no. 2, pp. 382–393, Feb. 2009. [Online]. Available: <http://ieeexplore.ieee.org/document/4773466/>
- [33] A. Martinez-Vazquez and J. Fortuny-Guasch, “A GB-SAR Processor for Snow Avalanche Identification,” *IEEE Transactions on Geoscience and Remote Sensing*, vol. 46, no. 11, pp. 3948–3956, Nov. 2008. [Online]. Available: <http://ieeexplore.ieee.org/document/4686196/>
- [34] J. Hasch, E. Topak, R. Schnabel, T. Zwick, R. Weigel, and C. Waldschmidt, “Millimeter-wave technology for automotive radar sensors in the 77 GHz frequency band,” *IEEE Transactions on Microwave Theory and Techniques*, vol. 60, no. 3 PART 2, pp. 845–860, 2012.
- [35] E. Intrieri, G. Gigli, M. Nocentini, L. Lombardi, F. Mugnai, F. Fidolini, and N. Casagli, “Sinkhole monitoring and early warning: An experimental and successful GB-InSAR application,” *Geomorphology*, vol. 241, pp. 304–314, 2015.
- [36] L. Lombardi, M. Nocentini, W. Frodella, T. Nolesini, F. Bardi, E. Intrieri, T. Carlà, L. Solari, G. Dotta, F. Ferrigno, and N. Casagli, “The Calatabiano landslide (southern Italy): preliminary GB-InSAR monitoring data and remote 3d mapping,” *Landslides*, vol. 14, no. 2, pp. 685–696, Apr. 2017. [Online]. Available: <https://doi.org/10.1007/s10346-016-0767-6>
- [37] W. Frodella, A. Ciampalini, F. Bardi, T. Salvatici, F. Di Traglia, G. Basile, and N. Casagli, “A method for assessing and managing landslide residual hazard in urban areas,” *Landslides*, vol. 15, no. 2, pp. 183–197, 2018.
- [38] L. Noferini, M. Pieraccini, G. Luzi, D. Mecatti, G. Macaluso, and C. Atzeni, “Ground-based radar interferometry for monitoring unstable slopes,” in *International Geoscience and Remote Sensing Symposium (IGARSS)*, 2006, pp. 4088–4091.

- [39] M. Pieraccini, G. Luzi, D. Mecatti, M. Fratini, L. Noferini, L. Carissimi, G. Franchioni, and C. Atzeni, "Remote sensing of building structural displacements using a microwave interferometer with imaging capability," *NDT and E International*, vol. 37, no. 7, pp. 545–550, 2004.
- [40] N. Harries, D. Noon, H. Pritchett, and D. Bates, "Slope Stability Radar for Managing Rock Fall Risks in Open Cut Mines," in *proceedings of the 3rd CANUS Rock Mechanics Symposium*, Toronto, 2009, p. 8.
- [41] A. Serrano-Juan, E. Vázquez-Suñè, O. Monserrat, M. Crosetto, C. Hoffmann, A. Ledesma, R. Criollo, E. Pujades, V. Velasco, A. Garcia-Gil, and M. Alcaraz, "Gb-SAR interferometry displacement measurements during dewatering in construction works. Case of La Sagrera railway station in Barcelona, Spain," *Engineering Geology*, vol. 205, pp. 104–115, 2016.
- [42] M. Pieraccini, L. Noferini, D. Mecatti, C. Atzeni, G. Teza, A. Galgaro, and N. Zaltron, "Integration of Radar Interferometry and Laser Scanning for Remote Monitoring of an Urban Site Built on a Sliding Slope," *IEEE Transactions on Geoscience and Remote Sensing*, vol. 44, no. 9, pp. 2335–2342, Sep. 2006. [Online]. Available: <http://ieeexplore.ieee.org/document/1677743/>
- [43] L. Pipia, X. Fabregas, A. Aguasca, C. Lopez-Martinez, S. Duque, J. J. Mallorqui, and J. Marturia, "Polarimetric Differential SAR Interferometry: First Results With Ground-Based Measurements," *IEEE Geoscience and Remote Sensing Letters*, vol. 6, no. 1, pp. 167–171, Jan. 2009. [Online]. Available: <http://ieeexplore.ieee.org/document/4729620/>
- [44] G. Luzi, M. Crosetto, and M. Cuevas-González, "A radar-based monitoring of the Collserola tower (Barcelona)," *Mechanical Systems and Signal Processing*, vol. 49, no. 1, pp. 234–248, Dec. 2014. [Online]. Available: <http://www.sciencedirect.com/science/article/pii/S0888327014001253>
- [45] D. Mecatti, L. Noferini, G. Macaluso, M. Pieraccini, G. Luzi, C. Atzeni, and A. Tamburini, "Remote sensing of glacier by ground-based radar interferometry," in *International Geoscience and Remote Sensing Symposium (IGARSS)*, 2007, pp. 4501–4504.
- [46] M. Pieraccini, M. Betti, D. Forcellini, D. Dei, F. Papi, G. Bartoli, L. Facchini, R. Corazzi, and V. C. Kovacevic, "Radar detection of pedestrian-induced vibrations on Michelangelo's David," *PLOS ONE*, vol. 12, no. 4, p. e0174480, Apr. 2017. [Online]. Available: <https://dx.plos.org/10.1371/journal.pone.0174480>
- [47] S. Calvari, E. Intrieri, F. Di Traglia, A. Bonaccorso, N. Casagli, and A. Cristaldi, "Monitoring crater-wall collapse at active volcanoes: a study of the 12 January 2013 event at Stromboli," *Bulletin of Volcanology*, vol. 78, no. 5, p. 39, Apr. 2016. [Online]. Available: <https://doi.org/10.1007/s00445-016-1033-4>
- [48] J. Oerlemans, B. Anderson, A. Hubbard, P. Huybrechts, T. Jóhannesson, W. Knap, M. Schmeits, A. Stroeven, R. Van De Wal, J. Wallinga, and

- Z. Zuo, "Modelling the response of glaciers to climate warming," *Climate Dynamics*, vol. 14, no. 4, pp. 267–274, 1998.
- [49] G. Luzi, M. Pieraccini, D. Mecatti, L. Noferini, G. Macaluso, A. Tamburini, and C. Atzeni, "Monitoring of an Alpine Glacier by Means of Ground-Based SAR Interferometry," *IEEE Geoscience and Remote Sensing Letters*, vol. 4, no. 3, pp. 495–499, Jul. 2007. [Online]. Available: <http://ieeexplore.ieee.org/document/4271456/>
- [50] A. Chapuis, C. Rolstad, and R. Norland, "Interpretation of amplitude data from a ground-based radar in combination with terrestrial photogrammetry and visual observations for calving monitoring of Kronebreen, Svalbard," *Annals of Glaciology*, vol. 51, no. 55, pp. 34–40, 2010.
- [51] S. Xie, T. Dixon, D. Voytenko, D. Holland, D. Holland, and T. Zheng, "Precursor motion to iceberg calving at Jakobshavn Isbræ, Greenland, observed with terrestrial radar interferometry," *Journal of Glaciology*, vol. 62, no. 236, pp. 1134–1142, 2016.
- [52] M. Pieraccini, "Extensive Measurement Campaign Using Interferometric Radar," *Journal of Performance of Constructed Facilities*, vol. 31, no. 3, p. 04016113, Jun. 2017. [Online]. Available: <http://ascelibrary.org/doi/10.1061/%28ASCE%29CF.1943-5509.0000987>
- [53] M. Pieraccini, M. Fratini, D. Dei, and C. Atzeni, "Structural testing of Historical Heritage Site Towers by microwave remote sensing," *Journal of Cultural Heritage*, vol. 10, no. 2, pp. 174–182, Apr. 2009. [Online]. Available: <https://linkinghub.elsevier.com/retrieve/pii/S1296207409000193>
- [54] M. Fratini, M. Pieraccini, C. Atzeni, M. Betti, and G. Bartoli, "Assessment of vibration reduction on the Baptistery of San Giovanni in Florence (Italy) after vehicular traffic block," *Journal of Cultural Heritage*, vol. 12, no. 3, pp. 323–328, Jul. 2011. [Online]. Available: <https://linkinghub.elsevier.com/retrieve/pii/S1296207411000112>
- [55] D. Tapete, N. Casagli, G. Luzi, R. Fanti, G. Gigli, and D. Leva, "Integrating radar and laser-based remote sensing techniques for monitoring structural deformation of archaeological monuments," *Journal of Archaeological Science*, vol. 40, no. 1, pp. 176–189, 2013.
- [56] F. Pratesi, T. Nolesini, S. Bianchini, D. Leva, L. Lombardi, R. Fanti, and N. Casagli, "Early Warning GBInSAR-Based Method for Monitoring Volterra (Tuscany, Italy) City Walls," *IEEE Journal of Selected Topics in Applied Earth Observations and Remote Sensing*, vol. 8, no. 4, pp. 1753–1762, Apr. 2015.
- [57] M. Pieraccini, D. Dei, M. Betti, G. Bartoli, G. Tucci, and N. Guardini, "Dynamic identification of historic masonry towers through an expeditious and no-contact approach: Application to the "Torre del Mangia" in Siena (Italy)," *Journal of Cultural Heritage*, vol. 15, no. 3, pp. 275–282, May 2014. [Online]. Available: <https://linkinghub.elsevier.com/retrieve/pii/S129620741300160X>

- [58] A. Castellano, A. Fraddosio, F. Martorano, G. Mininno, F. Paparella, and M. D. Piccioni, "Structural health monitoring of a historic masonry bell tower by radar interferometric measurements," in *2018 IEEE Workshop on Environmental, Energy, and Structural Monitoring Systems (EESMS)*. Salerno: IEEE, Jun. 2018, pp. 1–6. [Online]. Available: <https://ieeexplore.ieee.org/document/8405824/>
- [59] F. Di Traglia, T. Nolesini, A. Ciampalini, L. Solari, W. Frodella, F. Bellotti, A. Fumagalli, G. De Rosa, and N. Casagli, "Tracking morphological changes and slope instability using spaceborne and ground-based SAR data," *Geomorphology*, vol. 300, pp. 95–112, 2018.
- [60] T. Nolesini, F. Di Traglia, C. Del Ventisette, S. Moretti, and N. Casagli, "Deformations and slope instability on Stromboli volcano: Integration of GBInSAR data and analog modeling," *Geomorphology*, vol. 180-181, pp. 242–254, 2013.
- [61] F. Di Traglia, E. Intrieri, T. Nolesini, F. Bardi, C. Del Ventisette, F. Ferrigno, S. Frangioni, W. Frodella, G. Gigli, A. Lotti, C. Stefanelli, L. Tanteri, D. Leva, and N. Casagli, "The ground-based InSAR monitoring system at Stromboli volcano: Linking changes in displacement rate and intensity of persistent volcanic activity," *Bulletin of Volcanology*, vol. 76, no. 2, pp. 1–18, 2014.
- [62] F. Di Traglia, T. Nolesini, L. Solari, A. Ciampalini, W. Frodella, D. Steri, B. Allotta, A. Rindi, L. Marini, N. Monni, E. Galardi, and N. Casagli, "Lava delta deformation as a proxy for submarine slope instability," *Earth and Planetary Science Letters*, vol. 488, pp. 46–58, 2018.
- [63] E. Intrieri, F. Di Traglia, C. Del Ventisette, G. Gigli, F. Mugnai, G. Luzi, and N. Casagli, "Flank instability of Stromboli volcano (Aeolian Islands, Southern Italy): Integration of GB-InSAR and geomorphological observations," *Geomorphology*, vol. 201, pp. 60–69, Nov. 2013. [Online]. Available: <http://www.sciencedirect.com/science/article/pii/S0169555X1300319X>
- [64] G. Antonello, J. Fortuny, D. Tarchi, N. Casagli, C. Del Ventisette, L. Guerri, G. Luzi, F. Mugnai, and D. Leva, "Microwave interferometric sensors as a tool for space and time analysis of active volcano deformations: The Stromboli case," in *2008 Second Workshop on Use of Remote Sensing Techniques for Monitoring Volcanoes and Seismogenic Areas*. Napoli, Italy: IEEE, Nov. 2008, pp. 1–6. [Online]. Available: <http://ieeexplore.ieee.org/document/4740332/>
- [65] G. Wadge, D. Macfarlane, D. Robertson, A. Hale, H. Pinkerton, R. Burrell, G. Norton, and M. James, "AVTIS: A novel millimetre-wave ground based instrument for volcano remote sensing," *Journal of Volcanology and Geothermal Research*, vol. 146, no. 4, pp. 307–318, Sep. 2005. [Online]. Available: <https://linkinghub.elsevier.com/retrieve/pii/S0377027305000739>

- [66] S. Kuraoka, Y. Nakashima, R. Doke, and K. Mannen, "Monitoring ground deformation of eruption center by ground-based interferometric synthetic aperture radar (GB-InSAR): a case study during the 2015 phreatic eruption of Hakone volcano," *Earth, Planets and Space*, vol. 70, no. 1, p. 181, Dec. 2018. [Online]. Available: <https://earth-planets-space.springeropen.com/articles/10.1186/s40623-018-0951-0>
- [67] L. Noferini, M. Pieraccini, G. Luzi, D. Mecatti, G. Macaluso, and C. Atzeni, "Ground-based radar interferometry for terrain mapping," in *International Geoscience and Remote Sensing Symposium (IGARSS)*, 2006, pp. 2569–2572.
- [68] A. Schaffhauser, M. Adams, R. Fromm, P. Jörg, G. Luzi, L. Noferini, and R. Sailer, "Remote sensing based retrieval of snow cover properties," *Cold Regions Science and Technology*, vol. 54, no. 3, pp. 164–175, Nov. 2008. [Online]. Available: <http://www.sciencedirect.com/science/article/pii/S0165232X08001079>
- [69] Zheng-Shu Zhou, W.-M. Boerner, and M. Sato, "Development of a ground-based polarimetric broadband SAR system for noninvasive ground-truth validation in vegetation monitoring," *IEEE Transactions on Geoscience and Remote Sensing*, vol. 42, no. 9, pp. 1803–1810, Sep. 2004. [Online]. Available: <http://ieeexplore.ieee.org/document/1333165/>
- [70] P. Bukenya, P. Moyo, H. Beushausen, and C. Oosthuizen, "Health monitoring of concrete dams: A literature review," *Journal of Civil Structural Health Monitoring*, vol. 4, no. 4, pp. 235–244, 2014.
- [71] K. Luoju, J. Pulliainen, S. Metsämäki, and M. Hallikainen, "Snow-covered area estimation using satellite radar wide-swath images," *IEEE Transactions on Geoscience and Remote Sensing*, vol. 45, no. 4, pp. 978–988, 2007.
- [72] J. Broussolle, V. Kyovtorov, M. Basso, G. Ferraro Di Silvi E Castiglione, J. Figueiredo Morgado, R. Giuliani, F. Oliveri, P. F. Sammartino, and D. Tarchi, "MELISSA, a new class of ground based InSAR system. An example of application in support to the Costa Concordia emergency," *ISPRS Journal of Photogrammetry and Remote Sensing*, vol. 91, pp. 50–58, May 2014. [Online]. Available: <https://linkinghub.elsevier.com/retrieve/pii/S0924271614000409>
- [73] G. Nico, G. Cifarelli, G. Miccoli, F. Soccodato, W. Feng, M. Sato, S. Miliziano, and M. Marini, "Measurement of Pier Deformation Patterns by Ground-Based SAR Interferometry: Application to a Bollard Pull Trial," *IEEE Journal of Oceanic Engineering*, vol. 43, no. 4, pp. 822–829, Oct. 2018. [Online]. Available: <https://ieeexplore.ieee.org/document/8409936/>
- [74] C. Li, R. Bhalla, and H. Ling, "Investigation of the Dynamic Radar Signatures of a Vertical-Axis Wind Turbine," *IEEE Antennas and Wireless Propagation Letters*, vol. 14, pp. 763–766, 2015.
- [75] J.-M. Munoz-Ferreras, Z. Peng, Y. Tang, R. Gomez-Garcia, D. Liang, and C. Li, "A step forward towards radar sensor networks for structural health



- monitoring of wind turbines,” in *IEEE Radio and Wireless Symposium, RWS*, vol. 2016-March, 2016, pp. 23–25.
- [76] C. Li, S.-T. Yang, and H. Ling, “In-Situ ISAR Imaging of Wind Turbines,” *IEEE Transactions on Antennas and Propagation*, vol. 64, no. 8, pp. 3587–3596, 2016.
- [77] T. Jeffrey, *Phased-array radar design: Application of radar fundamentals*, ser. Phased-Array Radar Design: Application of Radar Fundamentals. Scitech Publishing, 2009.
- [78] W. Hong, W. Tan, Y. Wang, and Y. Wu, “Development and Experiments of Ground-Based SAR in IECAS for Advanced SAR Imaging Technique Validation,” in *EUSAR 2010*, 2010, p. 4.
- [79] D. Dei, D. Mecatti, and M. Pieraccini, “Static Testing of a Bridge Using an Interferometric Radar: The Case Study of “Ponte degli Alpini, Belluno”, Italy,” *The Scientific World Journal*, vol. 2013, pp. 1–7, 2013. [Online]. Available: <http://www.hindawi.com/journals/tswj/2013/504958/>
- [80] J. Severin, E. Eberhardt, L. Leoni, and S. Fortin, “Development and application of a pseudo-3d pit slope displacement map derived from ground-based radar,” *Engineering Geology*, vol. 181, pp. 202–211, Oct. 2014. [Online]. Available: <https://linkinghub.elsevier.com/retrieve/pii/S0013795214001823>
- [81] T. Zeng, C. Mao, C. Hu, X. Yang, and W. Tian, “Multi-static MIMO-SAR three dimensional deformation measurement system,” in *2015 IEEE 5th Asia-Pacific Conference on Synthetic Aperture Radar (APSAR)*. Singapore, Singapore: IEEE, Sep. 2015, pp. 297–301. [Online]. Available: <http://ieeexplore.ieee.org/document/7306212/>
- [82] C. Hu, Y. Deng, R. Wang, W. Tian, and T. Zeng, “Two-Dimensional Deformation Measurement Based on Multiple Aperture Interferometry in Gb-SAR,” *IEEE Geoscience and Remote Sensing Letters*, vol. 14, no. 2, pp. 208–212, 2017.
- [83] M. Pieraccini, F. Papi, and S. Rocchio, “Interferometric RotoSAR,” *Electronics Letters*, vol. 51, no. 18, pp. 1451–1453, 2015.
- [84] M. Pieraccini and L. Miccinesi, “RotoSAR for monitoring bridges,” in *European Microwave Week 2017: "A Prime Year for a Prime Event", EuMW 2017 - Conference Proceedings; 14th European Microwave Conference, EU-RAD 2017*, vol. 2018-January, 2018, pp. 311–314.
- [85] J. Lopez-Sanchez and J. Fortuny-Guasch, “3-D radar imaging using range migration techniques,” *IEEE Transactions on Antennas and Propagation*, vol. 48, no. 5, pp. 728–737, 2000.
- [86] D. Tarchi, H. Rudolf, M. Pieraccini, and C. Atzeni, “Remote monitoring of buildings using a ground-based SAR: Application to cultural heritage survey,” *International Journal of Remote Sensing*, vol. 21, no. 18, pp. 3545–3551, 2000.

- [87] M. Frukacz and A. Wieser, "On the impact of rockfall catch fences on ground-based radar interferometry," *Landslides*, vol. 14, no. 4, pp. 1431–1440, 2017.
- [88] D. D'Aria, G. Amoroso, A. Bicci, F. Coppi, M. Cecchetti, M. Rossi, and P. Falcone, "Advanced tomographic tool for HYDRA radar system," in *Proceedings of the European Conference on Synthetic Aperture Radar, EUSAR*, vol. 2018-June, 2018, pp. 484–486.
- [89] C. Ma, T. Yeo, Y. Zhao, and J. Feng, "MIMO radar 3d imaging based on combined amplitude and total variation cost function with sequential order one negative exponential form," *IEEE Transactions on Image Processing*, vol. 23, no. 5, pp. 2168–2183, 2014.
- [90] Online, accessed on 31 July 2019. [Online]. Available: <https://idsgeoradar.com/products/interferometric-radar/ibis-fm>
- [91] S. Placidi, A. Meta, L. Testa, and S. Rodelsperger, "Monitoring structures with FastGBSAR," in *2015 IEEE Radar Conference - Proceedings*, 2015, pp. 435–439.
- [92] M. Pieraccini and F. Papi, "Design of A CW-SF Ground Penetrating Radar," in *2016 IEEE International Geoscience and Remote Sensing Symposium (IGARSS)*, Jul. 2016, pp. 7430–7433.
- [93] M. I. Skolnik, *Radar handbook*, 3rd ed. McGraw-Hill, Incorporated, 1970.
- [94] M. Pieraccini, G. Luzi, and C. Atzeni, "Terrain mapping by ground-based interferometric radar," *IEEE Transactions on Geoscience and Remote Sensing*, vol. 39, no. 10, pp. 2176–2181, 2001.
- [95] O. Monserrat, M. Crosetto, and G. Luzi, "A review of ground-based SAR interferometry for deformation measurement," *ISPRS Journal of Photogrammetry and Remote Sensing*, vol. 93, pp. 40–48, 2014.
- [96] L. Iannini and A. Monti Guarnieri, "Atmospheric phase screen in ground-based radar: Statistics and compensation," *IEEE Geoscience and Remote Sensing Letters*, vol. 8, no. 3, pp. 537–541, 2011.
- [97] R. Iglesias, X. Fabregas, A. Aguasca, J. Mallorqui, C. Lopez-Martinez, J. Gili, and J. Corominas, "Atmospheric phase screen compensation in ground-based sar with a multiple-regression model over mountainous regions," *IEEE Transactions on Geoscience and Remote Sensing*, vol. 52, no. 5, pp. 2436–2449, 2014.
- [98] X. Zhang, B.-Y. Lu, Q. Song, and M. Leng, "Atmospheric disturbance correction in Ground-Based SAR differential interferometry," in *Proceedings of 2011 IEEE CIE International Conference on Radar, RADAR 2011*, vol. 2, 2011, pp. 1574–1577.
- [99] L. Noferini, M. Pieraccini, D. Mecatti, G. Luzi, C. Atzeni, A. Tamburini, and M. Broccolato, "Permanent scatterers analysis for atmospheric correction in ground-based SAR interferometry," *IEEE Transactions on Geoscience and Remote Sensing*, vol. 43, no. 7, pp. 1459–1470, 2005.

- [100] A. Moreira, P. Prats-Iraola, M. Younis, G. Krieger, I. Hajnsek, and K. Papathanassiou, "A tutorial on synthetic aperture radar," *IEEE Geoscience and Remote Sensing Magazine*, vol. 1, no. 1, pp. 6–43, 2013.
- [101] M. Pieraccini, "Monitoring of civil infrastructures by interferometric radar: A review," *The Scientific World Journal*, vol. 2013, 2013.
- [102] M. Crosetto, O. Monserrat, G. Luzi, M. Cuevas-Gonzalez, and N. Devanthery, "A noninterferometric procedure for deformation measurement using GB-SAR imagery," *IEEE Geoscience and Remote Sensing Letters*, vol. 11, no. 1, pp. 34–38, 2014.
- [103] M. Pieraccini, L. Miccinesi, and N. Rojhani, "A GBSAR Operating in Monostatic and Bistatic Modalities for Retrieving the Displacement Vector," *IEEE Geoscience and Remote Sensing Letters*, vol. 14, no. 9, pp. 1494–1498, Sep. 2017. [Online]. Available: <http://ieeexplore.ieee.org/document/7976377/>
- [104] M. Pieraccini and L. Miccinesi, "Bistatic ground-based synthetic aperture radar," in *Proceedings of the European Conference on Synthetic Aperture Radar, EUSAR*, vol. 2018-June, 2018, pp. 275–279.
- [105] M. Pieraccini, L. Miccinesi, "Bistatic ArcSAR," in *2018 URSI*, 2018, pp. 1–4.
- [106] M. Lapo and P. Massimiliano, "Monostatic/Bistatic interferometric radar for monitoring slender structures," in *2019 IEEE Conference on Antenna Measurements & Applications (CAMA)*. IEEE, 2019.
- [107] E. Laubie, B. Rigling, and R. Penno, "Bistatic SAR image registration accuracy," vol. 2015-June, 2015, pp. 742–746.
- [108] S.-G. Zhou, P.-K. Tan, and T.-H. Chio, "Low-profile, wideband dual-polarized antenna with high isolation and low cross polarization," *IEEE Antennas and Wireless Propagation Letters*, vol. 11, pp. 1032–1035, 2012.
- [109] M. Pieraccini and L. Miccinesi, "Cross-pol transponder with frequency shifter for bistatic ground-based synthetic aperture radar," *Remote Sensing*, vol. 10, no. 9, 2018.
- [110] M. Pieraccini, "Noise Performance Comparison Between Continuous Wave and Stroboscopic Pulse Ground Penetrating Radar," *IEEE Geoscience and Remote Sensing Letters*, vol. 15, no. 2, pp. 222–226, 2018.
- [111] D. Dei, M. Pieraccini, M. Fratini, C. Atzeni, and G. Bartoli, "Detection of vertical bending and torsional movements of a bridge using a coherent radar," *NDT and E International*, vol. 42, no. 8, pp. 741–747, 2009.
- [112] M. Pieraccini, D. Tarchi, H. Rudolf, D. Leva, G. Luzi, and C. Atzeni, "Interferometric radar for remote monitoring of building deformations," *Electronics Letters*, vol. 36, no. 6, pp. 569–570, 2000.
- [113] M. Pieraccini and L. Miccinesi, "Cross-pol long-cable transponder for bistatic ground-based synthetic aperture radar," *Electronics Letters*, vol. 54, no. 21, pp. 1233–1235, 2018.

- [114] E. Carden and P. Fanning, "Vibration based condition monitoring: A review," *Structural Health Monitoring*, vol. 3, no. 4, pp. 355–377, 2004.
- [115] M. PIERACCINI, P. CAMELIA, and M. BETTI, "A method and apparatus for monitoring slender elements by means of dynamic measurements of structural asymmetry," WO Patent WO2016 059 462A1, Apr., 2016. [Online]. Available: <https://patents.google.com/patent/WO2016059462A1/en?q=A&q=method&q=apparatus&q=monitoring&q=slender&q=elements&q=means&q=dynamic&q=measurements&q=structural&q=asymmetry&oq=A+method+and+apparatus+for+monitoring+slender+elements+by+means+of+dynamic+measurements+of+structural+asymmetry>
- [116] F. Viviani, A. Micheleni, L. Mayer, and F. Conni, "IBIS-ArcSAR: an Innovative Ground-Based SAR System for Slope Monitoring," in *IGARSS 2018 - 2018 IEEE International Geoscience and Remote Sensing Symposium*, Jul. 2018, pp. 1348–1351.
- [117] S. Qian and D. Chen, "Joint Analysis," *IEEE Signal Processing Magazine*, vol. 16, no. 2, pp. 52–67, 1999.
- [118] E. Candés and M. Wakin, "An introduction to compressive sampling: A sensing/sampling paradigm that goes against the common knowledge in data acquisition," *IEEE Signal Processing Magazine*, vol. 25, no. 2, pp. 21–30, 2008.
- [119] A. Massa, P. Rocca, and G. Oliveri, "Compressive sensing in electromagnetics - A review," *IEEE Antennas and Propagation Magazine*, vol. 57, no. 1, pp. 224–238, 2015.
- [120] M. Hadi, S. Alshebeili, K. Jamil, and F. El-Samie, "Compressive sensing applied to radar systems: an overview," *Signal, Image and Video Processing*, vol. 9, pp. 25–39, 2015.
- [121] Q. Huang, L. Qu, B. Wu, and G. Fang, "UWB through-wall imaging based on compressive sensing," *IEEE Transactions on Geoscience and Remote Sensing*, vol. 48, no. 3 PART2, pp. 1408–1415, 2010.
- [122] R. Karlina and M. Sato, "Compressive sensing applied to imaging by ground-based polarimetric SAR," 2011, pp. 2861–2864.
- [123] M. Zonno, "GBSAR data focusing based on compressive sensing," vol. Proceedings of the European Conference on Synthetic Aperture Radar, EUSAR, 2014, pp. 347–350.
- [124] E. Yigit, S. Demirci, A. Unal, C. Ozdemir, and A. Vertiy, "Millimeter-wave ground-based synthetic aperture radar imaging for foreign object debris detection: Experimental studies at short ranges," *Journal of Infrared, Millimeter, and Terahertz Waves*, vol. 33, no. 12, pp. 1227–1238, 2012.
- [125] R. Giordano, P. Guccione, G. Cifarelli, L. Mascolo, and G. Nico, "Focusing SAR images by compressive sensing: Study of interferometric properties," vol. 2015-November, 2015, pp. 5352–5355.

- [126] W. Feng, L. Yi, and M. Sato, "Near range radar imaging based on block sparsity and cross-correlation fusion algorithm," *IEEE Journal of Selected Topics in Applied Earth Observations and Remote Sensing*, vol. 11, no. 6, pp. 2079–2089, 2018.
- [127] M. Pieraccini, N. Rojhani, and L. Miccinesi, "Compressive Sensing for Ground Based Synthetic Aperture Radar," *Remote Sensing*, vol. 10, no. 12, p. 1960, Dec. 2018. [Online]. Available: <http://www.mdpi.com/2072-4292/10/12/1960>
- [128] M. Pieraccini, L. Miccinesi, and N. Rojhani, "Monitoring of Vespucci bridge in Florence, Italy using a fast real aperture radar and a MIMO radar," in *IGARSS 2019 - 2019 IEEE International Geoscience and Remote Sensing Symposium*. IEEE, 2019.
- [129] L. He and L. Carin, "Exploiting structure in wavelet-based bayesian compressive sensing," *IEEE Transactions on Signal Processing*, vol. 57, no. 9, pp. 3488–3497, 2009.
- [130] C. K. Chui, *An Introduction to Wavelets*. Elsevier, Jun. 2016, google-Books-ID: IC1fDAAAQBAJ.
- [131] J. S. Walker, *A Primer on Wavelets and Their Scientific Applications*. CRC Press, Jul. 2019. [Online]. Available: <https://www.taylorfrancis.com/books/9780429129421>
- [132] M. V. Wickerhauser, *Adapted Wavelet Analysis : From Theory to Software*. A K Peters/CRC Press, Apr. 1996. [Online]. Available: <https://www.taylorfrancis.com/books/9780429064258>
- [133] A. Yang, S. Sastry, A. Ganesh, and Y. Ma, "Fast  $\ell_1$ -minimization algorithms and an application in robust face recognition: A review," 2010, pp. 1849–1852.
- [134] R. G. Baraniuk, "Compressive Sensing [Lecture Notes]," *IEEE Signal Processing Magazine*, vol. 24, no. 4, pp. 118–121, Jul. 2007.
- [135] J. Tropp and A. Gilbert, "Signal recovery from random measurements via orthogonal matching pursuit," *IEEE Transactions on Information Theory*, vol. 53, no. 12, pp. 4655–4666, 2007.
- [136] D. Salomon, *Data Compression: The Complete Reference*. Springer Science & Business Media, Feb. 2004, google-Books-ID: PT1fcX32114C.
- [137] L. Noferini, D. Mecatti, G. Macaluso, M. Pieraccini, and C. Atzeni, "Monitoring of Belvedere Glacier using a wide angle GB-SAR interferometer," *Journal of Applied Geophysics*, vol. 68, no. 2, pp. 289–293, 2009.
- [138] M. Pieraccini, L. Noferini, D. Mecatti, G. Macaluso, G. Luzi, and C. Atzeni, "Digital elevation models by a GBSAR interferometer for monitoring glaciers: The case study of Belvedere Glacier," vol. 4, 2008, pp. IV1061–IV1064.

- [139] M. Pieraccini, G. Luzi, D. Mecatti, L. Noferini, and C. Atzeni, “Ground-based SAR for short and long term monitoring of unstable slopes,” 2007, pp. 92–95.
- [140] M. L. Pieraccini Massimiliano, Rojhani Neda, “MIMO radar with dense or random pattern: analysis of phase and positioning error sensitivity,” in *2019 Progress in Electromagnetics Research Symposium (PIERS-Rome)*, 2019.
- [141] M. Pieraccini, M. Fratini, F. Parrini, C. Atzeni, and G. Bartoli, “Interferometric radar vs. accelerometer for dynamic monitoring of large structures: An experimental comparison,” *NDT and E International*, vol. 41, no. 4, pp. 258–264, 2008.
- [142] M. Pieraccini, N. Casagli, G. Luzi, D. Tarchi, D. Mecatti, L. Noferini, and C. Atzeni, “Landslide monitoring by ground-based radar interferometry: A field test in Valdarno (Italy),” *International Journal of Remote Sensing*, vol. 24, no. 6, pp. 1385–1391, 2003.
- [143] J. Fortuny, “An efficient 3-D near-field ISAR algorithm,” *IEEE Transactions on Aerospace and Electronic Systems*, vol. 34, no. 4, pp. 1261–1270, 1998.
- [144] M. Pieraccini, N. Rojhani, and L. Miccinesi, “Ground Based Synthetic Aperture Radar with 3d Imaging Capability,” in *2018 15th European Radar Conference, EuRAD 2018*, 2018, pp. 206–209.
- [145] M. PIERACCINI, L. MICCINESI, and N. ROJHANI, “Gbsar con capacità di acquisire immagini tridimensionali,” IT Patent 102 017 000 145 769, Dec., 2017.
- [146] M. Pieraccini, L. Miccinesi, and N. Rojhani, “A radar with 3d imaging capability that uses synthetic aperture in azimuth and compressive sensing mimo in elevation,” in *2019 16th European Radar Conference, EuRAD 2019*, 2019.
- [147] W. Feng, J. Friedt, G. Nico, and M. Sato, “3-D Ground-Based Imaging Radar Based on C-Band Cross-MIMO Array and Tensor Compressive Sensing,” *IEEE Geoscience and Remote Sensing Letters*, pp. 1–5, 2019.
- [148] Z.-S. Zhou, W.-M. Boerner, and M. Sato, “Development of a ground-based polarimetric broadband SAR system for noninvasive ground-truth validation in vegetation monitoring,” *IEEE Transactions on Geoscience and Remote Sensing*, vol. 42, no. 9, pp. 1803–1810, 2004.
- [149] J. Li and P. Stoica, “MIMO radar with colocated antennas,” *IEEE Signal Processing Magazine*, vol. 24, no. 5, pp. 106–114, 2007.
- [150] X. Zhu and R. Bamler, “Tomographic SAR inversion by L1-norm regularization-the compressive sensing approach,” *IEEE Transactions on Geoscience and Remote Sensing*, vol. 48, no. 10, pp. 3839–3846, 2010.
- [151] E. Aguilera, M. Nannini, and A. Reigber, “Wavelet-based compressed sensing for SAR tomography of forested areas,” *IEEE Transactions on Geoscience and Remote Sensing*, vol. 51, no. 12, pp. 5283–5295, 2013.

PREMIO TESI DI DOTTORATO

TITOLI PUBBLICATI

ANNO 2007

Bracardi M., *La Materia e lo Spirito. Mario Ridolfi nel paesaggio umbro*

Coppi E., *Purines as Transmitter Molecules. Electrophysiological Studies on Purinergic Signalling in Different Cell Systems*

Mannini M., *Molecular Magnetic Materials on Solid Surfaces*

Natali I., *The Ur-Portrait. Stephen Hero ed il processo di creazione artistica in A Portrait of the Artist as a Young Man*

Petretto L., *Imprenditore ed Università nello start-up di impresa. Ruoli e relazioni critiche*

ANNO 2008

Bemporad F., *Folding and Aggregation Studies in the Acylphosphatase-Like Family*

Buono A., *Esercito, istituzioni, territorio. Alloggiamenti militari e «case Herme» nello Stato di Milano (secoli XVI e XVII)*

Castenasi S., *La finanza di progetto tra interesse pubblico e interessi privati*

Colica G., *Use of Microorganisms in the Removal of Pollutants from the Wastewater*

Gabbiani C., *Proteins as Possible Targets for Antitumor Metal Complexes: Biophysical Studies of their Interactions*

ANNO 2009

Decorosi F., *Studio di ceppi batterici per il biorisanamento di suoli contaminati da Cr(VI)*

Di Carlo P., *I Kalasha del Hindu Kush: ricerche linguistiche e antropologiche*

Di Patti F., *Finite-Size Effects in Stochastic Models of Population Dynamics: Applications to Biomedicine and Biology*

Inzitari M., *Determinants of Mobility Disability in Older Adults: Evidence from Population-Based Epidemiologic Studies*

Macri F., *Verso un nuovo diritto penale sessuale. Diritto vivente, diritto comparato e prospettive di riforma della disciplina dei reati sessuali in Italia*

Pace R., *Identità e diritti delle donne. Per una cittadinanza di genere nella formazione*

Vignolini S., *Sub-Wavelength Probing and Modification of Complex Photonic Structures*

ANNO 2010

Fedi M., *«Tuo lumine». L'accademia dei Risvegliati e lo spettacolo a Pistoia tra Sei e Settecento*

Fondi M., *Bioinformatics of genome evolution: from ancestral to modern metabolism. Phylogenomics and comparative genomics to understand microbial evolution*

Marino E., *An Integrated Nonlinear Wind-Waves Model for Offshore Wind Turbines*

Orsi V., *Crisi e Rigenerazione nella valle dell'Alto Khabur (Siria). La produzione ceramica nel passaggio dal Bronzo Antico al Bronzo Medio*

Polito C., *Molecular imaging in Parkinson's disease*

Romano R., *Smart Skin Envelope. Integrazione architettonica di tecnologie dinamiche e innovative per il risparmio energetico*

ANNO 2011

Acciaoli S., *Il trompe-l'œil letterario, ovvero il sorriso ironico nell'opera di Wilhelm Hauff*

Bernacchioni C., *Sfingolipidi bioattivi e loro ruolo nell'azione biologica di fattori di crescita e citochine*

Fabrizi N., *Bragg spectroscopy of quantum gases: Exploring physics in one dimension*

Gordillo Hervás R., *La construcción religiosa de la Hélade imperial: El Panhelenion*

Mugelli C., *Indipendenza e professionalità del giudice in Cina*  
Pollastri S., *Il ruolo di TAF12B e UVR3 nel ciclo circadiano dei vegetali*  
Salizzoni E., *Paesaggi Protetti. Laboratori di sperimentazione per il paesaggio costiero euro-mediterraneo*

ANNO 2012

Evangelisti E., *Structural and functional aspects of membranes: the involvement of lipid rafts in Alzheimer's disease pathogenesis. The interplay between protein oligomers and plasma membrane physicochemical features in determining cytotoxicity*  
Bondi D., *Filosofia e storiografia nel dibattito anglo-americano sulla svolta linguistica*  
Petrucci F., *Petri Candidi Decembrii Epistolarum iuveniliū libri octo. A cura di Federico Petrucci*  
Alberti M., *La 'scoperta' dei disoccupati. Alle origini dell'indagine statistica sulla disoccupazione nell'Italia liberale (1893-1915)*  
Galdani R., *Using the Patch-Clamp technique to shed light on ion channels structure, function and pharmacology*  
Adessi A., *Hydrogen production using Purple Non-Sulfur Bacteria (PNSB) cultivated under natural or artificial light conditions with synthetic or fermentation derived substrates*  
Ramalli A., *Development of novel ultrasound techniques for imaging and elastography. From simulation to real-time implementation*

ANNO 2013

Lunghi C., *Early cross-modal interactions and adult human visual cortical plasticity revealed by binocular rivalry*  
Brancaleoni I., *Architettura e illuminismo: filosofia e progetti di città nel tardo Settecento francese*  
Cucinotta E., *Produzione poetica e storia nella prassi e nella teoria greca di età classica*  
Pellegrini L., *Circostanze del reato: trasformazioni in atto e prospettive di riforma*  
Locatelli M., *Mid infrared digital holography and terahertz imaging*  
Muniz Miranda F., *Modelling of spectroscopic and structural properties using molecular dynamics*  
Bacci M., *Dinamica molecolare e modelli al continuo per il trasporto di molecole proteiche - Coarse-grained molecular dynamics and continuum models for the transport of protein molecules*  
Martelli R., *Characteristics of raw and cooked filets in species of actual and potential interest for italian aquaculture: rainbow trout (*oncorhynchus mykiss*) and meagre (*argyrosomus regius*)*

ANNO 2014

Lana D., *A study on cholinergic signal transduction pathways involved in short term and long term memory formation in the rat hippocampus. Molecular and cellular alterations underlying memory impairments in animal models of neurodegeneration*  
Lopez Garcia A., *Los Auditoria de Roma y el Athenaeum de Adriano*  
Pastorelli G., *L'immagine del cane in Franz Kafka*  
Bussoletti A., *L'età berlusconiana. Il centro-destra dai poli alla Casa della Libertà 1994-2001*  
Malavolti L., *Single molecule magnets sublimated on conducting and magnetic substrates*  
Belingardi C., *Comunanze urbane. Autogestione e cura dei luoghi*  
Guzzo E., *Il tempio nel tempio. Il tombeau di Rousseau al Panthéon di Parigi*

ANNO 2015

Lombardi N., *MEREA FaPS: uno Studio di Farmacovigilanza Attiva e Farmacoepidemiologia in Pronto Soccorso*  
Baratta L., *«A Marvellous and Strange Event». Racconti di nascite mostruose nell'Inghilterra della prima età moderna*



Richichi I.A., *La teocrazia: crisi e trasformazione di un modello politico nell'Europa del XVIII secolo*  
Palandri L., *I giudici e l'arte. Stati Uniti ed Europa a confronto*  
Caselli N., *Imaging and engineering optical localized modes at the nano scale*  
Calabrese G., *Study and design of topologies and components for high power density dc-dc converters*  
Porzilli S., *Rilevare l'architettura in legno. Protocolli metodologici per la documentazione delle architetture tradizionali lignee: i casi studio dei villaggi careliani in Russia*

ANNO 2016

Martinelli S., *Study of intracellular signaling pathways in Chronic Myeloproliferative Neoplasms*  
Abbado E., *"La celeste guida". L'oratorio musicale a Firenze: 1632-1799*  
Focarile P., *I Mannelli di Firenze. Storia mecenatismo e identità di una famiglia fra cultura mercantile e cultura cortigiana*  
Nucciotti A., *La dimensione normativa dell'imprenditorialità accademica. Tre casi di studio sugli investigatori principali, i loro gruppi di ricerca e i fattori di innesco dell'imprenditorialità accademica*  
Peruzzi P., *La inutilizzabilità della prestazione*  
Lottini E., *Magnetic Nanostructures: a promising approach towards RE-free permanent magnets*  
Uricchio T., *Image Understanding by Socializing the Semantic Gap*

ANNO 2017

Valenti R., *Cerebral Small Vessel Disease and Cerebral Amyloid Angiopathy: neuroimaging markers, cognitive features and rehabilitative issues*  
Starnini M., *L'uomo tutto intero. Biografia di Carlo Livi, psichiatra dell'Ottocento*  
Verardi D., *La scienza e i segreti della natura a Napoli nel Rinascimento: la magia naturale di Giovan Battista Della Porta*  
Minicucci G., *Il dolo nella bancarotta. Alla ricerca della tipicità soggettiva della fattispecie patrimoniale*  
Pattelli L., *Imaging light transport at the femtosecond scale: a walk on the wild side of diffusion*  
Egea Molines M.T., *Etnobotánica en el Alto Valle del Reno (Toscana y Emilia-Romaña, Italia). Etnobotanica nell'Alta Valle del Reno (Toscana ed Emilia-Romagna, Italia)*  
Romano I.M., *Pressione turistica sul Centro Storico di Firenze - sito UNESCO. Un modello per la valutazione dell'impatto percettivo*

ANNO 2018

Costa A., *Histaminergic neurotransmission as a gateway for the effects of the fat sensing molecule Oleoylethanolamide. Focus on cognition and stress-reactivity*  
Solera D., *«Sotto l'ombra della patente del Santo Ufficio». I familiares dell'Inquisizione romana tra XVI e XVII secolo*  
Landi G., *Secession and Referendum. A new Dimension of International Law on Territorial Changes?*  
Sacchetti A., *La costituente libertaria di Camillo Berneri. Un disegno politico tra federalismo e anarchismo*  
Livi L.F., *New quantum simulations with ultracold Ytterbium gases*  
Bellini E., *Ambienti sensoriali "terapeutici" che rendono Abili. Un progetto integrato di vita per persone con Disturbi dello Spettro Autistico*  
Piscitelli L.R., *Serviceability and post-failure behaviour of laminated glass structural elements*

ANNO 2019

Molinaro A., *New insights into creatine transporter deficiency. Identification of neuropathological and metabolic targets for treatment*

- Romano M., *Soldati e neuropsichiatria nell'Italia della Grande Guerra. Controllo militare e pratiche assistenziali a confronto (1915-1918)*
- Venturi M.T., «Io vivo fra le cose e invento, come posso, il modo di nominarle». Pier Paolo Pasolini e la lingua della modernità
- Rossi F., *Apparenza del diritto e rapporti di fatto nell'esperienza giuridica di Roma antica*
- Turrini L., *Development of optical methods for real-time whole-brain functional imaging of zebrafish neuronal activity*
- Moschetti V., *Camere Azzurre. Costruzione di un'antologia mediterranea. Da Palladio a Peter Märkli*
- Talluri L., *Micro turbo expander design for small scale ORC. Tesla turbine*

ANNO 2020

- De Vita D., *Functional validation of genetic variants identified by next generation sequencing in malformations of cortical development*
- Al Owaidi R., *La letteratura cavalleresca e il mondo arabo: il caso di Andrea da Barberino. Regesto e studio critico*
- Galante A., *Legalità e mutamenti giurisprudenziali nel diritto penale. Fondamento e limiti del divieto di retroattività dei mutamenti giurisprudenziali sfavorevoli*
- Colzi L., *Isotopic fractionation study towards massive star-forming regions across the Galaxy*
- Di Rosa M., *Tectono-metamorphic evolution of the continental units along the edge between Alpine and Hercynian Corsica. Constraints for the exhumation models in the continental collision setting*
- Miccinesi L., *Advanced Ground-Based Real and Synthetic Aperture Radar*
- Ricci C., *Santa Maria degli Angeli: un monastero camaldolese "dimenticato" nel centro di Firenze. Analisi del percorso storico-architettonico in età moderna e contemporanea*

*Premio Tesi Dottorato*

Firenze University Press - Università degli Studi di Firenze

2020

## Advanced Ground-Based Real and Synthetic Aperture Radar

Ground-based/terrestrial radar interferometry (GBRI) is a scientific topic of increasing interest in recent years. The GBRI is used in several fields as a remote sensing technique for monitoring the natural environment (landslides, glaciers, and mines) or infrastructures (bridges, towers). These sensors provide the displacement of targets by measuring the phase difference between the sending and receiving radar signals. If the acquisition rate is high enough, the GBRI can provide the natural frequency, e.g. by calculating the Fourier transform of displacement. The research activity, presented in this work, concerns the design and development of some advanced GBRI systems. These systems are related to the following issues: detection of displacement vectors, Multiple Input Multiple Output (MIMO) and radars with 3D capability.

LAPO MICCINESI received the M.S. degree in physics of particles in 2016 and the Ph.D. degree in information engineering from the University of Florence, Florence, Italy, in 2020. He is with the Department of Information Engineering, University of Florence, as a Post-Degree Grant Recipient.

ISSN 2612-8039 (print)  
ISSN 2612-8020 (online)  
ISBN 978-88-5518-376-5 (Print)  
ISBN 978-88-5518-377-2 (PDF)  
ISBN 978-88-5518-378-9 (XML)  
DOI 10.36253/978-88-5518-377-2

[www.fupress.com](http://www.fupress.com)